

1 A search for sparticles in zero lepton final states

2 Russell W. Smith

3 Submitted in partial fulfillment of the

4 requirements for the degree of

5 Doctor of Philosophy

6 in the Graduate School of Arts and Sciences

7 COLUMBIA UNIVERSITY

8 2016

9

© 2016

10

Russell W. Smith

11

All rights reserved

12

## ABSTRACT

13

A search for sparticles in zero lepton final states

14

Russell W. Smith

15 TODO : Here's where your abstract will eventually go. The above text is all in the  
16 center, but the abstract itself should be written as a regular paragraph on the page,  
17 and it should not have indentation. Just replace this text.



---

*Contents*

19	<b>Contents</b>	i
20	<b>1 Introduction</b>	1
21	<b>2 The Standard Model</b>	5
22	2.1 Overview	5
23	2.2 Field Content	5
24	2.3 Deficiencies of the Standard Model	15
25	<b>3 Supersymmetry</b>	21
26	3.1 Supersymmetric theories : from space to superspace	21
27	3.2 Minimally Supersymmetric Standard Model	24
28	3.3 Phenomenology	30
29	3.4 How SUSY solves the problems with the SM	33
30	3.5 Conclusions	35
31	<b>4 The Large Hadron Collider</b>	37
32	4.1 Basics of Accelerator Physics	37
33	4.2 Accelerator Complex	39
34	4.3 Large Hadron Collider	41
35	4.4 Dataset Delivered by the LHC	43
36	<b>5 The ATLAS detector</b>	49

37	5.1	Magnets	50
38	5.2	Inner Detector	52
39	5.3	Calorimetry	56
40	5.4	Muon Spectrometer	61
41	5.5	Trigger System	66
42	<b>6</b>	<b>Object Reconstruction</b>	<b>73</b>
43	6.1	Primitive Object Reconstruction	73
44	6.2	Physics Object Reconstruction and Quality Identification	79
45	<b>7</b>	<b>Recursive Jigsaw Reconstruction</b>	<b>105</b>
46	7.1	Razor variables	105
47	7.2	Recursive Jigsaw Reconstruction	110
48	7.3	Variables used in the search for zero lepton SUSY	116
49	<b>8</b>	<b>A search for supersymmetric particles in zero lepton final states with the Recursive Jigsaw Technique</b>	<b>123</b>
50	8.1	Collision data and simulation samples	123
51	8.2	Event selection	127
52	8.3	Background estimation	134
54	<b>9</b>	<b>Results</b>	<b>139</b>
55	9.1	Statistical Analysis	139
56	9.2	Signal Region distributions	139
57	9.3	Pull Plots	139
58	9.4	Exclusion plots	139
59	<b>Conclusion</b>		<b>141</b>
60	9.5	New Section	141

61	<b>Bibliography</b>	<b>143</b>
62	<b>Quantum Field Theory and Symmetries</b>	<b>155</b>
63	Quantum Field Theory	155
64	Symmetries	156
65	Local symmetries	158
66	<b>Additional N-1 plots</b>	<b>163</b>
67	Compressed region N-1 plots	163



---

*Acknowledgements*



---

*Dedication*



*Introduction*

72 Particle physics is a remarkably successful field of scientific inquiry. The ability to  
 73 precisely predict the properties of a exceedingly wide range of physical phenomena,  
 74 such as the description of the cosmic microwave background [1, 2], the understanding  
 75 of the anomalous magnetic dipole moment of the electron [3, 4], and the measurement  
 76 of the number of weakly-interacting neutrino flavors [5] is truly amazing.

77 The theory that has allowed this range of predictions is the *Standard Model*  
 78 of particle physics (SM). The Standard Model combines the electroweak theory of  
 79 Glashow, Weinberg, and Salam [6–8] with the theory of the strong interactions, as  
 80 first envisioned by Gell-Mann and Zweig [9, 10]. This quantum field theory (QFT)  
 81 contains a tiny number of particles, whose interactions describe phenomena up to at  
 82 least the TeV scale. These particles are manifestations of the fields of the Standard  
 83 Model, after application of the Higgs Mechanism. The particle content of the SM  
 84 consists only of the six quarks, the six leptons, the four gauge bosons, and the scalar  
 85 Higgs boson.

86 Despite its impressive range of described phenomena, the Standard Model has  
 87 some theoretical and experimental deficiencies. The SM contains 26 free parameters  
 88 <sup>1</sup>. It would be more theoretically pleasing to understand these free parameters in  
 89 terms of a more fundamental theory. The major theoretical concern of the Standard  
 90 Model, as it pertains to this thesis, is the *hierarchy problem*[11–15]. The light mass

---

<sup>1</sup>This is the Standard Model corrected to include neutrino masses. These parameters are the fermion masses (6 leptons, 6 quarks), CKM and PMNS mixing angles (8 angles, 2 CP-violating phases), W/Z/Higgs masses (3), the Higgs field expectation value, and the couplings of the strong, weak, and electromagnetic forces (3  $\alpha_{force}$  ).

of the Higgs boson (125 GeV) should be quadratically dependent on the scale of UV physics, due to the quantum corrections from high-energy physics processes. The most perplexing experimental issue is the existence of *dark matter*, as demonstrated by galactic rotation curves [16–22]. This data has shown that there exists additional matter which has not yet been seen interacting with the particles of the Standard Model. There is no particle in the SM which can act as a candidate for dark matter.

Both of these major issues, as well as numerous others, can be solved by the introduction of *supersymmetry* (SUSY) [15, 23–35]. In supersymmetric theories, each SM particles has a so-called *superpartner*, or sparticle partner, differing from given SM particle by 1/2 in spin. These theories solve the hierarchy problem, since the quantum corrections induced from the superpartners exactly cancel those induced by the SM particles. In addition, these theories are usually constructed assuming *R*–parity, which can be thought of as the “charge” of supersymmetry, with SM particles having  $R = 1$  and sparticles having  $R = -1$ . In collider experiments, since the incoming SM particles have total  $R = 1$ , the resulting sparticles are produced in pairs. This produces a rich phenomenology, which is characterized by significant hadronic activity and large missing transverse energy ( $E_T^{\text{miss}}$ ), which provide significant discrimination against SM backgrounds [36].

Despite the power of searches for supersymmetry where  $E_T^{\text{miss}}$  is a primary discriminating variable, there has been significant interest in the use of other variables to discriminate against SM backgrounds. These include searches employing variables such as  $\alpha T$ ,  $M_{T,2}$ , and the razor variables ( $M_R, R^2$ ) [37–47]. In this thesis, we will present the first search for supersymmetry using the novel Recursive Jigsaw Reconstruction (RJR) technique. RJR can be considered the conceptual successor of the razor variables. We impose a particular final state “decay tree” on an events, which roughly corresponds to a simplified Feynmann diagram in decays containing weakly-interacting particles. We account for the missing degrees of freedom associated

118 to the weakly-interacting particles by a series of simplifying assumptions, which allow  
119 us to calculate our variables of interest at each step in the decay tree. This allows an  
120 unprecedented understanding of the internal structure of the decay and the ability to  
121 construct additional variables to reject Standard Model backgrounds.

122 This thesis details a search for the superpartners of the gluon and quarks, the  
123 gluino and squarks, in final states with zero leptons, with  $13.3 \text{ fb}^{-1}$  of data using the  
124 ATLAS detector. We organize the thesis as follows. The theoretical foundations of  
125 the Standard Model and supersymmetry are described in Chapters 2 and 3. The  
126 Large Hadron Collider and the ATLAS detector are presented in Chapters 4 and 5.  
127 Chapter 5 provides a detailed description of Recursive Jigsaw Reconstruction and a  
128 description of the variables used for the particular search presented in this thesis.  
129 Chapter 6 presents the details of the analysis, including details of the dataset, object  
130 reconstruction, and selections used. In Chapter 7, the final results are presented;  
131 since there is no evidence of a supersymmetric signal in the analysis, we present the  
132 final exclusion curves in simplified supersymmetric models.



---

**135 2.1 Overview**

136 A Standard Model is another name for a theory of the internal symmetry group  
 137  $SU(3)_C \otimes SU(2)_L \otimes U(1)_Y$ , with its associated set of parameters. *The Standard*  
 138 Model refers specifically to a Standard Model with the proper parameters to describe  
 139 the universe. The SM is the culmination of years of work in both theoretical  
 140 and experimental particle physics. In this thesis, we take the view that theorists cite

141 construct a model with the field content and symmetries as inputs, and write down the  
 142 most general Lagrangian consistent with those symmetries. Assuming this model is  
 143 compatible with nature (in particular, the predictions of the model are consistent with  
 144 previous experiments), experimentalists are responsible measuring the parameters of  
 145 this model. This will be applicable for this chapter and the following one.

146 Additional theoretical background is in 9.5. The philosophy and notations are  
 147 inspired by [48, 49].

---

**148 2.2 Field Content**

The Standard Model field content is

$$\begin{aligned} \text{Fermions} &: Q_L(3, 2)_{+1/3}, U_R(3, 1)_{+4/3}, D_R(3, 1)_{-2/3}, L_L(1, 2)_{-1}, E_R(1, 1)_{-2} \\ \text{Scalar (Higgs)} &: \phi(1, 2)_{+1} \\ \text{Vector Fields} &: G^\mu(8, 1)_0, W^\mu(1, 3)_0, B^\mu(1, 1)_0 \end{aligned} \tag{2.1}$$

149 where the  $(A, B)_Y$  notation represents the irreducible representation under  $SU(3)$   
150 and  $SU(2)$ , with  $Y$  being the electroweak hypercharge. Each of these fermion fields  
151 has an additional index, representing the three generation of fermions.

152 We observed that  $Q_L, U_R$ , and  $D_R$  are triplets under  $SU(3)_C$ ; these are the *quark*  
153 fields. The *color* group,  $SU(3)_C$  is mediated by the *gluon* field  $G^\mu(8, 1)_0$ , which has  
154 8 degrees of freedom. The fermion fields  $L_L(1, 2)_{-1}$  and  $E_R(1, 1)_{-2}$  are singlets under  
155  $SU(3)_C$ ; we call them the *lepton* fields.

156 Next, we note the “left-handed” (“right-handed”) fermion fields, denoted by  $L$  ( $R$ )  
157 subscript, The left-handed fields form doublets under  $SU(2)_L$ . These are mediated  
158 by the three degrees of freedom of the “W” fields  $W^\mu(1, 3)_0$ . These fields only act  
159 on the left-handed particles of the Standard Model. This is the reflection of the  
160 “chirality” of the Standard Model; the left-handed and right-handed particles are  
161 treated differently by the electroweak forces. The right-handed fields,  $U_R, D_R$ , and  
162  $E_R$ , are singlets under  $SU(2)_L$ .

163 The  $U(1)_Y$  symmetry is associated to the  $B^\mu(1, 1)_0$  boson with one degree of  
164 freedom. The charge  $Y$  is known as the electroweak hypercharge.

165 To better understand the phenomenology of the Standard Model, let us investigate  
166 each of the *sectors* of the Standard Model separately.

## 167 Electroweak sector

The electroweak sector refers to the  $SU(2)_L \otimes U(1)_Y$  portion of the Standard  
Model gauge group. Following our philosophy of writing all gauge-invariant and  
renormalizable terms, the electroweak Lagrangian can be written as

$$\mathcal{L} = W_a^{\mu\nu} W_{\mu\nu}^a + B^{\mu\nu} B_{\mu\nu} + (D^\mu \phi)^\dagger D_\mu \phi - \mu^2 \phi^\dagger \phi - \lambda (\phi^\dagger \phi)^2. \quad (2.2)$$

where  $W_a^{\mu\nu}$  are the three ( $a = 1, 2, 3$ ) gauge bosons associated to the  $SU(2)_L$  gauge  
group,  $B^{\mu\nu}$  is the one gauge boson of the  $U(1)_Y$  gauge group, and  $\phi$  is the complex

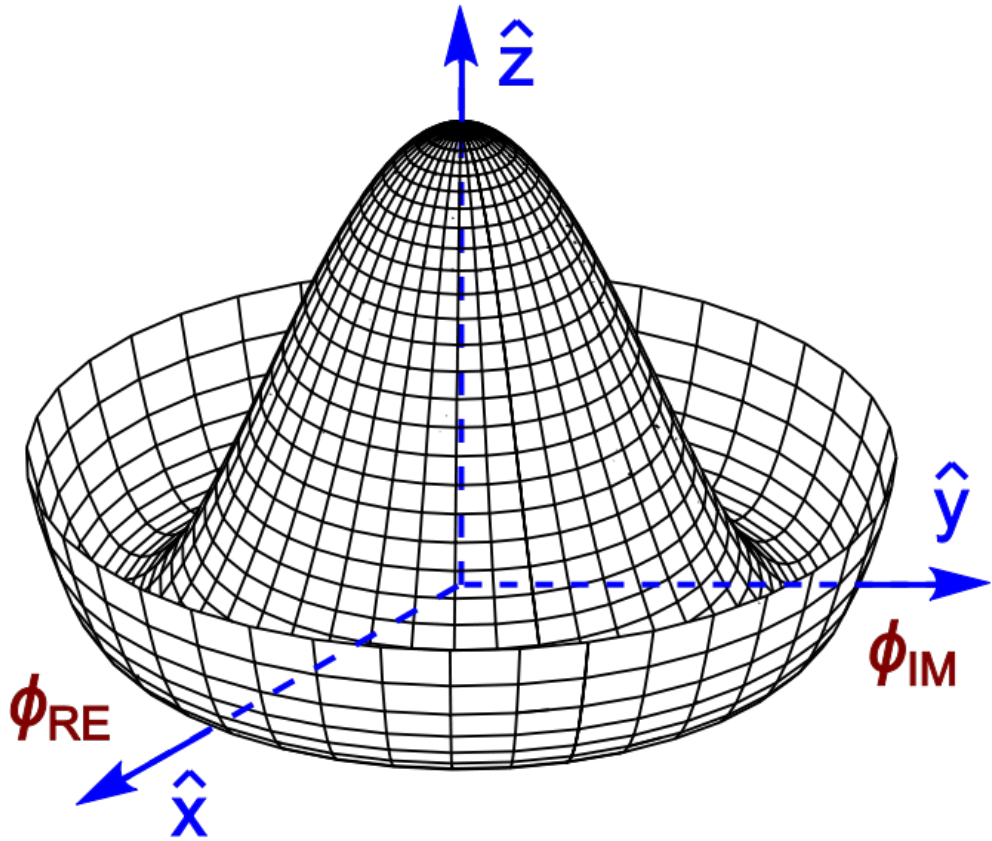


Figure 2.1: Sombrero potential

Higgs multiplet. The covariant derivative  $D^\mu$  is given by

$$D^\mu = \partial^\mu + \frac{ig}{2}W_a^\mu\sigma_a + \frac{ig'}{2}B^\mu \quad (2.3)$$

where  $i\sigma_a$  are the Pauli matrices times the imaginary constant, which are the generators for  $SU(2)_L$ , and  $g$  and  $g'$  are the  $SU(2)_L$  and  $U(1)_Y$  coupling constants, respectively. The field strength tensors  $W_a^{\mu\nu}$  and  $B^{\mu\nu}$  are given by the commutator of the covariant derivative associated to each field

$$B^{\mu\nu} = \partial^\mu B^\nu - \partial^\nu B^\mu \quad (2.4)$$

$$W_a^{\mu\nu} = \partial^\mu W_a^\nu - \partial^\nu W_a^\mu - g\epsilon_{abc}W_a^\mu W_b^\nu, \quad i = 1, 2, 3$$

169      The terms in the Lagrangian 2.2 proportional to  $\mu^2$  and  $\lambda$  make up the “Higgs  
 170 potential” [50]. As normal (see Appendix 9.5), we restrict  $\lambda > 0$  to guarantee our  
 171 potential is bounded from below, and we also require  $\mu^2 < 0$ , which gives us the  
 172 standard “sombrero” potential shown in 2.1.

This potential has infinitely many minima at  $\langle \phi \rangle = \sqrt{2m/\lambda}$ ; the ground state is *spontaneously* broken by the choice of ground state, which induces a vacuum expectation value (VEV). Without loss of generality, we can choose the Higgs field  $\phi$  to point in the real direction, and write the Higgs field  $\phi$  in the following form :

$$\phi = \frac{1}{\sqrt{2}} \exp\left(\frac{i}{v} \sigma_a \theta_a\right) \begin{pmatrix} 0 \\ v + h(x) \end{pmatrix}. \quad (2.5)$$

We choose a gauge to rotate away the dependence on  $\theta_a$ , such that we can write simply

$$\phi = \frac{1}{\sqrt{2}} \begin{pmatrix} 0 \\ v + h(x) \end{pmatrix}. \quad (2.6)$$

Now, we can see how the masses of the vector bosons are generated from the application of the Higgs mechanism. We plug Eq.2.6 back into the electroweak Lagrangian, and only showing the relevant mass terms in the vacuum state where  $h(x) = 0$  see that (dropping the Lorentz indices) :

$$\begin{aligned} \mathcal{L}_M &= \frac{1}{8} \left| \begin{pmatrix} gW_3 + g'B & g(W_1 - iW_2) \\ g(W_1 + iW_2) & -gW_3 + g'B \end{pmatrix} \begin{pmatrix} 0 \\ v \end{pmatrix} \right|^2 \\ &= \frac{g^2 v^2}{8} \left[ W_1^2 + W_2^2 + \left( \frac{g'}{g} B - W_3 \right)^2 \right] \end{aligned} \quad (2.7)$$

Defining the Weinberg angle  $\tan(\theta_W) = g'/g$  and the following *physical* fields :

$$W^\pm = \frac{1}{\sqrt{2}} (W_1 \mp iW_2) \quad (2.8)$$

$$Z^0 = \cos \theta_W W_3 - \sin \theta_W B$$

$$A^0 = \sin \theta_W W_3 + \cos \theta_W B$$

we can write the piece of the Lagrangian associated to the vector boson masses as

$$\mathcal{L}_{MV} = \frac{1}{4}g^2 v^2 W^+ W^- + \frac{1}{8}(g^2 + g'^2) v^2 Z^0 Z^0. \quad (2.9)$$

and we have the following values of the masses for the vector bosons :

$$\begin{aligned} m_W^2 &= \frac{1}{4}v^2 g^2 \\ m_Z^2 &= \frac{1}{4}v^2(g^2 + g'^2) \\ m_A^2 &= 0 \end{aligned} \quad (2.10)$$

We thus see how the Higgs mechanism gives rise to the masses of the  $W^\pm$  and  $Z$  boson in the Standard Model; the mass of the photon is zero, as expected. The  $SU(2)_L \otimes U(1)_Y$  symmetry of the initially massless  $W_{1,2,3}$  and  $B$  fields is broken to the  $U(1)_{EM}$ . Of the four degrees of freedom in the complex Higgs doublet, three are “eaten” when we give mass to the  $W^\pm$  and  $Z_0$ , while the other degree of freedom is the Higgs particle, as found in 2012 by the ATLAS and CMS collaborations [51, 52].

## 179 Quantum Chromodynamics

Quantum chromodynamics (or the theory of the *strong* force) characterizes the behavior of *colored* particles, collectively known as *partons*. The partons of the Standard Model are the (fermionic) quarks, and the (bosonic) gluons. The strong force is governed by  $SU(3)_C$ , an unbroken symmetry in the Standard Model, which implies the gluon remains massless. Defining the covariant derivative for QCD as

$$D^\mu = \partial^\mu + ig_s G_a^\mu L_a, a = 1, \dots, 8 \quad (2.11)$$

where  $L_a$  are the generators of  $SU(3)_C$ , and  $g_s$  is the coupling constant of the strong force. The QCD Lagrangian then is given by

$$\mathcal{L}_{QCD} = i\bar{\psi}_f D_\mu \gamma^\mu \psi_f - \frac{1}{4}G_{a,\mu\nu} G_a^{\mu\nu} \quad (2.12)$$

where the summation over  $f$  is for quarks *families*, and  $G_a^{\mu\nu}$  is the gluon field strength tensor, given by

$$G_a^{\mu\nu} = \partial^\mu G_a^\nu - \partial^\nu G_a^\mu - g_s f^{abc} G_b^\mu G_c^\nu, a, b, c = 1, \dots, 8 \quad (2.13)$$

180 where  $f^{abc}$  are the structure constants of  $SU(3)_C$ , which are analogous to  $\epsilon_{abc}$  for  
 181  $SU(2)_L$ . The kinetic term for the quarks is contained in the standard  $\partial_\mu$  term, while  
 182 the field strength term contains the interactions between the quarks and gluons, as  
 183 well as the gluon self-interactions.

184 Written down in this simple form, the QCD Lagrangian does not seem much  
 185 different from the QED Lagrangian, with the proper adjustments for the different  
 186 group structures. The gluon is massless, like the photon, so one could naïvely expect  
 187 an infinite range force, and it pays to understand why this is not the case. The  
 188 reason for this fundamental difference is the gluon self-interactions arising in the  
 189 field strength tensor term of the Lagrangian. This leads to the phenomena of *color*  
 190 *confinement*, which describes how one only observes color-neutral particles alone in  
 191 nature. In contrast to the electromagnetic force, particles which interact via the  
 192 strong force experience a *greater* force as the distance between the particles increases.  
 193 At long distances, the potential is given by  $V(r) = -kr$ . At some point, it is more  
 194 energetically favorable to create additional partons out of the vacuum than continue  
 195 pulling apart the existing partons, and the colored particles undergo *fragmentation*.  
 196 This leads to *hadronization*. Bare quarks and gluons are actually observed as sprays  
 197 of hadrons (primarily kaons and pions); these sprays are known as *jets*, which are  
 198 what are observed by experiments.

199 It is important to recognize the importance of understanding these QCD inter-  
 200 actions in high-energy hadron colliders such as the LHC. Since protons are hadrons,  
 201 proton-proton collisions such as those produced by the LHC are primarily governed by  
 202 the processes of QCD. In particular, by far the most frequent process observed in LHC  
 203 experiments is dijet production from gluon-gluon interactions (see Fig.2.2). These

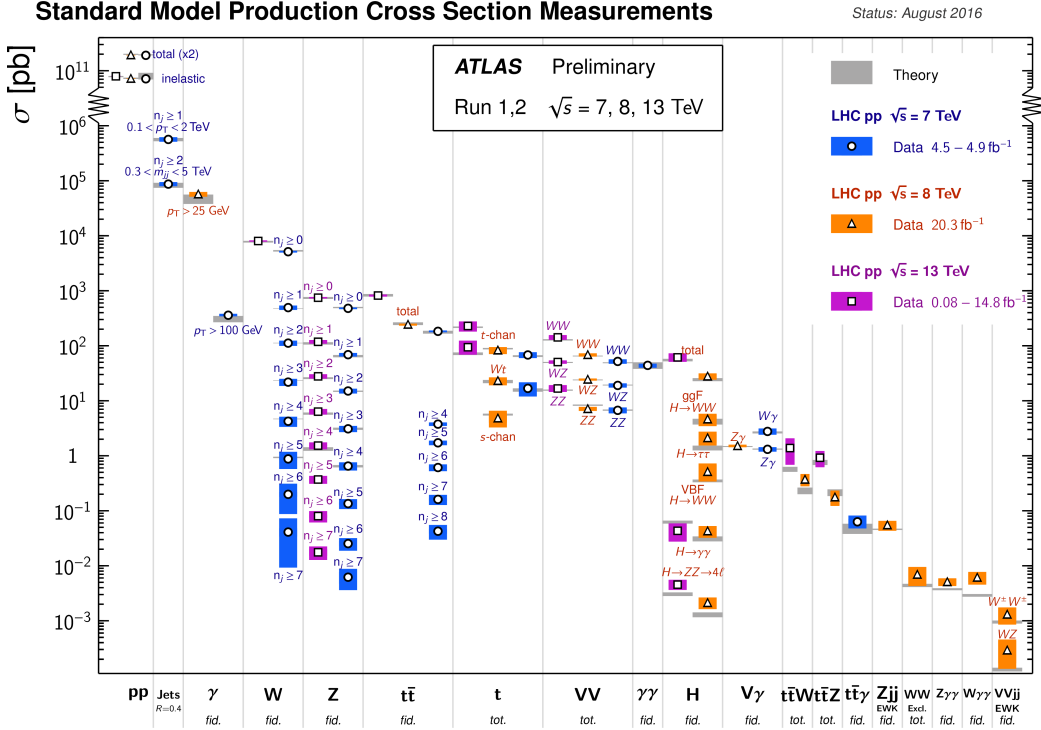


Figure 2.2: Cross-sections of various Standard Model processes

204 gluons that interact are part of the *sea* particles inside the proton; the simple  $p = uud$   
 205 model does not apply. The main *valence*  $uud$  quarks are constantly interacting via  
 206 gluons, which can themselves radiate gluons or split into quarks, and so on. A more  
 207 useful understanding is given by the colloquially-known *bag* model [53, 54], where the  
 208 proton is seen as a “bag” of (in principle) infinitely many partons, each with energy  
 209  $E < \sqrt{s} = 6.5$  TeV. One then collides this (proton) bag with another, and views the  
 210 products of this very complicated collision, where calculations include many loops in  
 211 nonperturbative QCD calculations.

212 Fortunately, we are generally saved by the QCD factorization theorems [55]. This  
 213 allows one to understand the hard (i.e. short distance or high energy)  $2 \rightarrow 2$  parton  
 214 process using the tools of perturbative QCD, while making series of approximations  
 215 known as a *parton shower* model to understand the additional corrections from  
 216 nonperturbative QCD. We will discuss the reconstruction of jets by experiments in  
 217 Ch.5.

218 **Fermions**

219 We will now look more closely at the fermions in the Standard Model [56].

220 As noted earlier in Sec.2.2, the fermions of the Standard Model can be first  
 221 distinguished between those that interact via the strong force (quarks) and those  
 222 which do not (leptons).

There are six leptons in the Standard Model, which can be placed into three  
*generations*.

$$\begin{pmatrix} e \\ \nu_e \end{pmatrix}, \begin{pmatrix} \mu \\ \nu_\mu \end{pmatrix}, \begin{pmatrix} \tau \\ \nu_\tau \end{pmatrix} \quad (2.14)$$

223 There is the electron ( $e$ ), muon ( $\mu$ ), and tau ( $\tau$ ), each of which has an associated  
 224 neutrino ( $\nu_e, \nu_\mu, \nu_\tau$ ). Each of the so-called charged (“electron-like”) leptons has  
 225 electromagnetic charge  $-1$ , while the neutrinos all have  $q_{EM} = 0$ .

226 Often in an experimental context, lepton is used to denote the stable electron  
 227 and metastable muon, due to their striking experimental signatures. Taus are often  
 228 treated separately, due to their much shorter lifetime of  $\tau_\tau \sim 10^{-13}s$ ; these decay  
 229 through hadrons or the other leptons, so often physics analyses at the LHC treat  
 230 them as jets or leptons, as will be done in this thesis.

231 As the neutrinos are electrically neutral, nearly massless, and only interact via the  
 232 weak force, it is quite difficult to observe them directly. Since LHC experiments rely  
 233 overwhelmingly on electromagnetic interactions to observe particles, the presence of  
 234 neutrinos is not observed directly. Neutrinos are instead observed by the conservation  
 235 of four-momentum in the plane transverse to the proton-proton collisions, known as  
 236 *missing transverse energy*.

There are six quarks in the Standard Model : up, down, charm, strange, top, and  
 bottom. Quarks are similar organized into three generations :

$$\begin{pmatrix} u \\ d \end{pmatrix}, \begin{pmatrix} c \\ s \end{pmatrix}, \begin{pmatrix} t \\ b \end{pmatrix} \quad (2.15)$$

237 where we speak of “up-like” quarks and “down-like” quarks.

238 Each up-like quark has charge  $q_{up} = 2/3$ , while the down-like quarks have  $q_{down} =$   
239  $-1/3$ . At the high energies of the LHC, one often makes the distinction between  
240 the light quarks ( $u, d, c, s$ ), the bottom quark, and top quark. In general, due to  
241 the hadronization process described above, the light quarks, with masses  $m_q < \sim$   
242  $1.5\text{GeV}$  are indistinguishable by LHC experiments. Their hadronic decay products  
243 generally have long lifetimes and they are reconstructed as jets.<sup>1</sup>. The bottom quark  
244 hadronizes primarily through the  $B$ -mesons, which generally travels a short distance  
245 before decaying to other hadrons. This allows one to distinguish decays via  $b$ -quarks  
246 from other jets; this procedure is known as *b-tagging* and will be discussed more in  
247 Ch.5. Due to its large mass, the top quark decays before it can hadronize; there  
248 are no bound states associated to the top quark. The top is of particular interest at  
249 the LHC; it has a striking signature through its most common decay mode  $t \rightarrow Wb$ .  
250 Decays via tops, especially  $t\bar{t}$  are frequently an important signal decay mode, or an  
251 important background process.

## 252 **Interactions in the Standard Model**

253 We briefly overview the entirety of the fundamental interactions of the Standard  
254 Model; these can also be found in 2.3.

255 The electromagnetic force, mediated by the photon, interacts with via a three-  
256 point coupling all charged particles in the Standard Model. The photon thus interacts  
257 with all the quarks, the charged leptons, and the charged  $W^\pm$  bosons.

258 The weak force is mediated by three particles : the  $W^\pm$  and the  $Z^0$ . The  $Z^0$  can  
259 interacts with all fermions via a three-point coupling. A real  $Z_0$  can thus decay to  
260 a fermion-antifermion pair of all SM fermions except the top quark, due to its large

---

<sup>1</sup>In some contexts, charm quarks are also treated as a separate category, although it is quite difficult to distinguish charm quarks from the other light quarks.

## Standard Model Interactions (Forces Mediated by Gauge Bosons)



Figure 2.3: The interactions of the Standard Model

mass. The  $W^\pm$  has two important three-point interactions with fermions. First, the  $W^\pm$  can interact with an up-like quark and a down-like quark; an important example in LHC experiments is  $t \rightarrow Wb$ . The coupling constants for these interactions are encoded in the unitary matrix known as the Cabibbo–Kobayashi–Maskawa (CKM) matrix [57, 58], and are generally known as flavor-changing interactions. Secondly, the  $W^\pm$  interacts with a charged lepton and its corresponding neutrino. In this case, the unitary matrix that corresponds to CKM matrix for quarks is the identity matrix, which forbids (fundamental) vertices such as  $\mu \rightarrow We$ . For leptons, instead this is a two-step process :  $\mu \rightarrow \nu_m u W \rightarrow \nu_m u \bar{\nu}_e e$ . Finally, there are the self-interactions

270 of the weak gauge bosons. There is a three-point and four-point interaction; all  
271 combinations are allowed which conserve electric charge.

272 The strong force is mediated by the gluon, which as discussed above also carries  
273 the strong color charge. There is the fundamental three-point interaction, where a  
274 quark radiates a gluon. Additionally, there are the three-point and four-point gluon-  
275 only interactions.

## 276 2.3 Deficiencies of the Standard Model

277 At this point, it is quite easy to simply rest on our laurels. This relatively simple  
278 theory is capable of explaining a very wide range of phenomena, which ultimately  
279 break down only to combinations of nine diagrams shown in Fig.2.3. Unfortunately,  
280 there are some unexplained problems with the Standard Model. We cannot go  
281 through all of the potential issues in this thesis, but we will motivate the primary  
282 issues which naturally lead one to *supersymmetry*, as we will see in Ch.3.

The Standard Model has many free parameters; see Table 2.1 In general, we prefer models with less free parameters. A great example of this fact, and the primary experimental evidence for EWSB, is the relationship between the couplings of the weak force and the masses of the gauge bosons of the weak force :

$$\rho \equiv \frac{m_W^2}{m_Z^2 \cos^2 \theta_W} \stackrel{?}{=} 1 \quad (2.16)$$

283 where ? indicates that this is a testable prediction of the Standard Model (in  
284 particular, that the gauge bosons gain mass through EWSB). This relationship has  
285 been measured within experimental and theoretical predictions. We would like to  
286 produce additional such relationships, which would exist if the Standard Model is a  
287 low-energy approximation of some other theory.

288 An additional issue is the lack of *gauge coupling unification*. The couplings of  
289 any quantum field theory “run” as a function of the distance scales (or inversely,

$m_e$	Electron mass	511 keV
$m_\mu$	Muon mass	105.7 MeV
$m_\tau$	Tau mass	1.78 GeV
$m_u$	Up quark mass	1.9 MeV ( $m_{\bar{MS}} = 2\text{GeV}$ )
$m_d$	Down quark mass	4.4 MeV ( $m_{\bar{MS}} = 2\text{GeV}$ )
$m_s$	Strange quark mass	87 MeV ( $m_{\bar{MS}} = 2\text{GeV}$ )
$m_c$	Charm quark mass	1.32 GeV ( $m_{\bar{MS}} = m_c$ )
$m_b$	Bottom quark mass	4.24 GeV ( $m_{\bar{MS}} = m_b$ )
$m_t$	Top quark mass	172.7 GeV (on-shell renormalization)
$\theta_{12}$ CKM	12-mixing angle	13.1°
$\theta_{23}$ CKM	23-mixing angle	2.4°
$\theta_{13}$ CKM	13-mixing angle	0.2°
$\delta$ CKM	CP-violating Phase	0.995
$g'$	U(1) gauge coupling	0.357 ( $m_{\bar{MS}} = m_Z$ )
$g$	SU(2) gauge coupling	0.652 ( $m_{\bar{MS}} = m_Z$ )
$g_s$	SU(3) gauge coupling	1.221 ( $m_{\bar{MS}} = m_Z$ )
$\theta_{QCD}$	QCD vacuum angle	~0
VEV	Higgs vacuum expectation value	246 GeV
$m_H$	Higgs mass	125 GeV

Table 2.1: Parameters of the Standard Model. For values dependent on the renormalization scheme, we use a combination of the on-shell normalization scheme [59–62] and modified minimal subtraction scheme with  $m_{\bar{MS}}$  as indicated in the table[63]

290 energy scales) of the theory. The idea is closely related to the unification of the  
 291 electromagnetic and weak forces at the so-called *electroweak scale* of  $O(100 \text{ GeV})$ .  
 292 One would hope this behavior was repeated between the electroweak forces and the  
 293 strong force at some suitable energy scale. The Standard Model does automatically  
 294 not exhibit this behavior, as we can see in Fig.2.4.

The most significant problem with the Standard Model is the *hierarchy problem*. In its most straightforward incarnation, the Higgs scalar field is subject to quantum corrections through loop diagrams, as shown in Fig.2.5. For demonstration, we use the contributions from the top quark, since the top quark has the largest Higgs Yukawa coupling due to its large mass. In general, we should expect these corrections to quadratically depend on the scale of the ultraviolet physics,  $\Lambda$ . Briefly assume there is no new physics before the Planck scale of gravity,  $\Lambda_{\text{Planck}} = 10^{19} \text{ GeV}$ . In this

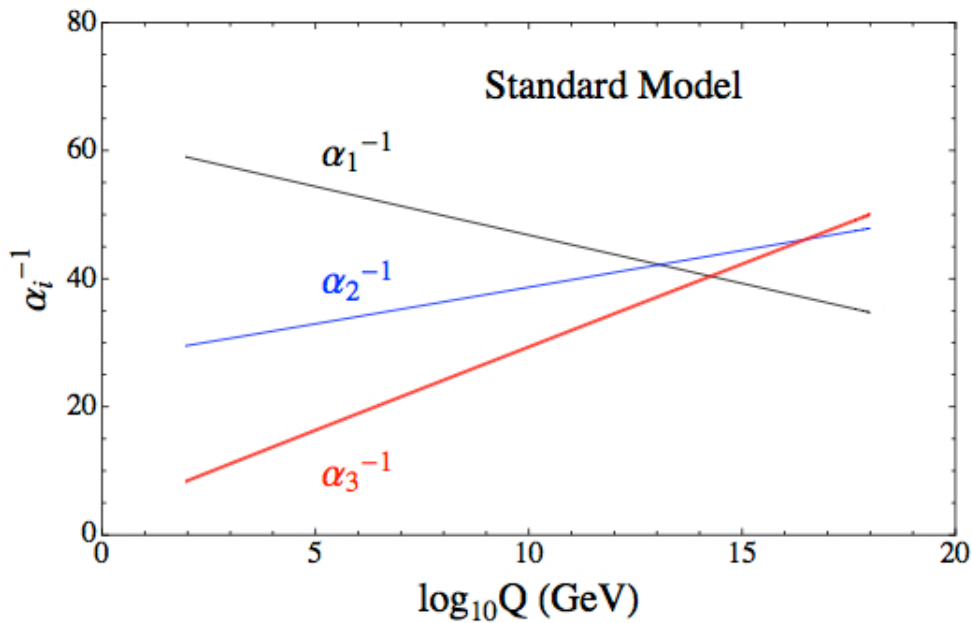


Figure 2.4: The running of Standard Model gauge couplings. The Standard Model couplings do not unify at high energies, which indicates it cannot completely describe nature through the Planck scale.

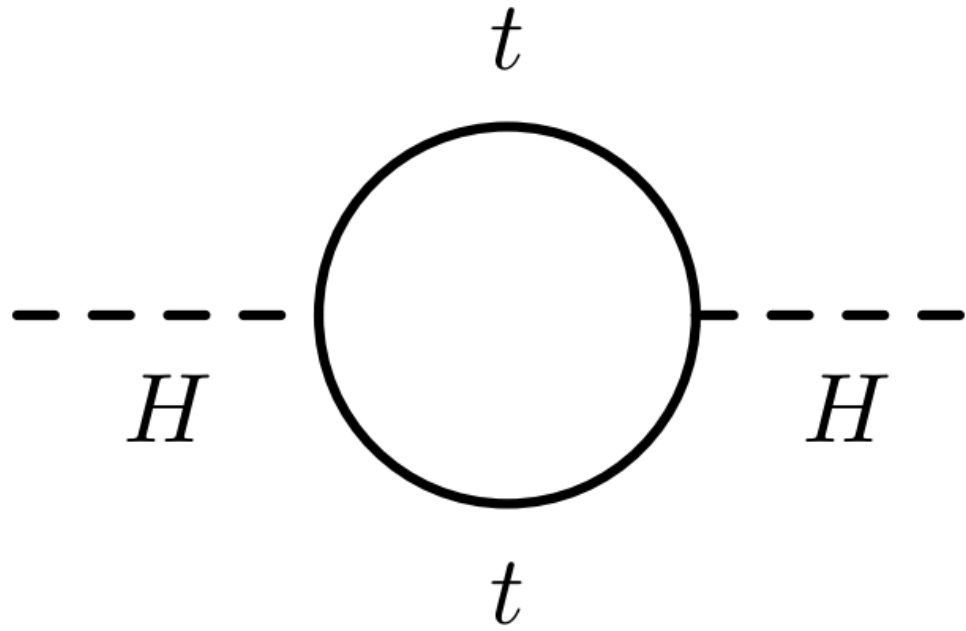


Figure 2.5: The dominant quantum loop correction to the Higgs mass in the Standard Model.

case, we expect the corrections to the Higgs mass like

$$\delta m_H^2 \approx \left( \frac{m_t}{8\pi^2 \langle \phi \rangle_{VEV}} \right)^2 \Lambda_{Planck}^2. \quad (2.17)$$

To achieve the miraculous cancellation required to get the observed Higgs mass of 125 GeV, one needs to then set the bare Higgs mass  $m_0$ , our input to the Standard Model Lagrangian, itself to a *precise* value  $\sim 10^{19}$  GeV. This extraordinary level of parameter finetuning is quite undesirable, and within the framework of the Standard Model, there is little that can be done to alleviate this issue.

An additional concern, of a different nature, is the lack of a *dark matter* candidate in the Standard Model. Dark matter was discovered by observing galactic rotation curves, which showed that much of the matter that interacted gravitationally was invisible to our (electromagnetic) telescopes [16–22]. The postulation of the existence of dark matter, which interacts at least through gravity, allows one to understand these galactic rotation curves. Unfortunately, no particle in the Standard Model could possibly be the dark matter particle. The only candidate truly worth another look is the neutrino, but it has been shown that the neutrino content of the universe is simply too small to explain the galactic rotation curves [22, 64]. The experimental evidence from the galactic rotations curves thus show there *must* be additional physics beyond the Standard Model, which is yet to be understood.

In the next chapter, we will see how these problems can be alleviated by the theory of supersymmetry.

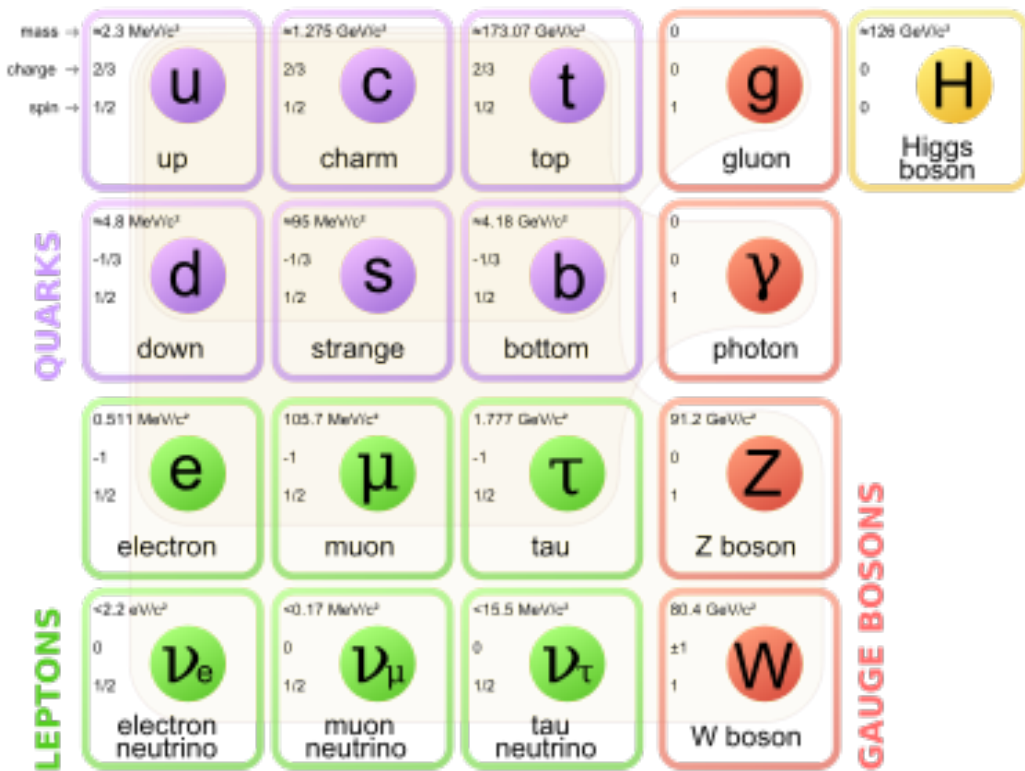


Figure 2.6: Particles of the Standard Model



313

## Chapter 3

---

314

### *Supersymmetry*

315 This chapter will introduce supersymmetry (SUSY) [15, 23–35]. We will begin by  
 316 introducing the concept of a *superspace*, and discuss some general ingredients of  
 317 supersymmetric theories. This will include a discussion of how the problems with the  
 318 Standard Model described in Ch.2 are naturally fixed by these theories.

319 The next step is to discuss the particle content of the *Minimally Supersymmetric*  
 320 *Standard Model* (MSSM). As its name implies, this theory contains the minimal  
 321 additional particle content to make Standard Model supersymmetric. We then discuss  
 322 the important phenomenological consequences of this theory, especially as it would  
 323 be observed in experiments at the LHC.

324 **3.1 Supersymmetric theories : from space to  
 325 superspace**

326 **Coleman-Mandula “no-go” theorem**

327 We begin the theoretical motivation for supersymmetry by citing the “no-go” theorem  
 328 of Coleman and Mandula [65]. This theorem forbids *spin-charge unification*; it  
 329 states that all quantum field theories which contain nontrivial interactions must be  
 330 a direct product of the Poincarégroup of Lorentz symmetries, the internal product  
 331 from of gauge symmetries, and the discrete symmetries of parity, charge conjugation,  
 332 and time reversal. The assumptions which go into building the Coleman-Mandula

theorem are quite restrictive, but there is one unique way out, which has become known as *supersymmetry* [26, 66]. In particular, we must introduce a *spinorial* group generator  $Q$ . Alternatively, and equivalently, this can be viewed as the addition of anti-commuting coordinates; space plus these new anti-commuting coordinates is then called *superspace* [67]. We will not investiage this view in detail, but it is also a quite intuitive and beautiful way to construct supersymmetry[15].

### 339 **Supersymmetry transformations**

340 A *supersymmetric* transformation  $Q$  transforms a bosonic state into a fermionic state,  
 341 and vice versa :

$$Q |\text{Fermion}\rangle = |\text{Boson}\rangle \quad (3.1)$$

$$Q |\text{Boson}\rangle = |\text{Fermion}\rangle \quad (3.2)$$

To ensure this relation holds,  $Q$  must be an anticommuting spinor. Additionally, since spinors are inherently complex,  $Q^\dagger$  must also be a generator of the supersymmetry transformation. Since  $Q$  and  $Q^\dagger$  are spinor objects (with  $s = 1/2$ ), we can see that supersymmetry must be a spacetime symmetry. The Haag-Lopuszanski-Sohnius extension [66] of the Coleman-Mandula theorem [65] is quite restrictive about the forms of such a symmetry. Here, we simply write the (anti-) commutation relations [15] :

$$Q_\alpha, Q_{\dot{\alpha}}^\dagger = -2\sigma_{\alpha\dot{\alpha}\mu} P_\mu \quad (3.3)$$

$$Q_\alpha, Q_{\dot{\beta}} = Q_{\dot{\alpha}}^\dagger, Q_{\dot{\beta}}^\dagger = 0 \quad (3.4)$$

$$[P^\mu, Q_\alpha] = [P^\mu, Q_{\dot{\alpha}}^\dagger] = 0 \quad (3.5)$$

342 **Supermultiplets**

343 In a supersymmetric theory, we organize single-particle states into irreducible  
344 representations of the supersymmetric algebra which are known as *supermultiplets*.  
345 Each supermultiplet contains a fermion state  $|F\rangle$  and a boson state  $|B\rangle$ ; these two  
346 states are the known as *superpartners*. These are related by some combination of  
347  $Q$  and  $Q^\dagger$ , up to a spacetime transformation.  $Q$  and  $Q^\dagger$  commute with the mass-  
348 squared operator  $-P^2$  and the operators corresponding to the gauge transformations  
349 [15]; in particular, the gauge interactions of the Standard Model. In an unbroken  
350 supersymmetric theory, this means the states  $|F\rangle$  and  $|B\rangle$  have exactly the same mass,  
351 electromagnetic charge, electroweak isospin, and color charges. One can also prove  
352 [15] that each supermultiplet contains the exact same number of bosonic ( $n_B$ ) and  
353 fermion ( $n_F$ ) degrees of freedom. We now explore the possible types of supermultiples  
354 one can find in a renormalizable supersymmetric theory.

355 Since each supermultiplet must contain a fermion state, the simplest type of  
356 supermultiplet contains a single Weyl fermion state ( $n_F = 2$ ) which is paired with  
357  $n_B = 2$  scalar bosonic degrees of freedom. This is most conveniently constructed as  
358 single complex scalar field. We call this construction a *scalar supermultiplet* or *chiral*  
359 *supermultiplet*. The second name is indicative; only chiral supermultiplets can contain  
360 fermions whose right-handed and left-handed components transform differently under  
361 the gauge interactions (as of course happens in the Standard Model).

362 The second type of supermultiplet we construct is known as a *gauge* supermul-  
363 tiplet. We take a spin-1 gauge boson (which must be massless due to the gauge  
364 symmetry, so  $n_B = 2$ ) and pair this with a single massless Weyl spinor<sup>1</sup>. The gauge  
365 bosons transform as the adjoint representation of the their respective gauge groups;  
366 their fermionic partners, which are known as gauginos, must also. In particular,  
367 the left-handed and right-handed components of the gaugino fermions have the same

---

<sup>1</sup>Choosing an  $s = 3/2$  massless fermion leads to nonrenormalizable interactions.

368 gauge transformation properties.

369 Excluding gravity, this is the entire list of supermultiplets which can participate  
370 in renormalizable interactions in what is known as  $N = 1$  supersymmetry. This  
371 means there is only one copy of the supersymmetry generators  $Q$  and  $Q^\dagger$ . This is  
372 essentially the only “easy” phenomenological choice, since it is the only choice in four  
373 dimensions which allows for the chiral fermions and parity violations built into the  
374 Standard Model, and we will not look further into  $N > 1$  supersymmetry in this thesis.

375 The primary goal, after understanding the possible structures of the multiplets  
376 above, is to fit the Standard Model particles into a multiplet, and therefore make  
377 predictions about their supersymmetric partners. We explore this in the next section.

## 378 **3.2 Minimally Supersymmetric Standard Model**

379 To construct what is known as the MSSM [15, 68–71], we need a few ingredients and  
380 assumptions. First, we match the Standard Model particles with their corresponding  
381 superpartners of the MSSM. We will also introduce the naming of the superpartners  
382 (also known as *sparticles*). We discuss a very common additional restraint imposed on  
383 the MSSM, known as *R*–parity. We also discuss the concept of soft supersymmetry  
384 breaking and how it manifests itself in the MSSM.

### 385 **Chiral supermultiplets**

386 The first thing we deduce is directly from Sec.???. The bosonic superpartners  
387 associated to the quarks and leptons *must* be spin 0, since the quarks and leptons must  
388 be arranged in a chiral supermultiplet. This is essentially the note above, since the  
389 chiral supermultiplet is the only one which can distinguish between the left-handed  
390 and right-handed components of the Standard Model particles. The superpartners of  
391 the quarks and leptons are known as *squarks* and *sleptons*, or *sfermions* in aggregate.

392 (for ‘‘scalar quarks’’, ‘‘scalar leptons’’, and ‘‘scalar fermion’’<sup>2</sup>). The ‘‘s-’’ prefix  
 393 can also be added to the individual quarks i.e. *selectron*, *sneutrino*, and *stop*. The  
 394 notation is to add a  $\sim$  over the corresponding Standard Model particle i.e.  $\tilde{e}$ , the  
 395 selectron is the superpartner of the electron. The two-component Weyl spinors of the  
 396 Standard Model must each have their own (complex scalar) partner i.e.  $e_L, e_R$  have  
 397 two distinct partners :  $\tilde{e}_L, \tilde{e}_R$ . As noted above, the gauge interactions of any of the  
 398 sfermions are identical to those of their Standard Model partners.

Due to the scalar nature of the Higgs, it must obviously lie in a chiral supermultiplet. To avoid gauge anomalies and ensure the correct Yukawa couplings to the quarks and leptons[15], we must add additional Higgs bosons to any supersymmetric theory. In the MSSM, we have two chiral supermultiplets. The SM (SUSY) parts of the multiplets are denoted  $H_u(\tilde{H}_u)$  and  $H_d(\tilde{H}_d)$ . Writing out  $H_u$  and  $H_d$  explicitly:

$$H_u = \begin{pmatrix} H_u^+ \\ H_u^0 \end{pmatrix} \quad (3.6)$$

$$H_d = \begin{pmatrix} H_d^0 \\ H_d^- \end{pmatrix} \quad (3.7)$$

(3.8)

399 we see that  $H_u$  looks very similar to the SM Higgs with  $Y = 1$ , and  $H_d$  is symmetric  
 400 to this with  $+ \rightarrow -$ , with  $Y = -1$ . The SM Higgs boson,  $h_0$ , is a linear superposition  
 401 of the neutral components of these two doublets. The SUSY parts of the Higgs  
 402 multiplets,  $\tilde{H}_u$  and  $\tilde{H}_d$ , are each left-handed Weyl spinors. For generic spin-1/2  
 403 sparticles, we add the ‘‘-ino’’ suffix. We then call the partners of the two Higgs  
 404 collectively the *Higgsinos*.

---

<sup>2</sup>The last one should probably have bigger scare quotes.

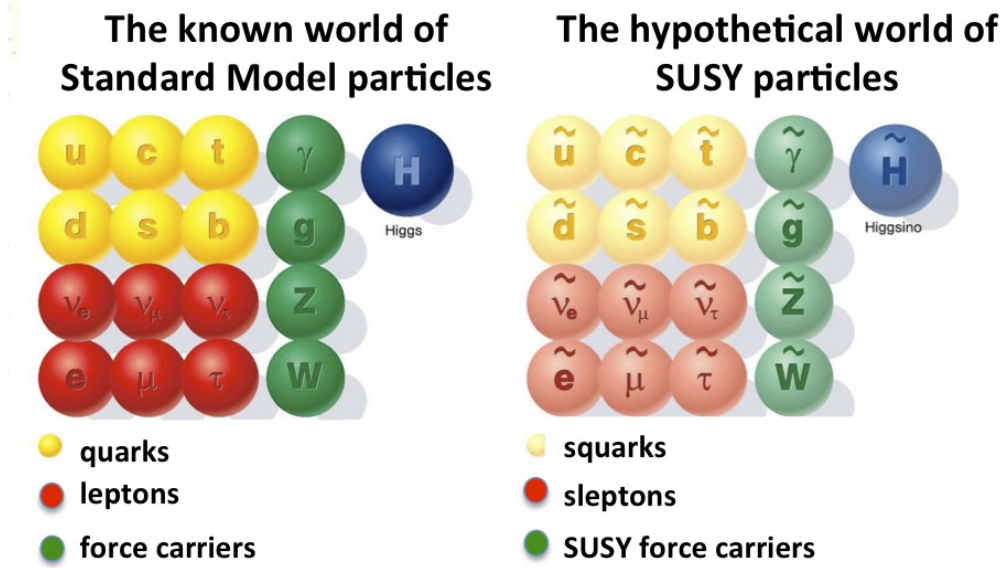


Figure 3.1: Particles of the MSSM

## 405 Gauge supermultiplets

406 The superpartners of the gauge bosons must all be in gauge supermultiplets since  
 407 they contain a spin-1 particle. Collectively, we refer to the superpartners of the  
 408 gauge bosons as the gauginos.

409 The first gauge supermultiplet contains the gluon, and its superpartner, which is  
 410 known as the *gluino*, denoted  $\tilde{g}$ . The gluon is of course the SM mediator of  $SU(3)_C$ ;  
 411 the gluino is also a colored particle, subject to  $SU(3)_C$ . From the SM before EWSB,  
 412 we have the four gauge bosons of the electroweak symmetry group  $SU(2)_L \otimes U(1)_Y$  :  
 413  $W^{1,2,3}$  and  $B^0$ . The superpartners of these particles are thus the *winos*  $W^{\tilde{1},\tilde{2},\tilde{3}}$  and  
 414 *bino*  $\tilde{B}^0$ , where each is placed in another gauge supermultiplet with its corresponding  
 415 SM particle. After EWSB, without breaking supersymmetry, we would also have the  
 416 zino  $\tilde{Z}^0$  and photino  $\tilde{\gamma}$ .

417 The entire particle content of the MSSM can be seen in Fig.3.1.

418 At this point, it's important to take a step back. Where are these particles?  
 419 As stated above, supersymmetric theories require that the masses and all quantum



Figure 3.2: This Feynmann diagram shows how proton decay is induced in the MSSM, if one does not impose  $R$ -parity.

420 numbers of the SM particle and its corresponding sparticle are the same. Of course,  
 421 we have not observed a selectron, squark, or wino. The answer, as it often is, is that  
 422 supersymmetry is *broken* by the vacuum state of nature [15].

423  **$R$ -parity**

This section is a quick aside to the general story.  $R$  – parity refers to an additional discrete symmetry which is often imposed on supersymmetric models. For a given particle state, we define

$$R = (-1)^{3(B-L)+2s} \quad (3.9)$$

424 where  $B, L$  is the baryon (lepton) number and  $s$  is the spin. The imposition of  
 425 this symmetry forbids certain terms from the MSSM Lagrangian that would violate  
 426 baryon and/or lepton number. This is required in order to prevent proton decay, as  
 427 shown in Fig.3.2<sup>3</sup>. .

428 In supersymmetric models, this is a  $\mathbb{Z}_2$  symmetry, where SM particles have  $R = 1$   
 429 and sparticles have  $R = -1$ . We will take  $R$  – parity as part of the definition of  
 430 the MSSM. We will discuss later the *drastic* consequences of this symmetry on SUSY  
 431 phenomenology

---

<sup>3</sup>Proton decay can actually be prevented by allowing only one of the four potential R-parity violating terms to survive.

432 **Soft supersymmetry breaking**

The fundamental idea of *soft* supersymmetry breaking[15, 34, 35, 72, 73] is that we would like to break supersymmetry without reintroducing the quadratic divergences we discussed at the end of Chapter 2. We write the Lagrangian in a form :

$$\mathcal{L}_{\text{MSSM}} = \mathcal{L}_{\text{SUSY}} + \mathcal{L}_{\text{soft}} \quad (3.10)$$

433 In this sense, the symmetry breaking is “soft”, since we have separated out the  
 434 completely symmetric terms from those soft terms which will not allow the quadratic  
 435 divergences to the Higgs mass.

436 The explicitly allowed terms in the soft-breaking Lagrangian are [35].

- 437 • Mass terms for the scalar components of the chiral supermultipletss  
 438 • Mass terms for the Weyl spinor components of the gauge supermultipletss  
 439 • Trilinear couplings of scalar components of chiral supermultiplets

In particular, using the field content described above for the MSSM, the softly-broken portion of the MSSM Lagrangian can be written

$$\mathcal{L}_{\text{soft}} = -\frac{1}{2} \left( M_3 \tilde{g} \tilde{g} + M_2 \tilde{W} \tilde{W} + M_1 \tilde{B} \tilde{B} + c.c. \right) \quad (3.11)$$

$$- \left( \tilde{u} a_u \tilde{Q} H_u - \tilde{d} a_d \tilde{Q} H_d - \tilde{e} a_e \tilde{L} H_d + c.c. \right) \quad (3.12)$$

$$- \tilde{Q}^\dagger m_Q^2 \tilde{Q} - \tilde{L}^\dagger m_L^2 \tilde{L} - \tilde{u} m_u^2 \tilde{u}^\dagger - \tilde{d} m_d^2 \tilde{d}^\dagger - \tilde{e} m_e^2 \tilde{e}^\dagger \quad (3.13)$$

$$- m_{H_u}^2 H_u^* H_u - m_{H_d}^2 H_d^* H_d - (b H_u H_d + cc). \quad (3.14)$$

440 where we have introduced the following notations :

441 1.  $M_3, M_2, M_1$  are the gluino, wino, and bino masses.

442 2.  $a_u, a_d, a_e$  are complex  $3 \times 3$  matrices in family space.

443 3.  $m_Q^2, m_u^2, m_d^2, m_L^2, m_e^2$  are hermitian  $3 \times 3$  matrices in family space.

444 4.  $m_{H_u}^2, m_{H_d}^2, b$  are the SUSY-breaking contributions to the Higgs potential.

445 We have written matrix terms without any sort of additional notational decoration  
 446 to indicate their matrix nature, and we now show why. The first term 1 are  
 447 straightforward; these are just the straightforward mass terms for these fields. There  
 448 are strong constraints on the off-diagonal terms for the matrices of 2 [74, 75]; for  
 449 simplicity, we will assume that each  $a_i, i = u, d, e$  is proportional to the Yukawa  
 450 coupling matrix :  $a_i = A_{i0}y_i$ . The matrices in ?? can be similarly constrained by  
 451 experiments [68, 75–82] Finally, we assume that the elements 4 contributing to the  
 452 Higgs potential as well as all of the 1 terms must be real, which limits the possible  
 453 CP-violating interactions to those of the Standard Model. We thus only consider  
 454 flavor-blind, CP-conserving interactions within the MSSM.

The important mixing for mass and gauge interaction eigenstates in the MSSM occurs within electroweak sector, in a process akin to EWSB in the Standard Model. The neutral portions of the Higgsinos doublets and the neutral gauginos  $(\tilde{H}_u^0, \tilde{H}_d^0, \tilde{B}^0, \tilde{W}^0)$  of the gauge interaction basis mix to form what are known as the *neutralinos* of mass basis :

$$M_{\tilde{\chi}} = \begin{pmatrix} M_1 & 0 & -c_\beta s_W m_Z & s_\beta s_W m_Z \\ 0 & M_2 & c_\beta c_W m_Z & -s_\beta c_W m_Z \\ -c_\beta s_W m_Z & c_\beta c_W m_Z & 0 & -\mu \\ s_\beta s_W m_Z & -s_\beta c_W m_Z & -\mu & 0 \end{pmatrix} \quad (3.15)$$

455 where  $s(c)$  are the sine and cosine of angles related to EWSB, which introduced  
 456 masses to the gauginos and higgsinos. Diagonalization of this matrix gives the four  
 457 neutralino mass states, listed without loss of generality in order of increasing mass :  
 458  $\tilde{\chi}_{1,2,3,4}^0$ .

459 The neutralinos, especially the lightest neutralino  $\tilde{\chi}_1^0$ , are important ingredients  
 460 in SUSY phenomenology.

461     The same process can be done for the electrically charged gauginos with  
462     the charged portions of the Higgsino doublets along with the charged winos  
463      $(\tilde{H}_u^+, \tilde{H}_d^+, \tilde{W}^+, \tilde{W}^-)$ . This leads to the *charginos*, again in order of increasing mass  
464     :  $\tilde{\chi}_{1,2}^\pm$ .

465     

### 3.3 Phenomenology

466     We are finally at the point where we can discuss the phenomenology of the MSSM,  
467     in particular as it manifests itself at the energy scales of the LHC.

468     As noted above in Sec.3.2, the assumption of *R*–parity has important conse-  
469     quences for MSSM phenomenology. The SM particles have  $R = 1$ , while the sparticles  
470     all have  $R = -1$ . Simply, this is the “charge” of supersymmetry. Since the particles of  
471     LHC collisions ( $pp$ ) have total incoming  $R = 1$ , we must expect that all sparticles will  
472     be produced in *pairs*. An additional consequence of this symmetry is the fact that the  
473     lightest supersymmetric particle (LSP) is *stable*. Off each branch of the Feynmann  
474     diagram shown in Fig., we have  $R = -1$ , and this can only decay to another sparticle  
475     and a SM particle. Once we reach the lightest sparticle in the decay, it is absolutely  
476     stable. This leads to the common signature  $E_T^{\text{miss}}$  for a generic SUSY signal.

477     For this thesis, we will be presenting an inclusive search for squarks and gluinos  
478     with zero leptons in the final state. This is a very interesting decay channel<sup>4</sup>, due  
479     to the high cross-sections of  $\tilde{g}\tilde{g}$  and  $\tilde{q}\tilde{q}$  decays, as can be seen in Fig.?? [83]. This  
480     is a direct consequence of the fact that these are the colored particles of the MSSM.  
481     Since the sparticles interact with the gauge groups of the SM in the same way as their  
482     SM partners, the colored sparticles, the squarks and gluinos, are produced and decay  
483     as governed by the color group  $SU(3)_C$  with the strong coupling  $g_S$ . The digluino  
484     production is particularly copious, due to color factor corresponding to the color octet

---

<sup>4</sup>Prior to Run1, probably the most *most* interesting SUSY decay channel.

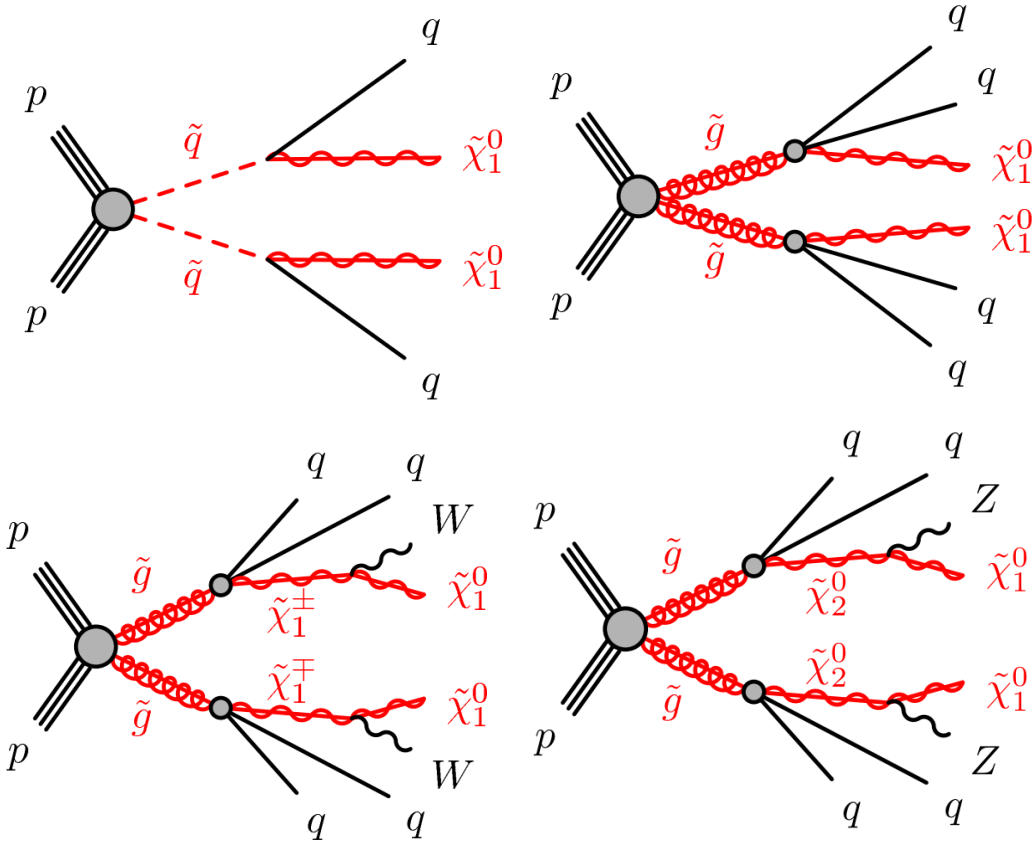


Figure 3.3: SUSY signals considered in this thesis

485 of  $SU(3)C$ .

486 In the case of disquark production, the most common decay mode of the squark in  
 487 the MSSM is a decay directly to the LSP plus a single SM quark [15]. This means the  
 488 basic search strategy of disquark production is two jets from the final state quarks,  
 489 plus missing transverse energy for the LSPs. There are also cascade decays, the most  
 490 common of which, and the only one considered in this thesis, is  $\tilde{q} \rightarrow q\chi_1^\pm \rightarrow qW^\pm\chi_1^0$ .

491 For digluino production, the most common decay is  $\tilde{g} \rightarrow g\tilde{q}$ , due to the large  
 492  $g_S$  coupling. The squark then decays as listed above. In this case, we generically  
 493 search for four jets and missing transverse energy from the LSPs. We can also have  
 494 the squark decay in association with a  $W^\pm$  or  $Z^0$ ; in this thesis, we are interested in  
 495 those cases where this vector boson goes hadronically.

496 In the context of experimental searches for SUSY, we often consider *simplified*

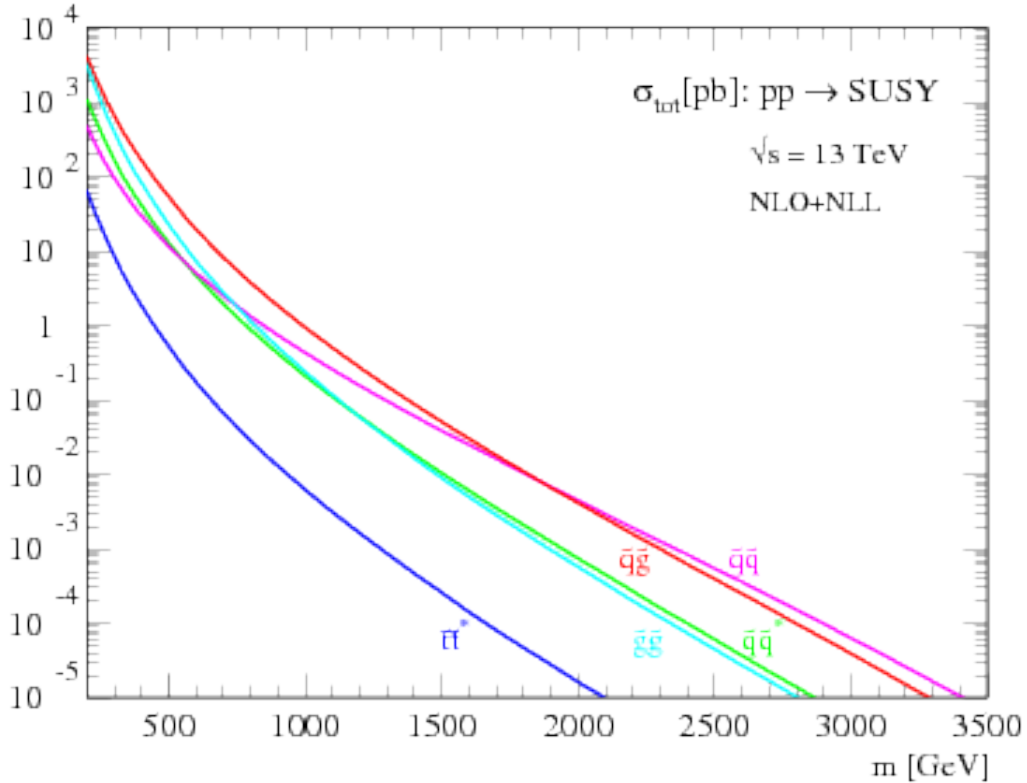


Figure 3.4: SUSY production cross-sections as a function of sparticle mass at  $\sqrt{s} = 13$  TeV.

497 *models*. These models make certain assumptions which allow easy comparisons of  
 498 results by theorists and rival experimentalists. In the context of this thesis, the  
 499 simplified models will make assumptions about the branching ratios described in the  
 500 preceding paragraphs. In particular, we will often choose a model where the decay of  
 501 interest occurs with 100% branching ratio. This is entirely for ease of interpretation  
 502 by other physicists<sup>5</sup>, but it is important to recognize that these are more a useful  
 503 comparison tool, especially with limits, than a strict statement about the potential  
 504 masses of sought-after beyond the Standard Model particle.

---

<sup>5</sup>In the author's opinion, this often leads to more confusion than comprehension. We will revisit the shortcomings of simplified models in the Conclusion to this thesis.

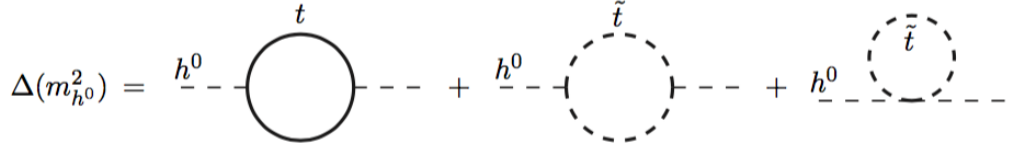


Figure 3.5: Loop diagrams correct the Higgs mass in the MSSM

## 505 3.4 How SUSY solves the problems with the SM

506 We now return to the issues with the Standard Model as described in Ch.2 to see  
 507 how these issues are solved by supersymmetry.

### 508 Quadratic divergences to the Higgs mass

The quadratic divergences induced by the loop corrections to the Higgs mass, for example from the top Yukawa coupling, goes as

$$\delta m_H^2 \approx \left( \frac{m_t}{8\pi^2 \langle \phi \rangle_{VEV}} \right)^2 \Lambda_{Planck}^2. \quad (3.16)$$

509 The miraculous thing about SUSY is each of these terms *automatically* comes  
 510 with a term which exactly cancels this contribution[15]. The fermions and bosons  
 511 have opposite signs in this loop diagram to all orders in perturbation theory, which  
 512 completely solves the hierarchy problem. This is the most well-motivated reason for  
 513 supersymmetry.

### 514 Gauge coupling unification

515 An additional motivation for supersymmetry is seen by the gauge coupling unification  
 516 high scales. In the Standard Model, as we saw the gauge couplings fail to unify at  
 517 high energies. In the MSSM and many other forms of supersymmetry, the gauge  
 518 couplings unify at high energy, as can be seen in Fig.???. This provides additional  
 519 aesthetic motivation for supersymmetric theories.



Figure 3.6: The running of Standard Model gauge couplings; compare to Fig.2.4. The MSSM gauge couplings nearly intersect at high energies.

## 520 Dark matter

521 As we discussed previously, the lack of any dark matter candidate in the Standard  
 522 Model naturally leads to beyond the Standard Model theories. In the Standard Model,  
 523 there is a natural dark matter candidate in the lightest supersymmetric particle[15]  
 524 The LSP would in dark matter experiments be called a *weakly-interacting massive*  
 525 *particle* (WIMP), which is a type of cold dark matter [22, 84]. These WIMPS would  
 526 only interact through the weak force and gravity, which is exactly as a model like the  
 527 MSSM predicts for the neutralino. In Fig.3.7, we can see the current WIMP exclusions  
 528 for a given mass. The range of allowed masses which have not been excluded for LSPs  
 529 and WIMPs have significant overlap. This provides additional motivation outside of  
 530 the context of theoretical details.



Figure 3.7: WIMP exclusions from direct dark matter detection experiments.

### 531 3.5 Conclusions

532 Supersymmetry is the most well-motivated theory for physics beyond the Standard  
 533 Model. It provides a solution to the hierarchy problem, leads to gauge coupling  
 534 unification, and provides a dark matter candidate consistent with galactic rotation  
 535 curves. As noted in this chapter, due to the LSPs in the final state, most SUSY  
 536 searches require a significant amount of missing transverse energy in combination  
 537 with jets of high transverse momentum. However, there is some opportunity to do  
 538 better than this, especially in final states where one has two weakly-interacting LSPs  
 539 on opposite sides of some potentially complicated decay tree. We will see how this is  
 540 done in Ch.??.



541

## Chapter 4

---

542

### *The Large Hadron Collider*

543 The Large Hadron Collider (LHC) produces high-energy protons which are collided  
 544 at the center of multiple large experiments at CERN on the outskirts of Geneva,  
 545 Switzerland [85]. The LHC produces the highest energy collisions in the world,  
 546 with design center-of-mass energy of  $\sqrt{s} = 14$  TeV, which allows the experiments  
 547 to investigate physics far beyond the reach of previous colliders. This chapter will  
 548 summarize the basics of accelerator physics, especially with regards to discovering  
 549 physics beyond the Standard Model. We will describe the CERN accelerator complex  
 550 and the LHC.

551 **4.1 Basics of Accelerator Physics**

552 This section follows closely the presentation of [86].

Simple particle accelerators simply rely on the acceleration of charged particles in a static electric field. Given a field of strength  $E$ , charge  $q$ , and mass  $m$ , this is simply

$$a = \frac{qE}{m}. \quad (4.1)$$

553 For a given particle with a given mass and charge, this is limited by the static electric  
 554 field which can be produced, which in turn is limited by electrical breakdown at high  
 555 voltages.

556 There are two complementary solutions to this issue. First, we use the *radio*  
 557 *frequency acceleration* technique. We call the devices used for this *RF cavities*. The

558    cavities produce a time-varied electric field, which oscillate such that the charged  
 559    particles passing through it are accelerated towards the design energy of the RF  
 560    cavity. This oscillation also induces the particles into *bunches*, since particles which  
 561    are slightly off in energy from that induced by the RF cavity are accelerated towards  
 562    the design energy.

Second, one bends the particles in a magnetic field, which allows them to pass through the same RF cavity over and over. This second process is often limited by *synchrotron radiation*, which describes the radiation produced when a charged particle is accelerated. The power radiated is

$$P \sim \frac{1}{r^2} \left( E/m \right)^4 \quad (4.2)$$

563    where  $r$  is the radius of curvature and  $E, m$  is the energy (mass) of the charged  
 564    particle. Given an energy which can be produced by a given set of RF cavities (which  
 565    is *not* limited by the mass of the particle), one then has two options to increase the  
 566    actual collision energy : increase the radius of curvature or use a heavier particle.  
 567    Practically speaking, the easiest options for particles in a collider are protons and  
 568    electrons, since they are (obviously) copious in nature and do not decay<sup>1</sup>. Given the  
 569    dependence on mass, we can see why protons are used to reach the highest energies.  
 570    The tradeoff for this is that protons are not point particles, and we thus we don't  
 571    know the exact incoming four-vectors of the protons, as discussed in Ch.2.

The particle *beam* refers to the bunches all together. An important property of a beam of a particular energy  $E$ , moving in uniform magnetic field  $B$ , containing particles of momentum  $p$  is the *beam rigidity* :

$$R \equiv rB = p/c. \quad (4.3)$$

572    The linear relation between  $r$  and  $p$ , or alternatively  $B$  and  $p$  have important  
 573    consequences for LHC physics. For hadron colliders, this is the limiting factor on

---

<sup>1</sup>Muon colliders are a really cool option at high energies, since the relativistic  $\gamma$  factor gives them a relatively long lifetime in the lab frame.

574 going to higher energy scales; one needs a proportionally larger magnetic field to  
575 keep the beam accelerating in a circle.

576 Besides the rigidity of the beam, the most important quantities to characterize  
577 a beam are known as the (normalized) *emittance*  $\epsilon_N$  and the *betatron function*  $\beta$ .  
578 These quantities determine the transverse size  $\sigma$  of a relativistic beam  $v \gtrsim c$  beam :  
579  $\sigma^2 = \beta^* \epsilon_N / \gamma_{\text{rel}}$ , where  $\beta^*$  is the value of the betatron function at the collision point  
580 and  $\gamma_{\text{rel}}$  is the Lorentz factor.

These quantities determine the *instantaneous luminosity*  $L$  of a collider, which combined with the cross-section  $\sigma$  of a particular physics process, give the rate of this physics process :

$$R = L\sigma. \quad (4.4)$$

The instantaneous luminosity  $L$  is given by :

$$L = \frac{f_{\text{rev}} N_b^2 F}{4\pi\sigma^2} = \frac{f_{\text{rev}} n N_b^2 \gamma_{\text{rel}} F}{4\pi\beta^* \epsilon_N}. \quad (4.5)$$

581 Here we have introduced the frequency of revolutions  $f_{\text{rev}}$ , the number of bunches  $n$ ,  
582 the number of protons per bunch  $N_b^2$ , and a geometric factor  $F$  related to the crossing  
583 angle of the beams.

The *integrated luminosity*  $\int L$  gives the total number of a particular physics process  $P$ , with cross-section  $\sigma_P$ .

$$N_P = \sigma_P \int L. \quad (4.6)$$

584 Due to this simple relation, one can also quantify the “amount of data delivered” by  
585 a collider simply by  $\int L$ .

## 586 4.2 Accelerator Complex

587 The Large Hadron Collider is the last accelerator in a chain of accelerators which  
588 together form the CERN accelerator complex, which can be seen in 4.1. The protons



Figure 4.1: The CERN accelerator complex.

begin their journey to annihilation in a hydrogen source, where they are subsequently ionized. The first acceleration occurs in the Linac 2, a linear accelerator composed of RF cavities. The protons leave the Linac 2 at an energy of 50 MeV and enter the Proton Synchrotron Booster (PSB). The PSB contains four superimposed rings, which accelerate the protons to 1.4 GeV. The protons are then injected into the Proton Synchrotron (PS). This synchrotron increases the energy up to 25 GeV. After leaving the PS, the protons enter the Super Proton Synchrotron (SPS). This is the last step before entering the LHC ring, and the protons are accelerated to 450 GeV. From the SPS, the protons are injected into the beam pipes of the LHC. The process to fill the LHC rings with proton bunches from start to finish typically takes about four minutes.

## 600 4.3 Large Hadron Collider

The Large Hadron Collider is the final step in the CERN accelerator complex, and produces the collisions analyzed in this thesis. From the point of view of experimentalists on the general-purpose ATLAS and CMS experiments, the main goal of the LHC is to deliver collisions at the highest possible energy, with the highest possible instantaneous luminosity. The LHC was installed in the existing 27 km tunnel used by the Large Electron Positron (LEP) collider [87]. This allowed the existing accelerator complex at CERN, described in the previous section, to be used as the injection system to prepare the protons up to 450 GeV. Many aspects of the LHC design were decided by this very fact, and specified the options allowed to increase the energy or luminosity. In particular, the radius of the tunnel was already specified; from Eq.4.3, this implies the momentum (or energy) of the beam is entirely determined by the magnetic field. Given the 27 km circumference of the LEP tunnel, one can calculate the required magnetic field to reach the 7 TeV per proton design energy of the LHC :

$$r = C/2\pi = 4.3 \text{ km} \quad (4.7)$$

$$\rightarrow B = \frac{p}{rc} = 5 \text{ T} \quad (4.8)$$

601 In fact, the LHC consists of 8 528 m straight portions consisting of RF cavities, used  
602 to accelerate the particles, and 8 circular portions which bend the protons around the  
603 LHC ring. These circular portions actually have a slightly smaller radius of curvature  
604  $r = 2804 \text{ m}$ , and we require  $B = 8.33 \text{ T}$ . To produce this large field, we need to use  
605 superconducting magnets, as discussed in the next section.

## 606 Magnets

607 There are many magnets used by the LHC machine, but the most important are the  
608 1232 dipole magnets; a schematic is shown in Fig.4.2 and a photograph is shown in



Figure 4.2: Schematic of an LHC dipole magnet.

609 Fig.4.3.

610 The magnets are made of Niobium and Titanium. The maximum field strength is  
 611 10 T when cooled to 1.9 Kelvin. The magnets are cooled by superfluid helium, which  
 612 is supplied by a large cryogenic system. Due to heating between the eight helium  
 613 refrigerators and the beampipe, the helium is cooled in the refrigerators to 1.8 K.

614 A failure in the cooling system can cause what is known as a *quench*. If the  
 615 temperature goes above the critical superconducting temperature, the metal loses its  
 616 superconducting properties, which leads to a large resistance in the metal. This leads  
 617 to rapid temperature increases, and can cause extensive damages if not controlled.

618 The dipole magnets are 16.5 meters long with a diameter of 0.57 meters. There  
 619 are two individual beam pipes inside each magnet, which allows the dipoles to house  
 620 the beams travelling in both directions around the LHC ring. They curve slightly,  
 621 at an angle of 5.1 mrad, which carefully matches the curvature of the ring. The

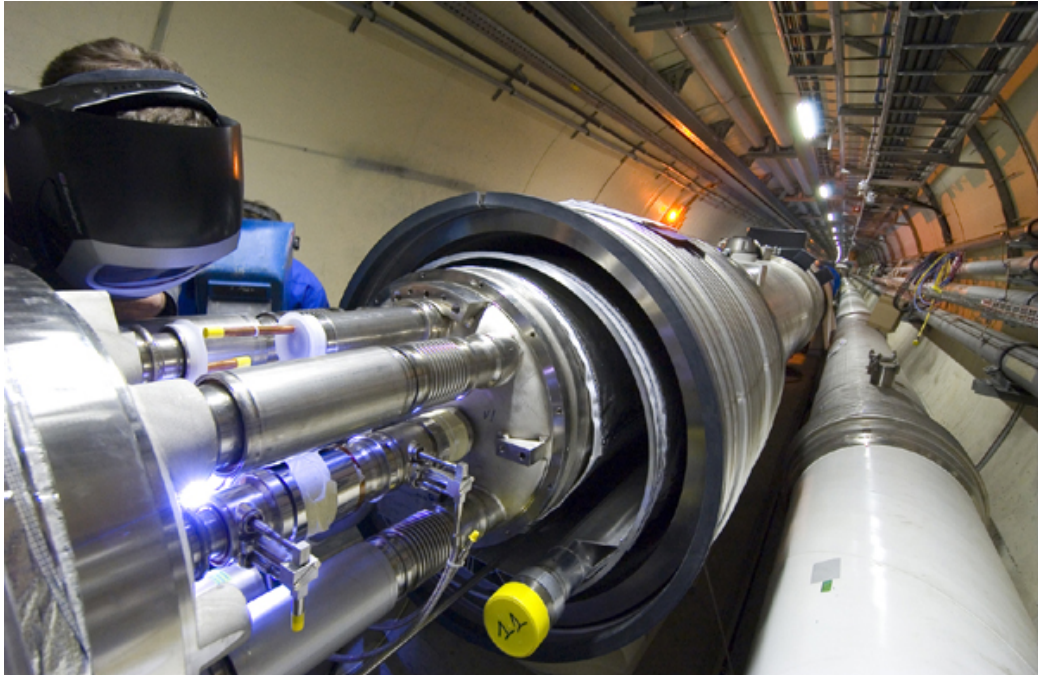


Figure 4.3: Photograph of a technician connecting an LHC dipole magnet.

622 beampipes inside of the magnets are held in high vacuum, to avoid stray particles  
623 interacting with the beam.

## 624 **4.4 Dataset Delivered by the LHC**

625 In this thesis, we analyze the data delivered by the LHC to ATLAS in the 2015 and  
626 2016 datasets. The beam parameters relevant to this dataset are available in Table  
627 [4.1](#).

628 The peak instantaneous luminosity delivered in 2015 (2016) was  $L =$   
629  $5.2(11) \text{ cm}^{-2}\text{s}^{-1} \times 10^{33}$ . One can note that the instantaneous luminosity delivered in  
630 the 2016 dataset exceeds the design luminosity of the LHC. The total integrated  
631 luminosity delivered was  $13.3 \text{ fb}^{-1}$ . In Figure [4.4](#), we display the integrated luminosity  
632 as a function of day for 2015 and 2016.

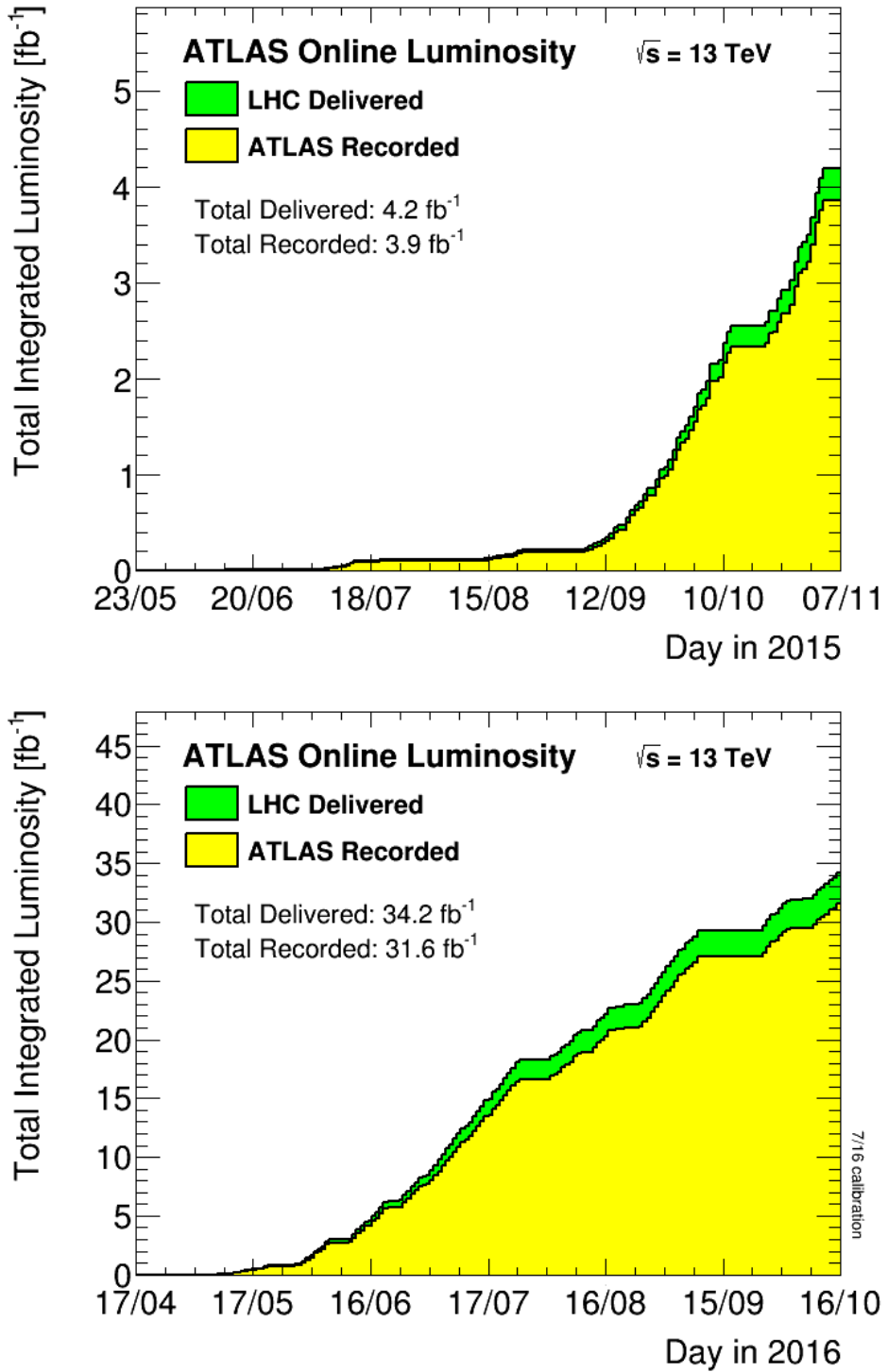


Figure 4.4: Integrated Luminosity delivered by the LHC and collected by ATLAS in the 2015 and 2016 datasets.

Parameter	Injection	Extraction
Energy (GeV)	450	7000
Rigidity (T-m)	3.8	23353
Bunch spacing (ns)	25	25
Design Luminosity ( $\text{cm}^{-2}\text{s}^{-1} \times 10^3$ )	-	1.0
Bunches per proton beam	2808	2808
Protons per bunch	1.15 e11	1.15 e11
Beam lifetime (hr)	-	10
Normalized Emittance $\epsilon_N$ (mm $\mu\text{rad}$ )	3.3	3.75
Betatron function at collision point $\beta^*$ (cm)	-	55

Table 4.1: Beam parameters of the Large Hadron Collider.

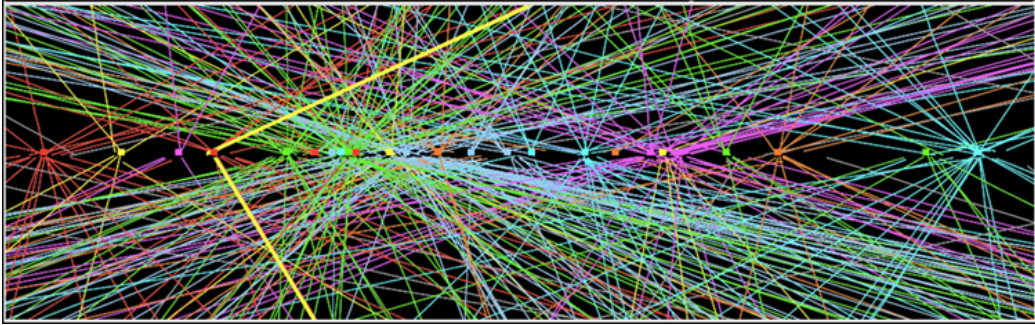


Figure 4.5: Simulated event with many pileup vertices.

## 633 Pileup

634 *Pileup* is the term for the additional proton-proton interactions which occur during  
 635 each bunch crossing of the LHC. At the beginning of the LHC physics program, there  
 636 had not been a collider which averaged more than a single interaction per bunch  
 637 crossing. In the LHC, each bunch crossing (or *event*) generally contains multiple  
 638 proton-proton interactions. An simulated event with many *vertices* can be seen in  
 639 Fig.4.5. The so-called *primary vertex* (or *hard scatter vertex*) refers to the vertex  
 640 which has the highest  $\Sigma p_T^2$ ; this summation occurs over the *tracks* in the detector,  
 641 which we will describe later[**ATL-INDET-PUB-2009-001**]. We then distinguish  
 642 between *in-time* pileup and *out-of-time* pileup. In-time pileup refers to the additional  
 643 proton-proton interactions which occur in the event. Out-of-time pileup refers to  
 644 effects related to proton-proton interactions previous bunch crossings.

645        We quantify in-time pileup by the number of “primary”<sup>2</sup> vertices in a particular  
646    event. To quantify the out-of-time pileup, we use the average number of interactions  
647    per bunch crossing  $\langle \mu \rangle$  over some human-scale time. In Figure 4.6, we show the  
648    distribution of  $\mu$  for the dataset used in this thesis.

---

<sup>2</sup>The primary vertex is as defined above, but we unfortunately use the same name here.



Figure 4.6: Mean number of interactions per bunch crossing in the 2015 and 2016 datasets.



*The ATLAS detector*

651 The dataset analyzed in this thesis was taken by the ATLAS detector [88], which is  
 652 located at the “Point 1” cavern of the LHC beampipe, just across the street from  
 653 the main CERN campus. The much-maligned acronym stands for *A Toroidal LHC*  
 654 *ApparatuS*. ATLAS is a massive cylindrical detector, with a radius of 12.5 m and a  
 655 length of 44 m, with nearly hermitic coverage around the collision point. It consists  
 656 of multiple subdetectors; each plays a role in ATLAS’s ultimate purpose of measuring  
 657 the energy, momentum, and type of the particles produced in collisions delivered by  
 658 the LHC. These subdetectors are immersed in a hybrid solenoid-toroid magnet system  
 659 whichs forces charged particles to curve, which allows for precise measurements of  
 660 their momenta. These magnetic fields are maximized in the central solenoid magnet,  
 661 which contains a magnetic field of 2 T. A schematic of the detector can be seen in  
 662 [5.1](#).

663 The *inner detector* (ID) lies closest to the collision point, and contains three  
 664 separate subdetectors. It provides pseudorapidity<sup>1</sup>coverage of  $|\eta| < 2.5$  for charged  
 665 particles to interact with the tracking material. The tracks reconstructed from the  
 666 inner detector hits are used to reconstruct the primary vertices, as noted in Ch.??,

---

<sup>1</sup>ATLAS uses a right-handed Cartesian coordinate system; the origin is defined by the nominal beam interaction point. The positive- $z$  direction is defined by the incoming beam travelling counterclockwise around the LHC. The positive- $x$  direction points towards the center of the LHC ring from the origin, and the positive- $y$  direction points upwards towards the sky. For particles of transverse (in the  $x - y$  plane) momentum  $p_T = \sqrt{p_x^2 + p_y^2}$  and energy  $E$ , it is generally most convenient fully describe this particle’s kinematics as measured by the detector in the  $(p_T, \phi, \eta, E)$  basis. The angle  $\phi = \arctan(p_y/p_x)$  is the standard azimuthal angle, and  $\eta = \ln \tan(\theta/2)$  is known as the pseudorapidity, and defined based on the standard polar angle  $\theta = \arccos(p_z/p_T)$ . For locations of i.e. detector elements, both  $(r, \phi, \eta)$  and  $(z, \phi, \eta)$  can be useful.



Figure 5.1: The ATLAS detector

and to determine the momemta of charged particles. The ATLAS *calorimeter* consists of two subdetectors, known as the *electromagnetic* and *hadronic* calorimeters. These detectors stop particles in their detector material, and measure the energy deposition inside, which measures the energy of the particles deposited. The calorimeters provide coverage out to pseudorapidity of  $|\eta| < 4.9$ . The muon spectrometer is aptly named; it is specifically used for muons, which are the only particles which generally reach the outer portions of the detector. In this region, we have the large tracking systems of the muon spectrometer, which provide precise measurements of muon momenta. The muon spectrometer has pseudorapidity coverage of  $|\eta| < 2.7$ .

## 5.1 Magnets

ATLAS contains multiple magnetic systems; primarily, we are concerned with the solenoid, used by the inner detector, and the toroids located outside of the ATLAS calorimeter. A schematic is shown in Fig.5.2. These magnetic fields are used to bend

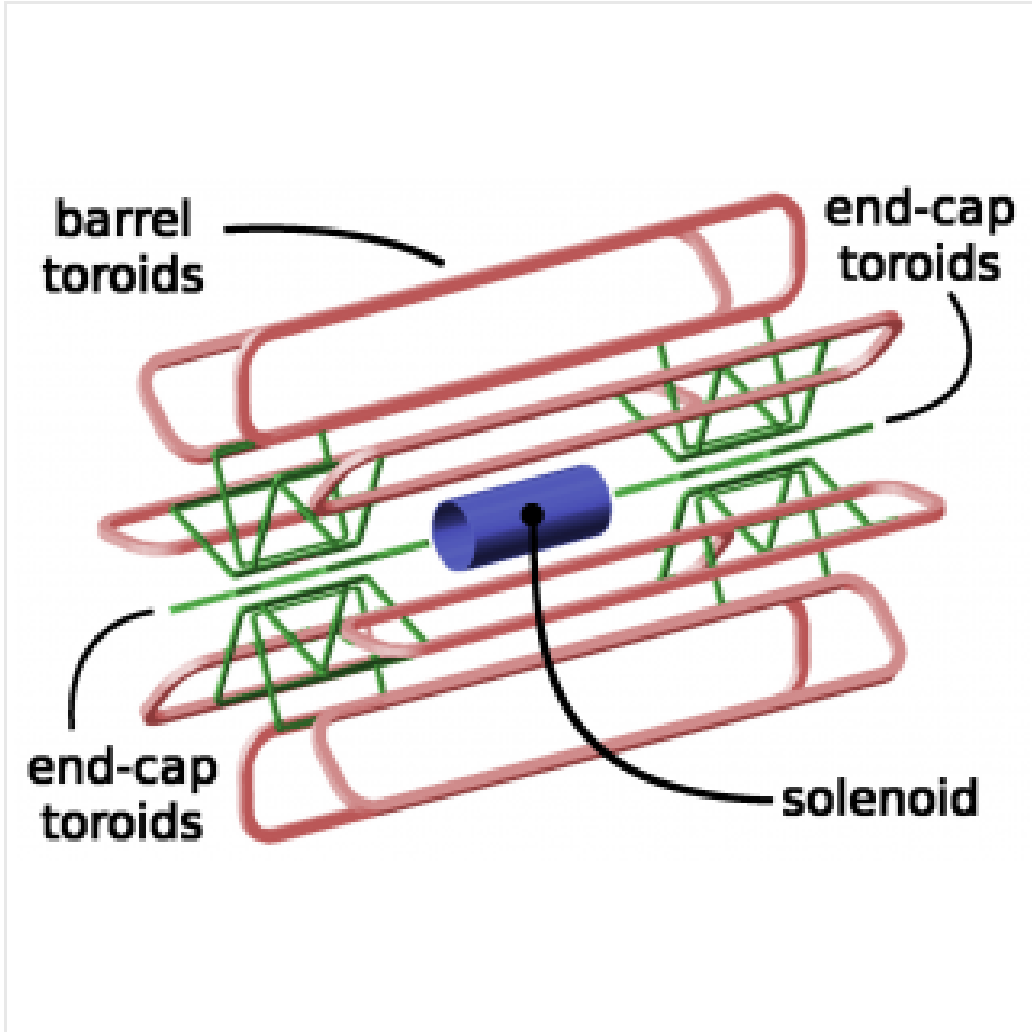


Figure 5.2: The ATLAS magnet system

680 charged particles under the Lorentz force, which subsequently allows one to measure  
681 their momentum.

682 The ATLAS central solenoid is a 2.3 m diameter, 5.3 m long solenoid at the center  
683 of the ATLAS detector. It produces a uniform magnetic field of 2 T; this strong field  
684 is necessary to accurately measure the charged particles in this field. An important  
685 design constraint for the central solenoid was the decision to place it in between the  
686 inner detector and the calorimeters. To avoid excessive impacts on measurements in  
687 the calorimetry, the central solenoid must be as transparent as possible<sup>2</sup>.

---

<sup>2</sup>This is also one of the biggest functional differences between ATLAS and CMS; in CMS, the



Figure 5.3: The ATLAS inner detector

688     The toroid system consists of eight air-core superconducting barrel loops; these  
 689    give ATLAS its distinctive shape. There are also two endcap air-core magnets. These  
 690    produce a magnetic field in a region of approximately 26 m in length and 10 m of  
 691    radius. The magnetic field in this region is non-uniform, due to the prohibitive costs  
 692    of a solenoid magnet of that size.

## 693    **5.2 Inner Detector**

694    The ATLAS inner detector consists of three separate tracking detectors, which are  
 695    known as, in order of increasing distance from the interaction point, the Pixel  
 696    Detector, Semiconductor Tracker (SCT), and the Transition Radiation Tracker  
 697    (TRT). When charged particles pass through these tracking layers, they produce  
 698    *hits*, which using the known 2 T magnetic field, allows the reconstruction of *tracks*.  
 699    Tracks are used as inputs for reconstruction of many higher-level physics objects,

---

solenoid is outside of the calorimeters.

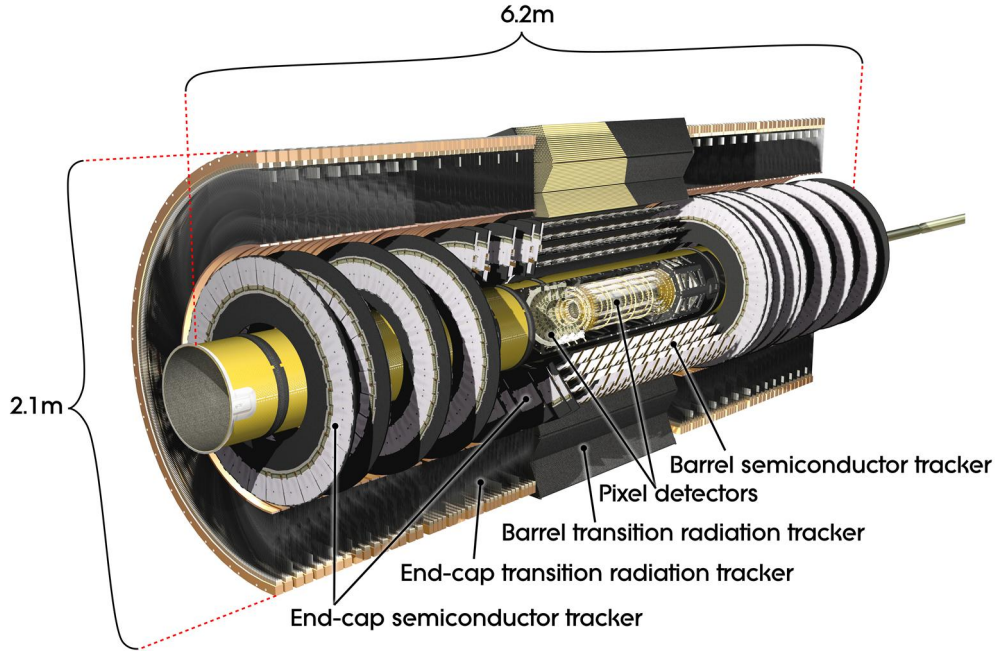


Figure 5.4: The ATLAS pixel detector

such as electrons, muons, photons, and  $E_T^{\text{miss}}$ . Accurate track reconstruction is thus crucial for precise measurements of charged particles.

## Pixel Detector

The ATLAS pixel detector consists four layers of silicon “pixels”. This refers to the segmentation of the active medium into the pixels; compare to the succeeding silicon detectors, which will use silicon “strips”. This provides precise 3D hit locations. The layers are known as the “Insertable”<sup>3</sup>B-Layer (IBL), the B-Layer (or Layer-0), Layer-1, and Layer-2, in order of increasing distance from the interaction point. These layers are very close to the interaction point, and therefore experience a large amount of radiation.

Layer-1, Layer-2, and Layer-3 were installed with the initial construction of ATLAS. They contain front-end integrated electronics (FEI3s) bump-bonded to 1744

---

<sup>3</sup>Very often, the IBL is mistakenly called the Inner B-Layer, which would have been a much more sensible name.

712 silicon modules; each module is  $250 \mu\text{m}$  in thickness and contains 47232 pixels. These  
713 pixels have planar sizes of  $50 \times 400 \mu\text{m}^2$  or  $50 \times 600 \mu\text{m}^2$ , to provide highly accurate  
714 location information. The FEI3s are mounted on long rectangular structures known  
715 as staves, which encircle the beam pipe. A small tilt to each stave allows full coverage  
716 in  $\phi$  even with readout systems which are installed. These layers are at radia of 50.5  
717 mm, 88.5 mm, and 122.5 mm from the interaction point.

718 The IBL was added to ATLAS after Run1 in 2012 at a radius of 33 mm from the  
719 interaction point. The entire pixel detector was removed from the center of ATLAS  
720 to allow an additional pixel layer to be installed. The IBL was required to preserve  
721 the integrity of the pixel detector as radiation damage leads to inoperative pixels in  
722 the other layers. The IBL consists of 448 FEI4 chips, arranged onto 14 staves. Each  
723 FEI4 has 26880 pixels, of planar size  $50 \times 250 \mu\text{m}$ . This smaller granularity was  
724 required due to the smaller distance to the interaction point.

725 In total, a charged particle passing through the inner detector would expect to  
726 leave four hits in the pixel detector.

## 727 Semiconductor Tracker

728 The SCT is directly beyond Layer-2 of the pixel detector. This is a silicon strip  
729 detector, which do not provide the full 3D information of the pixel detector. The  
730 dual-sensors of the SCT contain  $2 \times 768$  individual strips; each strip has area  $6.4$   
731  $\text{cm}^2$ . The SCT dual-sensor is then double-layered, at a relative angle of 40 mrad;  
732 together these layers provide the necessary 3D information for track reconstruction.  
733 There are four of these double-layers, at radia of 284 mm, 355 mm, 427 mm, and 498  
734 mm. These double-layers provide hits comparable to those of the pixel detector, and  
735 we have four additional hits to reconstruct tracks for each charged particle.

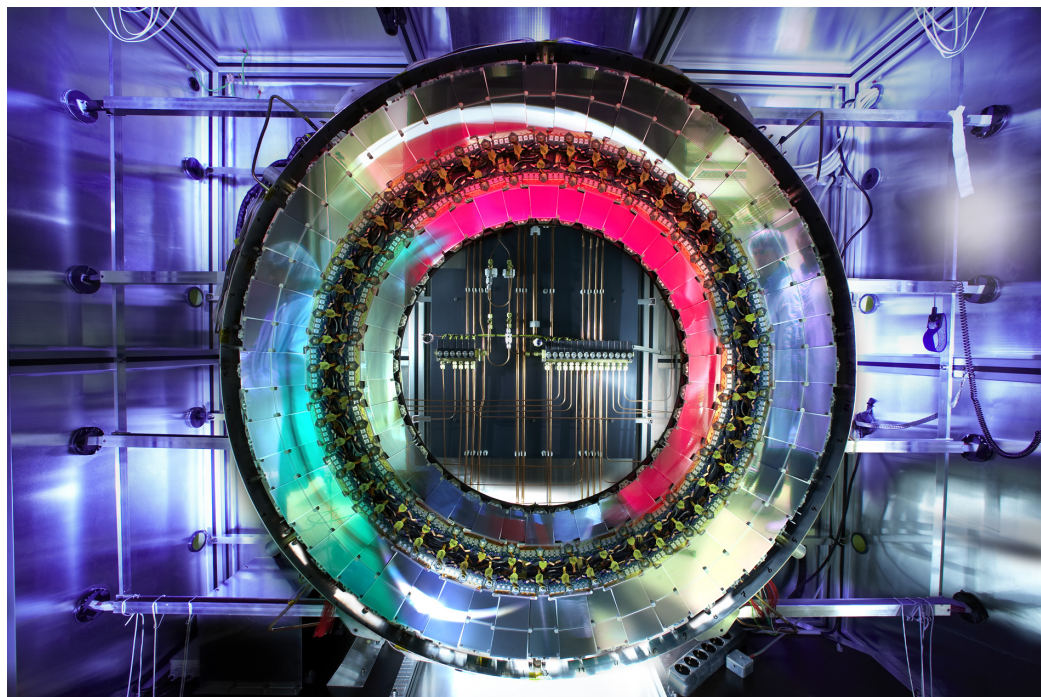


Figure 5.5: A ring of the Semiconductor Tracker

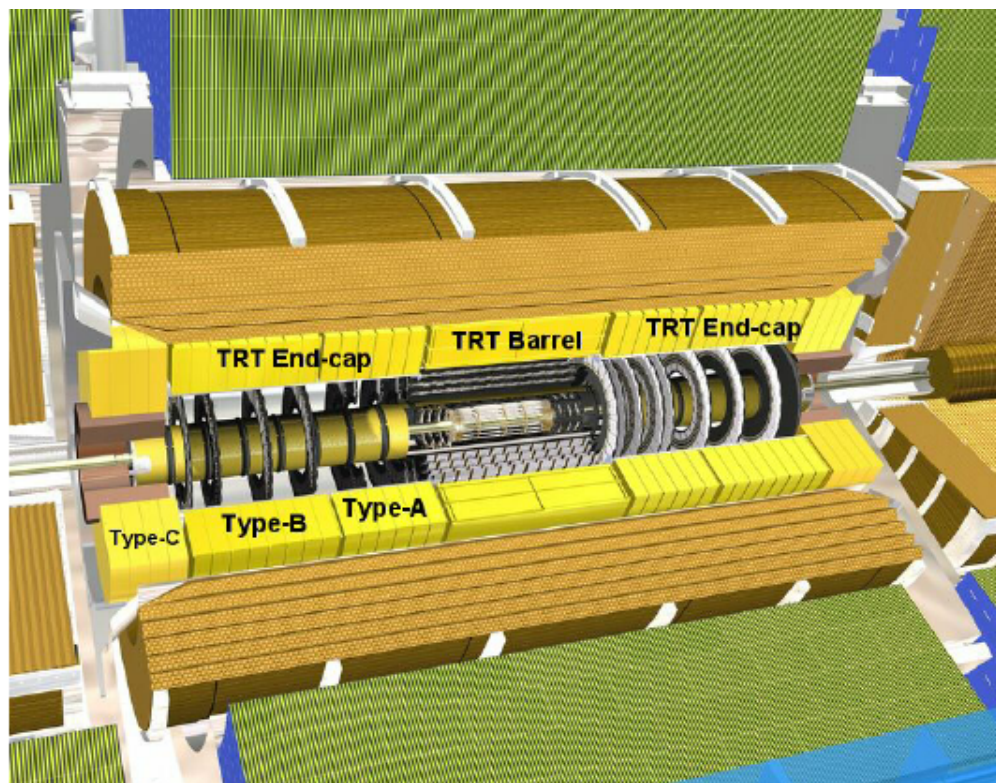


Figure 5.6: A schematic of the Transition Radiation Tracker

736 **Transition Radiation Tracker**

737 The Transition Radiation Tracker is the next detector radially outward from the SCT.  
738 It contains straw drift tubes; these contain a tungsten gold-plated wire of  $32 \mu\text{m}$   
739 diameter held under high voltage (-1530 V) with the edge of the Kapton-aluminum  
740 tube. They are filled with a gas mixture of primarily xenon that is ionized when  
741 a charged particle passes through the tube. The ions are collected by the “drift”  
742 due to the voltage inside the tubes, which is read out by the electronics. This gives  
743 so-called “continuous tracking” throughout the tube, due to the large number of ions  
744 produced.

745 The TRT is so-named due to the *transition radiation* (TR) it induces. Due to  
746 the dielectric difference between the gas and tubes, TR is induced. This is important  
747 for distinguishing electrons from their predominant background of minimum ionizing  
748 particles. Generally, electrons have a much larger Lorentz factor than minimum  
749 ionizing particles, which leads to additional TR. This can be used as an additional  
750 handle for electron reconstruction.

751 **5.3 Calorimetry**

752 The calorimetry of the ATLAS detector also includes multiple subdetectors; these sub-  
753 detectors allow precise measurements of the electrons, photons, and hadrons produced  
754 by the ATLAS detector. Generically, calorimeters work by stopping particles in their  
755 material, and measuring the energy deposition. This energy is deposited as a cascade  
756 particles induce from interactions with the detector material known *showers*. ATLAS  
757 uses *sampling* calorimeters; these alternate a dense absorbing material, which induces  
758 showers, with an active layer which measures energy depositions by the induced  
759 showers. Since some energy is deposited into the absorption layers as well, the energy  
760 depositions must be properly calibrated for the detector.

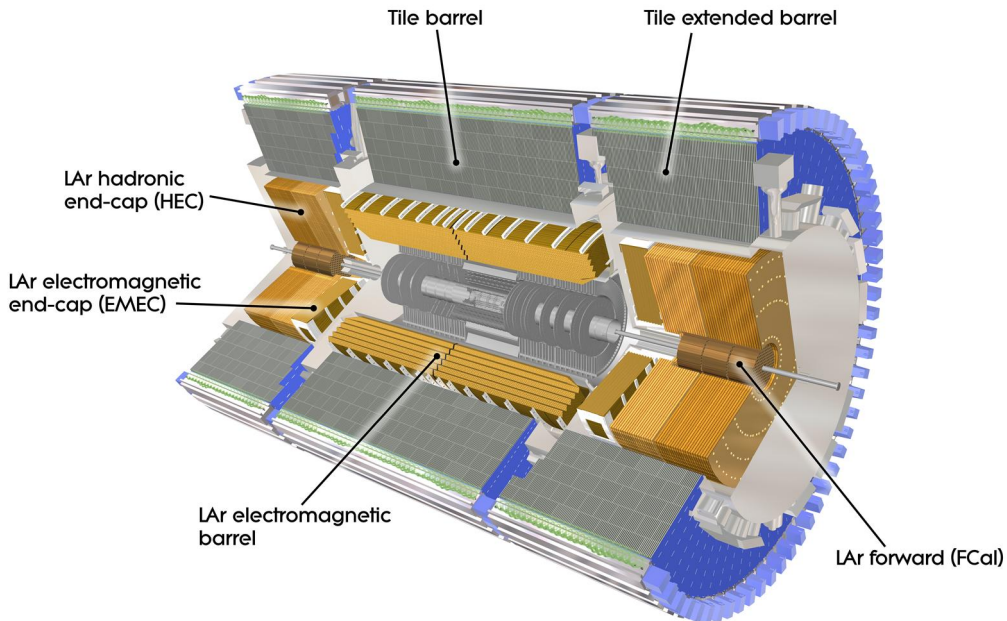


Figure 5.7: The ATLAS calorimeter

761 Electromagnetic objects (electrons and photons) and hadrons have much different  
 762 interaction properties, and thus we need different calorimeters to accurately measure  
 763 these different classes of objects; we can speak of the *electromagnetic* and *hadronic*  
 764 calorimeters. ATLAS contains four separate calorimeters : the liquid argon (LAr)  
 765 electromagnetic barrel calorimeter, the Tile barrel hadronic calorimeter, the LAr  
 766 endcap electromagnetic calorimeter, the LAr endcap hadronic calorimeter, and the  
 767 LAr Forward Calorimeter (FCal). Combined, these provide full coverage in  $\phi$  up to  
 768  $|\eta| < 4.9$ , and can be seen in Fig.5.7.

769 **Electromagnetic Calorimeters**

770 The electromagnetic calorimeters of the ATLAS detector consist of the barrel and  
 771 endcap LAr calorimeters. These are arranged into an ingenious “accordion” shape,  
 772 shown in 5.8, which allows full coverage in  $\phi$  and exceptional coverage in  $\eta$  while  
 773 still allowing support structures for detector operation. The accordion is made of



Figure 5.8: A schematic of a subsection of the barrel LAr electromagnetic calorimeter

774 layers with liquid argon (active detection material) and lead (absorber) to induce  
 775 electromagnetic showers. The LAr EM calorimeters are each more than 20 radiation  
 776 lengths deep, which provides the high stopping power necessary to properly measure  
 777 the electromagnetic showers.

778 The barrel component of the LAr EM calorimeter extends from the center of the  
 779 detector out to  $|\eta| < 1.475$ . The calorimeter has a presampler, which measures the  
 780 energy of any EM shower induced before the calorimeter. This has segmentation of  
 781  $\Delta\eta = 0.025, \Delta\phi = .01$ . There are three “standard” layers in the barrel, which have  
 782 decreasing segmentation into calorimeter *cells* as one travels radially outward from  
 783 the interaction point. The first layer has segmentation of  $\Delta\eta = 0.003, \Delta\phi = .1$ , and  
 784 is quite thin relative to the other layers at only 4 radiation lengths deep. It provides  
 785 precise  $\eta$  and  $\phi$  measurements for incoming EM objects. The second layer is the  
 786 deepest at 16 radiation lengths, with a segmentation of  $\Delta\eta = 0.025, \Delta\phi = 0.025$ . It



Figure 5.9: A schematic of Tile hadronic calorimeter

is primarily responsible for stopping the incoming EM particles, which dictates its large relative thickness, and measures most of the energy of the incoming particles. The third layer is only 2 radiation lengths deep, with a rough segmentation of  $\Delta\eta = 0.05$ ,  $\Delta\phi = .025$ . The deposition in this layer is primarily used to distinguish hadrons interacting electromagnetically and entering the hadronic calorimeter from the strictly EM objects which are stopped in the second layer.

The barrel EM calorimeter has a similar overall structure, but extends from  $1.4 < |\eta| < 3.2$ . The segmentation in  $\eta$  is better in the endcap than the barrel; the  $\phi$  segmentation is the same. In total, the EM calorimeters contain about 190000 individual calorimeter cells.

## Hadronic Calorimeters

The hadronic calorimetry of ATLAS sits directly outside the EM calorimetry. It contains three subdetectors : the barrel Tile calorimeter, the endcap LAr calorimeter,

800 and the Forward LAr Calorimeter. Similar to the EM calorimeters, these are  
801 sampling calorimeters that alternate steel (dense material) with an active layer  
802 (plastic scintillator).

803 The barrel Tile calorimeter extends out to  $|\eta| < 1.7$ . There are again three layers,  
804 which combined give about 10 interactions length of distance, which provides excellent  
805 stopping power for hadrons. This is critical to avoid excess *punchthrough* to the muon  
806 spectrometer beyond the hadronic calorimeters. The first layer has a depth of 1.5  
807 interaction lengths. The second layer is again the thickest at a depth of 4.1 interaction  
808 lengths; most of the energy of incoming particle is deposited here. Both the first and  
809 second layer have segmentation of about  $\Delta\eta = 0.1, \Delta\phi = 0.1$ . Generally, one does not  
810 need as fine of granularity in the hadronic calorimeter, since the energy depositions  
811 in the hadronic calorimeters will be summed into the composite objects we know as  
812 jets. The third layer has a thickness of 1.8 interaction lengths, with a segmentation of  
813  $\Delta\eta = 0.2, \Delta\phi = 0.1$ . The use of multiple layers allows one to understand the induced  
814 hadronic shower as it propagates through the detector material.

815 The endcap LAr hadronic calorimeter covers the region  $1.5 < |\eta| < 3.2$ . It is  
816 again a sampling calorimeter; the active material is LAr with a copper absorbed. It  
817 does not use the accordion shape of the other calorimeters; it has a “standard” flat  
818 shape perpendicular to the interaction point. The segmentation varies with  $\eta$ . For  
819  $1.5 < |\eta| < 2.5$ , the cells are  $\Delta\eta = 0.1, \Delta\phi = 0.1$ ; in the region  $2.5 < |\eta| < 3.2$ , the  
820 cells are  $\Delta\eta = 0.2, \Delta\phi = 0.2$  in size.

821 The final calorimeter in ATLAS is the forward LAr calorimeter. Of those  
822 subdetectors which are used for standard reconstruction techniques, the FCal sits  
823 at the most extreme values of  $3.1 < |\eta| < 4.9$ . The FCal itself is made of three  
824 subdetectors; FCal1 is actually an electromagnetic module, while FCal2 and FCal3  
825 are hadronic. The absorber in FCal1 is copper, with a liquid argon active medium.  
826 FCal2 and FCal3 also use a liquid argon active medium, with a tungsten absorber.

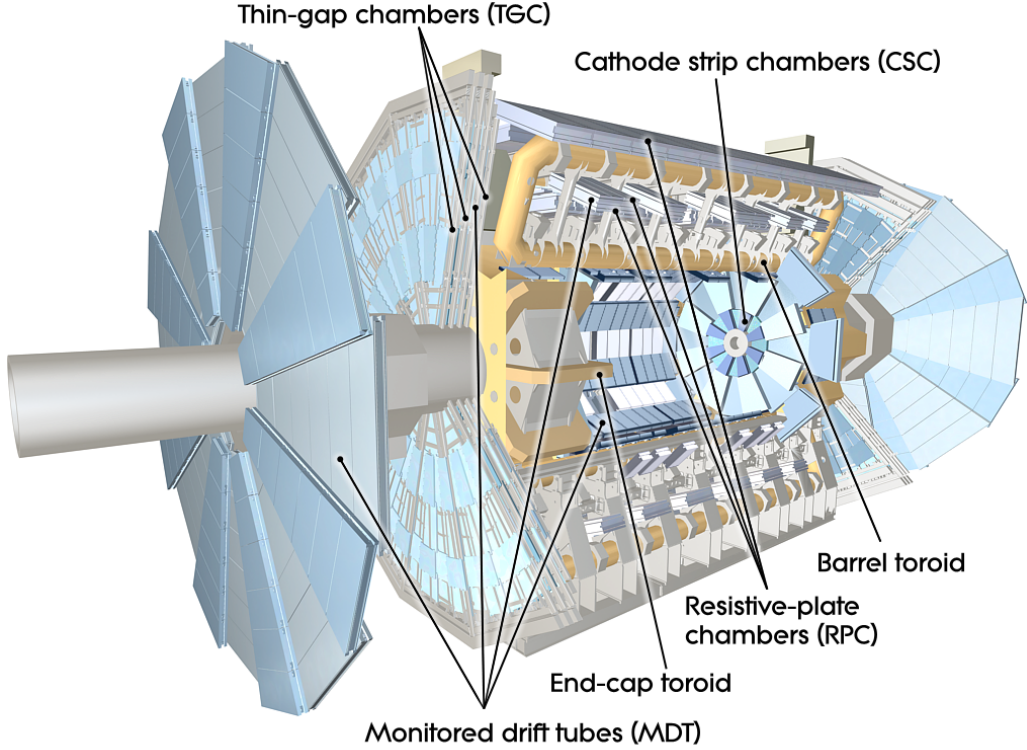


Figure 5.10: The ATLAS muon spectrometer

## 827 5.4 Muon Spectrometer

828 The muon spectrometer is the final major subdetector of the ATLAS detector.  
829 The muon spectrometer sits outside the hadronic calorimetry, with pseudorapidity  
830 coverage out to  $|\eta| < 2.7$ . The MS is a huge detector, with some detector elements  
831 existing as far as 11 m in radius from the interaction point. This system is used  
832 almost exclusively to measure the momenta of muons; these are the only measured  
833 SM particles which consistently exit the hadronic calorimeters. These systems provide  
834 a rough measurement, which is used in triggering (described in Ch.5.5), and a precise  
835 measurement to be used in offline event reconstruction as described in Ch.???. The  
836 MS produces tracks in a similar way to the ID; the hits in each subdetector are  
837 recorded and then tracks are produced from these hits. Muon spectrometer tracks are  
838 largely independent of the ID tracks due to the independent solenoidal and toroidal  
839 magnet systems used in the ID and MS respectively. The MS consists of four separate

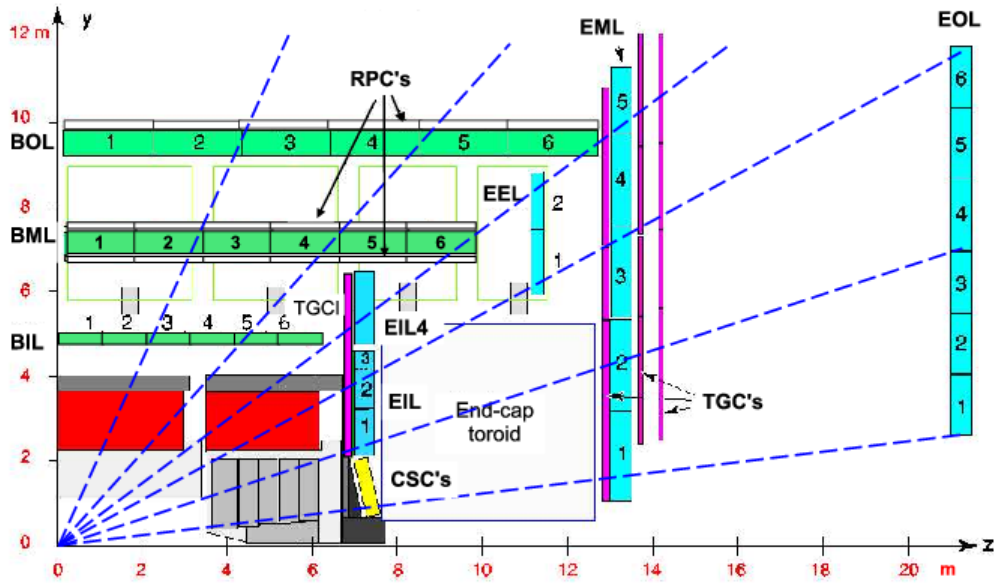


Figure 5.11: A schematic in  $z/\eta$  showing the location of the subdetectors of the muon spectrometer

840 subdetectors: the barrel region is covered by the Resistive Plate Chambers (RPCs)  
 841 and Monitored Drift Tubes (MDTs) while the endcaps are covered by MDTs, Thin  
 842 Gap Chambers (TGCs), and Cathode Strip Chambers (CSCs).

### 843 Monitored Drift Tubes

844 The MDT system is the largest individual subdetector of the MS. MDTs provide  
 845 precision measurements of muon momenta as well as fast measurements used for  
 846 triggers. There are 1088 MDT chambers providing coverage out to pseudorapidity  
 847  $|\eta| < 2.7$ ; each consists of an aluminum tube containing an argon- $\text{CO}_2$  gas mixture.  
 848 In the center of each tube there  $50\mu\text{m}$  diameter tungsten-rhenium wire at a voltage of  
 849 3080 V. A muon entering the tube will induce ionization in the gas, which will “drift”  
 850 towards the wire due to the voltage. One measures this ionization as a current in the  
 851 wire; this current comes with a time measurement related to how long it takes the  
 852 ionization to drift to the wire.

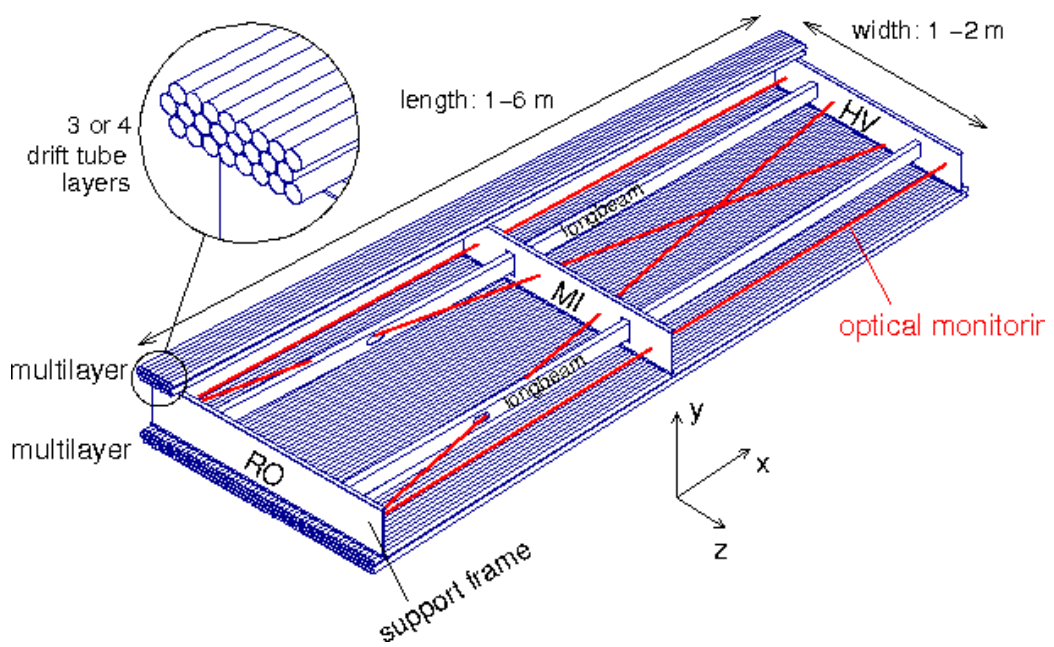


Figure 5.12: Schematic of a Muon Drift Tube chamber

853 These tubes are layered in a pattern shown in Fig.5.12. Combining the measure-  
854 ments from the tubes in each layer gives good position resolution. The system consists  
855 of three subsystems of these layers, at 5 m, 7m, and 9 m from the interaction point.  
856 The innermost layer is directly outside the hadronic calorimeter. The combination of  
857 these three measurements gives precise momenta measurements for muons.

## 858 Resistive Plate Chambers

859 The RPC system is alternated with the MDT system in the barrel; the first two layers  
860 of RPC detectors surround the second MDT layer while the third is outside the final  
861 MDT layer. The RPC system covers pseudorapidity  $|\eta| < 1.05$ . Each RPC consists  
862 of two parallel plates at a distance of 2 mm surrounding a  $\text{C}_2\text{H}_2\text{F}_4$  mixture. The  
863 electric field between these plates is 4.9k kV/mm. Just as in the MDTs, an incoming  
864 muon ionizes the gas, and the deposited ionization is collected by the detector (in this  
865 case on the plates). It is quite fast, but with a relatively poor spatial resolution of  
866 1 cm. Still, it can provide reasonable  $\phi$  resolution due to its large distance from the  
867 interaction point. This is most useful in triggering, where the timing requirements are  
868 quite severe. The RPCs are also complement the MDTs by providing a measurement  
869 of the non-bending coordinate.

## 870 Cathode Strip Chambers

871 The CSCs are used in place of MDTs in the first layer of the endcaps. This region, at  
872  $2.0 < |\eta| < 2.7$ , has higher particle multiplicity at the close distance to the interaction  
873 point from low-energy photons and neutrons. The MDTs were not equip to deal with  
874 the higher particle rate of this region, so the CSCs were designed to deal with this  
875 deficiency.

876 Each CSC consists multiwire proportional chambers, oriented radially outward  
877 from the interaction point. These chambers overlap partially in  $\phi$ . The wires contain



Figure 5.13: Photo of the installation of Cathode Strip Chambers and Monitored Drift Tubes

878 a gas mixture of argon and CO<sub>2</sub>, which is ionized when muons enter. The detectors  
879 operate with a voltage of 1900 V, with much lower drift times than the MDTs. They  
880 provide less hits than MDTs, but their lower drift times lower uptime and reduce the  
881 amount of detector overload.

882 The CSCs are arranged into four planes on the wheels of the muon spectrometer,  
883 as seen in Fig.???. There are 32 CSCs in total, with 16 on each side of the detector  
884 in  $\eta$ .

### 885 **Thin Gap Chambers**

886 The TGCs serve the purpose of the RPCs in the endcap at pseudorapidity of  $1.05 <$   
887  $|\eta| < 2.4$ ; they provide fast measurements used in triggering. The TGCs are also  
888 multiwire proportional chambers a la the CSCs. The fast readouts necessary for  
889 trigger are provided by a high electric field and a small wire-to-wire distance of 1.8  
890 mm. These detectors provide both  $\eta$  and  $\phi$  information, allowing the trigger to use  
891 as much information as possible when selecting events.



Figure 5.14: Photo of a muon Big Wheel, consisting of Thin Gap Chambers

## 892 5.5 Trigger System

893 The data rate delivered by the LHC is staggering [89]. In the 2016 dataset, the  
894 collision rate was 40 MHz, meaning a *bunch spacing* of 25 ns. In each of the event,  
895 as we saw in Ch.??, there are many proton-proton collisions. Most of the collisions  
896 are uninteresting, such as elastic scattering of protons, or even inelastic scattering  
897 leading to low-energy dijet events. These types of events have been studied in detail  
898 in previous experiments.

899 Even if one is genuinely interested in these events, it's *impossible* to save all of  
900 the information available in each event. If all events were written "to tape" (as the  
901 jargon goes), ATLAS would store terabytes of data per second. We are limited to only  
902 about 1000 Hz readout by computing processing time and storage space. We thus  
903 implement a *trigger* which provides fast inspection of events to drastically reduce  
904 the data rate from the 40 MHz provided by the LHC to the 1000 Hz we can write to  
905 tape for further analysis.

906       The ATLAS trigger system consists of a two-level trigger, known as the Level-  
907       1 trigger (L1 trigger) and the High-Level Trigger (HLT)<sup>4</sup>. Trigger selections are  
908       organized into *trigger chains*, where events passing a particular L1 trigger are passed  
909       to a corresponding HLT trigger. For example, one would require a particular high- $p_T$   
910       muon at L1, with additional quality requirements at HLT. One can also use HLT  
911       triggers as prerequisites for each other, as is done in some triggers requiring both jets  
912       and  $E_T^{\text{miss}}$ .

## 913       **Level-1 Trigger**

914       The L1 trigger is hardware-based, and provides the very fast rejection needed to  
915       quickly select events of interest. The L1 trigger uses only what is known as *prompt*  
916       data to quickly identify interesting events. Only the calorimeters and the triggering  
917       detectors (RPCs and TGCs) of the MS are fast enough to be considered at L1,  
918       since the tracking reconstruction algorithms used by the ID and the more precise  
919       MS detectors are very slow. This allows quick identification of events with the  
920       most interesting physical objects : large missing transverse momentum and high-  
921        $p_T$  electrons, muons, and jets.

922       L1 trigger processing is done locally. This means that events are selected without  
923       considering the entire available event. Energy deposits over some threshold are  
924       reconstructed as *regions of interest*. These RoIs are then compared using pattern  
925       recognition hardware to “expected” patterns for the given RoIs. Events with RoIs  
926       matching these expected patterns are then handed to the HLT through the Central  
927       Trigger Processor. This step alone lowers the data rate down by about three orders  
928       of magnitude.

---

<sup>4</sup>In Run1, ATLAS ran with a three-level trigger system. The L1 was essentially as today; the HLT consisted of two separate systems known as the L2 trigger and the Event Filter (EF). This was changed to the simpler system used today during the shutdown between Run1 and Run2.

929 **High-Level Trigger**

930 The HLT performs the next step, taking the incoming data rate from the L1 trigger  
931 of  $\sim 75$  kHz down to the  $\sim 1$  kHz that can be written to tape. The HLT really  
932 performs much like a simplified offline reconstruction, using many common quality  
933 and analysis cuts to eliminate uninteresting events. This is done by using computing  
934 farms located close to the detector, which process events in parallel. Individually, each  
935 event which enters the computing farms takes about 4 seconds to reconstruct; the  
936 HLT reconstruction time also has a long tail, which necessitates careful monitoring  
937 of the HLT to ensure smooth operation.

938 HLT triggers are targetted to a particular physics process, such as a  $E_T^{\text{miss}}$  trigger,  
939 single muon trigger, or multijet trigger. The collection of all triggers is known as  
940 the trigger *menu*. Since many low-energy particles are produced in collisions, it is  
941 necessary to set a *trigger threshold* on the object of interest; this is really just a fancy  
942 naming for a trigger  $p_T$  cut. Due to the changing luminosity conditions of the LHC,  
943 these thresholds change constantly, mostly by increasing thresholds with increasing  
944 instantaneous luminosity. This allows an approximately constant number of events to be  
945 written for further analysis. Triggers which have rates higher than those designated  
946 by the menu are *prescaled*. This means writing only some fraction of the triggered  
947 events. Of course, for physics analyses, one wishes to investigate all data events  
948 passing some set of analysis cuts, so often one uses the “lowest threshold unprescaled  
949 trigger”. *Turn-on curves* allow one to select the needed offline analysis cut to ensure  
950 the trigger is fully efficient. An example turn-on curve for the  $E_T^{\text{miss}}$  triggers used in  
951 the signal region of this analysis is shown in ??.

952 The full set of the lowest threshold unprescaled triggers considered here can be  
953 found in Table 5.1. These are the lowest unprescaled triggers associated to the SUSY  
954 signal models and Standard Model backgrounds considered in this thesis. More  
955 information can be found in [89].

Physics Object	Trigger	$p_T$ (GeV)	Threshold	Level-1 Seed	Additional Requirements	Approximate Rate (Hz)
<b>2015 Data</b>						
$E_T^{\text{miss}}$	HLT_xe70	70	L1_XE50	-	60	
Muon	HLT_mu24_iloose_L1MU15	50	L1_MU15	isolated, loose	130	
Muon	HLT_mu50	50	L1_MU15	-	30	
Electron	HLT_e24_1hmedium_ll2base_L1EM20VH		L1_EM20VH	medium OR isolated, loose	140	
Electron	HLT_e60_1hmedium	60	L1_EM20VH	medium	10	
Electron	HLT_e120_1hloose	120	L1_EM20VH	loose	<10	
Photon	HLT_g120_loose	120	L1_EM20VH	loose	20	
<b>2016 Data</b>						
$E_T^{\text{miss}}$	HLT_xe100_mht_L1XE5000		L1_XE50	-	180	
Muon	HLT_mu24_ivarmedium4	50	L1_MU20	medium	120	
Muon	HLT_mu50	50	L1_MU20	-	40	
Electron	HLT_e24_1htight_noD1ivarloose		L1_EM22VHI	tight with no $d_0$ or loose	110	
Electron	HLT_e60_1hmedium_nd60		L1_EM22VHI	medium with no $d_0$	10	
Electron	HLT_e140_1hloose_noD0		L1_EM22VHI	loose with no $d_0$	<10	
Photon	HLT_g140_loose	140	L1_EM22VHI	loose	20	

Table 5.1: High-Level Triggers used in this thesis. Descriptions of loose, medium, tight, and isolated can be found in [89]. The  $d_0$  cut refers to a quality cut on the vertex position; this was removed from many triggers in 2016 to increase sensitivity to displaced vertex signals. For most triggers, the increased thresholds in 2016 compared to 2016 were designed to keep the rate approximately equal. The exception is the  $E_T^{\text{miss}}$  triggers; see 5.5.

956 **Razor Triggers**

957 For the analysis presented in this thesis, the *razor triggers* were developed. These are  
958 topological triggers, combining both jet and  $E_T^{\text{miss}}$  information to select interesting  
959 events. In particular, they use the razor variable  $M_{\Delta}^R$  which will be described in  
960 Chapter ??.

961 Based on 2015 run conditions, these triggers would have allowed the use of a lower  
962 offline  $E_T^{\text{miss}}$  cut with a similar rate to the nominal  $E_T^{\text{miss}}$  triggers. This can be seen  
963 in the turn-on curves shown in Figure 5.15. The razor triggers are fully efficient at  
964 nearly 100 GeV lower than the corresponding  $E_T^{\text{miss}}$  triggers in  $M_{\Delta}^R$ .

965 There was a quite big change in the 2016 menu, which increased the rate given to  
966  $E_T^{\text{miss}}$  triggers drastically. This can be seen in the difference in rate shown between  
967  $E_T^{\text{miss}}$  triggers in 2015 and 2016 in Table 5.1. This allowed the  $E_T^{\text{miss}}$  triggers to  
968 maintain a lower threshold throughout the dataset used in this thesis.

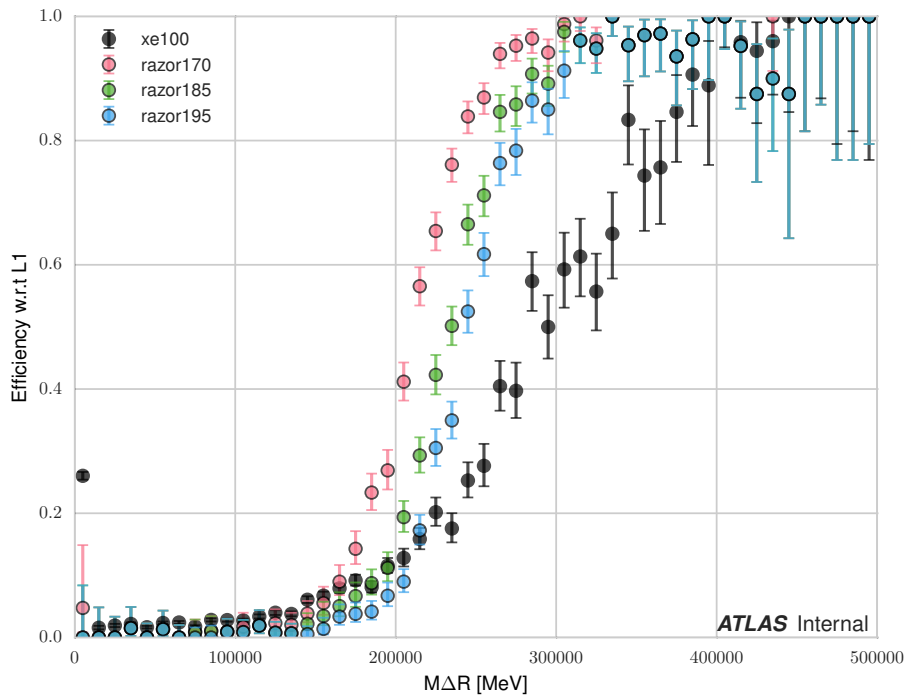
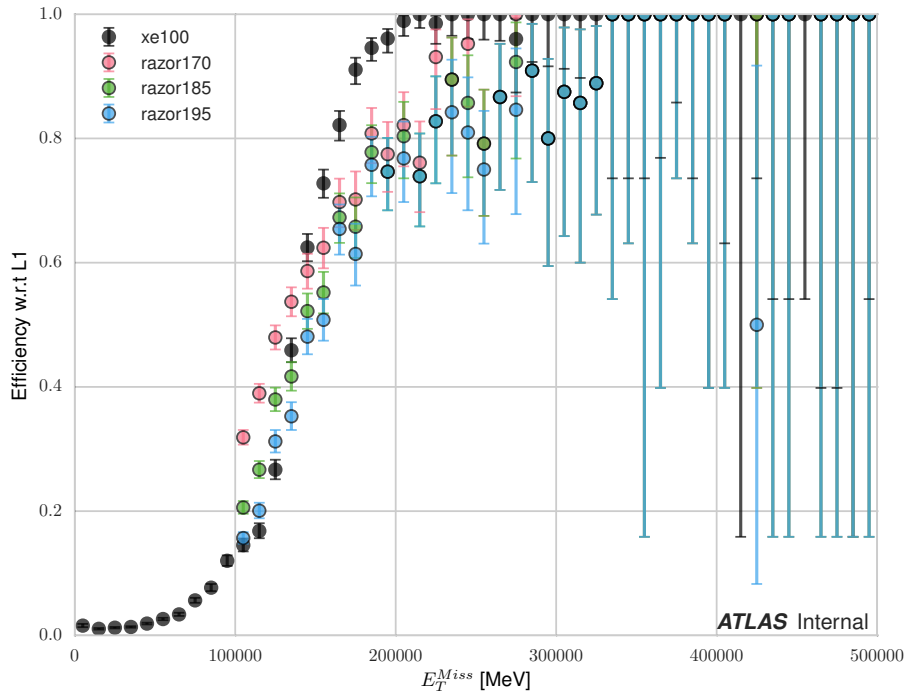


Figure 5.15: Turn-on curves for the razor triggers and nominal  $E_T^{\text{miss}}$  trigger. The razor triggers show a much sharper turn-on in  $M_D^R$  relative to the  $E_T^{\text{miss}}$  trigger. The converse is true for the  $E_T^{\text{miss}}$  triggers.



## Object Reconstruction

971 This chapter describes the reconstruction algorithms used within ATLAS. We will  
972 make the distinction between the “primitive” objects which are reconstructed from  
973 the detector signals from the “composite” physics objects we use in measurements  
974 and searches for new physics.

### 975 6.1 Primitive Object Reconstruction

976 The primitive objects reconstructed by ATLAS are *tracks* and (calorimeter) *clusters*.  
977 These are reconstructed directly from tracking hits and calorimeter energy deposits  
978 into cells. Tracks can be further divided into inner detector and muon spectrom-  
979 eter tracks. Calorimeter clusters can be divided into sliding-window clusters and  
980 topological clusters (topoclusters).

#### 981 Inner Detector Tracks

982 Inner detector tracks are reconstructed from hits in the inner detector [90, 91] These  
983 hits indicate that a charged particle has passed through the detector material. Due  
984 to the 2 T solenoid in the inner detector, the hits associated with any individual  
985 particle will be curved. The amount of curvature determines the momentum of the  
986 particle. In any given event, there are upwards of  $10^4$  hits, making it impossible to do  
987 any sort of combinatorics to reconstruct tracks. There are two algorithms used by  
988 ATLAS track reconstruction, known as *inside-out* and *outside-in*.

989       ATLAS first employs the inside-out algorithm. One assumes the track begins  
990 at the interaction point. Moving out from the interaction point, one creates track  
991 seeds. Track seeds are proto-tracks constructed from three hits. These hits can be  
992 distributed as three pixel hits, two pixel hits and one SCT hit, or three SCT hits.  
993 One extrapolates the track and uses a combinatorial Kalman filter[90], which adds  
994 the rest of the pixel and SCT hits to the seeds. This is done seed by seed, so it  
995 avoids the combinatorial complexity involved with checking all hits with all seeds.  
996 At this point, the algorithm applies an additional filter to avoid ambiguities from  
997 nearby tracks. The TRT hits are added to the seeds using the same method. After  
998 this procedure, all hits are associated to a track.

999       The next step is to figure out the correct kinematics of the track. This is  
1000 done by applying a fitting algorithm which outputs the best-fit track parameters  
1001 by minimizing the track distance from hits, weighted by each hit's resolution. These  
1002 parameters are  $(d_0, z_0, \eta, \phi, q/p)$  where  $d_0$  ( $z_0$ ) is the transverse (longitudinal) impact  
1003 parameter and  $q/p$  is the charge over the track momenta. This set of parameters  
1004 uniquely defines the measurement of the trajectory of the charged particle associated  
1005 to the track. An illustration of a track with these parameters is shown in Fig.6.1.

1006       The other track reconstruction algorithm is the outside-in algorithm. As the  
1007 name implies, we start from the outside of the inner detector, in the TRT, and  
1008 extend the tracks in toward the interaction point. One begins by seeding from  
1009 TRT hits, and extending the track back towards the center of the detector. The  
1010 same fitting procedure is used as in the inside-out algorithm to find the optimal  
1011 track parameters. This algorithm is particularly important for finding tracks which  
1012 originate from interactions with the detector material, especially the SCT. For tracks  
1013 from primary vertices, this often finds the same tracks as the inside-out algorithm,  
1014 providing an important check on the consistency of the tracking procedure.

1015       In the high luminosity environment of the LHC, even the tracks reconstructed

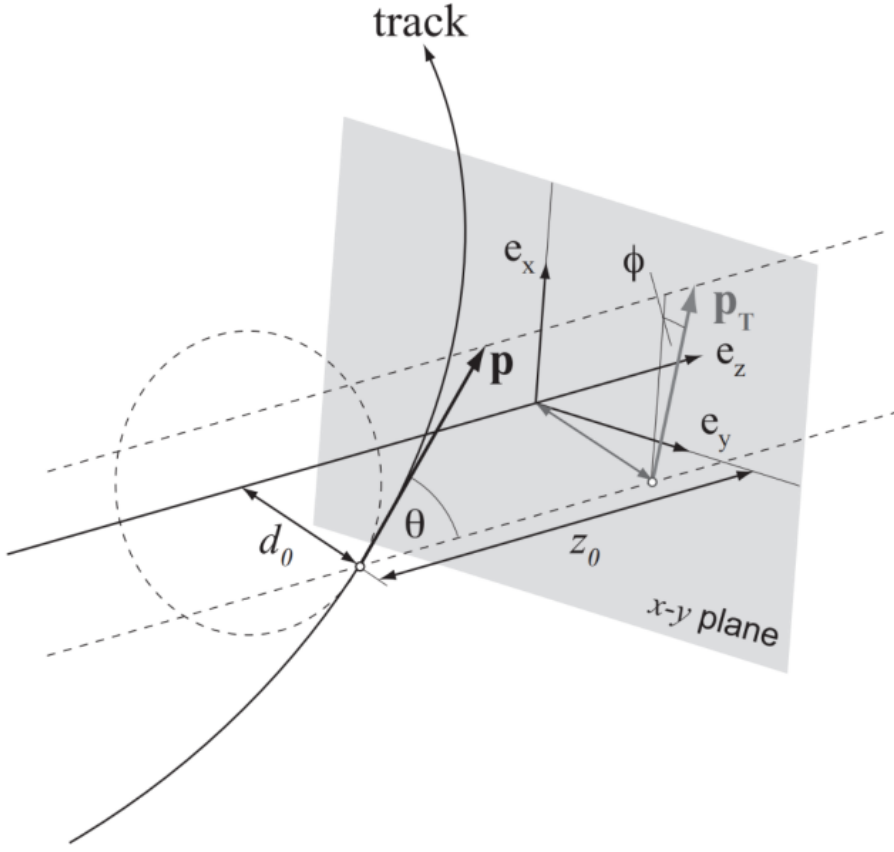


Figure 6.1: The parameters associated to a track.

from precision detectors such as those of ATLAS inner detector can sometimes lead to fake tracks from simple combinatoric chance. Several quality checks are imposed after track fitting which reduce this background. Seven silicon (pixel + SCT) hits are required for all tracks. No more than two *holes* are allowed in the pixel detector. Holes are expected measurements from the track that are missing in the pixel detector. Finally, tracks with poor fit quality, as measured by  $\chi^2/ndf$ , are also rejected. Due to the high quality of the silicon measurements in the pixel detector and SCT, these requirements give good track reconstruction efficiency, as seen in Fig.6.2 for simulated events[92].



(a) Track reconstruction as a function of  $p_T$ . (b) Track reconstruction as a function of  $\eta$ .

Figure 6.2: Track reconstruction efficiency as a function of track  $p_T$  and  $\eta$ . The efficiency is defined as the number of reconstructed tracks divided by the number of generate charged particles.

## 1025 Sliding-window clusters

1026 The sliding-window algorithm is a way to combine calorimeter cells into composite  
 1027 objects (clusters) to be used as inputs for other algorithms[93]. Sliding-window  
 1028 clusters are the primary inputs to electron and photon reconstruction, as described  
 1029 below. The electromagnetic calorimeter has high granularity, with a cell size of  
 1030  $(\eta, \phi) = (.025, .025)$  in the coarsest second layer throughout most of the calorimeter.  
 1031 The “window” consists of 3 by 5 cells in the  $(\eta, \phi)$  space. All layers are added on  
 1032 this same 2D space. One translates this window over the space and seeds a cluster  
 1033 whenever the energy sum of the cells is maximized. If the seed energy is greater  
 1034 than 2.5 GeV, this seed is called a sliding-window cluster. This choice was motivated  
 1035 to optimize the reconstruction efficiency of proto-electrons and proto-photons while  
 1036 rejecting fakes from electronic noise and additional particles from pileup vertices.

## 1037 Topological clusters

1038 Topoclusters are the output of the algorithm used within ATLAS to combine  
1039 hadronic and electromagnetic calorimeter cells in a way which extracts signal from  
1040 a background of significant electronic noise[94]. They are the primary input to the  
1041 algorithms which reconstruct jets.

1042 Topological clusters are reconstructed from calorimeter cells in the following way.  
1043 First, one maps all cells onto a single  $\eta - \phi$  plane so one can speak of *neighboring*  
1044 cells. Two cells are considered neighboring if they are in the same layer and directly  
1045 adjacent, or if they are in adjacent layers and overlap in  $\eta - \phi$  space. The *significance*  
1046  $\xi_{\text{cell}}$  of a cell during a given event is

$$\xi_{\text{cell}} = \frac{E_{\text{cell}}}{\sigma_{\text{noise},\text{cell}}} \quad (6.1)$$

1047 where  $\sigma_{\text{noise},\text{cell}}$  is measured for each cell in ATLAS and  $E_{\text{cell}}$  measures the current  
1048 energy level of the cell. One thinks of this as the measurement of the energy *over*  
1049 *threshold* for the cell.

1050 Topocluster *seeds* are defined as calorimeter cells which have a significance  $\xi_{\text{cell}} >$   
1051 4. These are the inputs to the algorithm. One iteratively tests all cells adjacent  
1052 to these seeds for  $\xi_{\text{cell}} > 2$ . Each cells passing this selection is then added to the  
1053 topocluster, and the procedure is repeated. When the algorithm reaches the point  
1054 where there are no additional adjacent cells with  $\xi_{\text{cell}} > 2$ , every positive-energy cell  
1055 adjacent to the current proto-cluster is added. The collection of summed cells is a  
1056 topocluster. An example of this procedure for a simulation dijet event is shown in  
1057 Fig.6.3.

1058 There are two calibrations used for clusters[95]. These are known as the  
1059 electromagnetic (EM) scale and the local cluster weighting (LCW) scale. The EM  
1060 scale is the energy read directly out of the calorimeters as described. This scale  
1061 is appropriate for electromagnetic processes. The LCW scale applies additional



Figure 6.3: Example of topoclustering on a simulated dijet event.

1062 scaling to the clusters based on the shower development. The cluster energy can be  
1063 corrected for calorimeter non-compensation and the differences in the hadronic and  
1064 electromagnetic calorimeters' responses. This scale provides additional corrections  
1065 that improve the accuracy of hadronic energy measurements. This thesis only uses  
1066 the EM scale corrections. LCW scaling requires additional measurements that only  
1067 became available with additional data. Due to the jet calibration procedure that  
1068 we will describe below, it is also a relatively complicated procedure to rederive the  
1069 “correct” jet energy.

## 1070 Muon Spectrometer Tracks

1071 Muon spectrometer tracks are fit using the same algorithms as the ID tracks, but  
1072 different subdetectors. The tracks are seeded by hits in the MDTs or CSCs. After  
1073 seeding in the MDTs and CSCs, the hits from all subsystems are refit as the final  
1074 MS track. These tracks are used as inputs to the muon reconstruction, as we will see  
1075 below.

## 1076 6.2 Physics Object Reconstruction and Quality

### 1077 Identification

1078 There are essentially six objects used in ATLAS searches for new physics: electrons,  
1079 photons, muons,  $\tau$ -jets, jets, and  $E_T^{\text{miss}}$ . The reconstruction of these objects is  
1080 described here. In this thesis,  $\tau$  lepton jets are not treated differently from other  
1081 hadronic jets, and we will not consider their reconstruction algorithms. A very  
1082 convenient summary plot is shown in Fig.6.4.

1083 One often wishes to understand “how certain” we are that a particular object  
1084 is truly the underlying physics object. In ATLAS, we often generically consider, in



Figure 6.4: The interactions of particles with the ATLAS detector. Solid lines indicate the particle is interacting with the detector, while dashed lines are shown where the particle does not interact.

1085 order, *very loose*, *loose*, *medium*, and *tight* objects<sup>1</sup>. These are ordered in terms of  
 1086 decreasing object efficiency, or equivalently, decreasing numbers of fake objects. We  
 1087 will also describe briefly the classification of objects into these categories.

1088 In this thesis, since we present a search for new physics in a zero lepton final state,  
 1089 we will provide additional details about jet and  $E_T^{\text{miss}}$  reconstruction.

---

<sup>1</sup> These are not all used for all objects, but it's conceptually useful to think of these different categories.

1090 **Electrons and Photons**

1091 **Reconstruction**

1092 The reconstruction of electrons and photons (often for brevity called “electromagnetic  
1093 objects”) is very similar [93, 96, 97]. This is because the reconstruction begins with  
1094 the energy deposit in the calorimeter in the form of an electromagnetic shower. For  
1095 any incoming  $e/\gamma$ , this induces many more electrons and photons in the shower. The  
1096 measurement in the calorimeter is similar for these two objects.

1097 One begins the reconstruction of electromagnetic objects from the sliding-window  
1098 clusters reconstructed from the EM calorimeter. These  $E > 2.5$  GeV clusters the  
1099 the primary seed for electrons and photons. One then looks for all ID tracks within  
1100  $\Delta R < 0.3$ , where  $\Delta R = \sqrt{\Delta\eta^2 + \Delta\phi^2}$ . We “match” the track and cluster if they are  
1101 within  $\Delta\phi < 0.2$  in the direction of track curvature, or  $\Delta\phi < 0.05$  in the direction  
1102 opposite the track curvature. Those track-cluster seeds with tracks pointing to the  
1103 primary vertex are reconstructed as electrons.

1104 For photons, we have two options to consider, known as *converted* and *unconverted*  
1105 photons. Due to the high energy of the LHC collisions, typical photons have energy  
1106  $>\sim 1$  GeV. At this scale, photons interact almost exclusively via pair-production in  
1107 the presence of the detector material, as shown in Fig.6.5 [56]. If the track-cluster seed  
1108 has a track which does not point at the primary vertex, we reconstruct this object as a  
1109 converted photon. This happens since the photon travels a distance before decay into  
1110 two electrons, and see the tracks coming from this secondary vertex. Those clusters  
1111 which do not have any associated tracks are then reconstruced as an unconverted  
1112 photon.

1113 The final step in electromagnetic object reconstruction is the final energy value  
1114 assigned to these objects. This process is different between electrons and photons due  
1115 to their differing signatures in the EM calorimeter. In the barrel, electrons energies

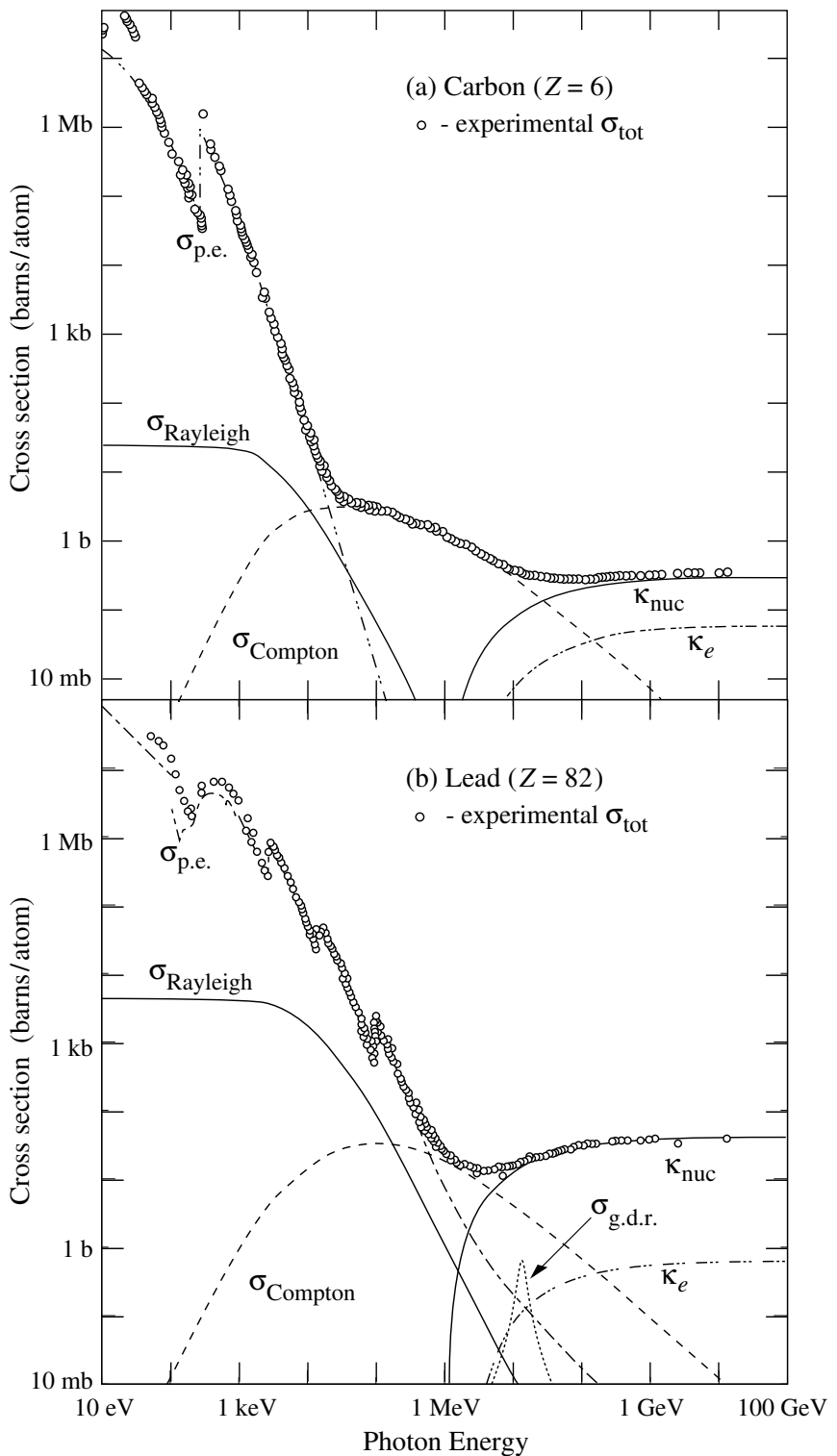


Figure 6.5: Photon total cross sections as a function of energy in carbon and lead, showing the contributions of different processes[56].

1116 are assigned as the sum of the 3 clusters in  $\eta$  and 7 clusters in  $\phi$  to account for the  
1117 electron curving in the  $\phi$  direction. Barrel photons are assigned the energy sum of  
1118 (3, 5) clusters in  $(\eta, \phi)$  space. In the endcap, the effect of the magnetic field on the  
1119 electrons is smaller, and there is a coarser granularity. Both objects sum the (5, 5)  
1120 clusters for their final energy value.

## 1121 Quality Identification

1122 Electrons have a number of important backgrounds which can give fakes. Fake  
1123 electrons come primarily from secondary vertices in hadron decays or misidentified  
1124 hadronic jets. To reduce these backgrounds, quality requirements are imposed on  
1125 electron candidates. Loose electrons have requirements imposed on the shower  
1126 shapes in the electromagnetic calorimeter and on the quality of the associated ID  
1127 track. There is also a requirement that there is a small energy deposition in the  
1128 hadronic calorimeter behind the electron, to avoid jets being misidentified as electrons  
1129 (low hadronic leakage). Medium and tight electrons have increasingly stronger  
1130 requirements on these variables, and additional requirements on the isolation (as  
1131 measured by  $\Delta R$ ) and matching of the ID track momentum and the calorimeter  
1132 energy deposit.

1133 Photons are relatively straightforward to measure, since there are few background  
1134 processes[98]. The primary one is pion decays to two photons, which can cause a jet  
1135 to be misidentified as photon. Loose photons have requirements on the shower shape  
1136 and hadronic leakage. Tight photons have tighter shower shape cuts, especially on  
1137 the high granularity first layer of the EM calorimeter. The efficiency for unconverted  
1138 tight photons as a function of  $p_T$  is shown in

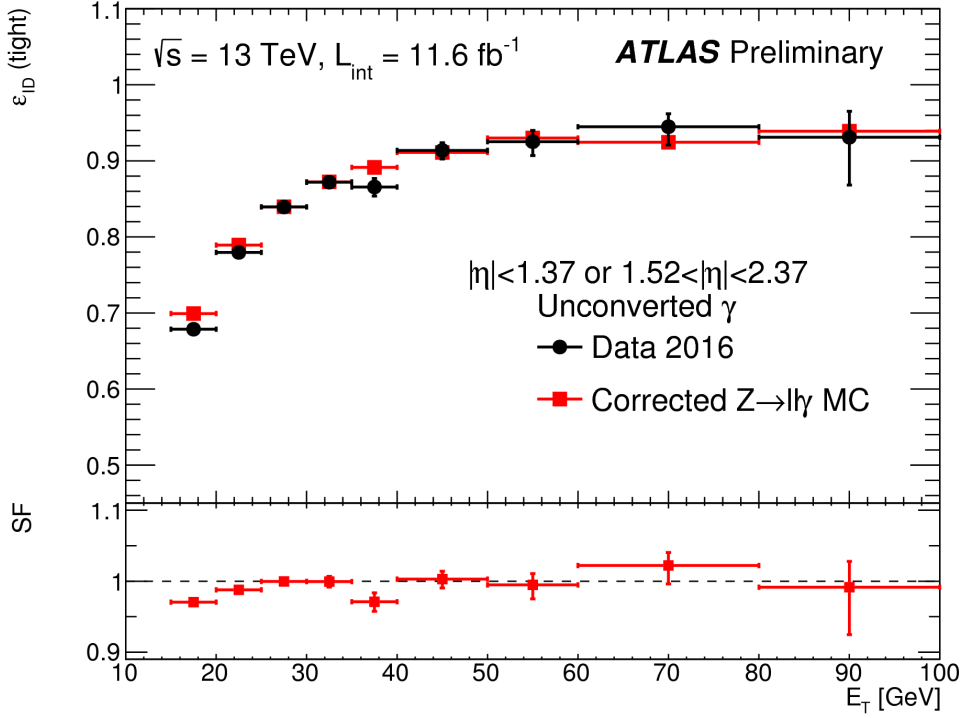


Figure 6.6: Unconverted photon efficiency as measured in [98].

## 1139 Muons

### 1140 Reconstruction

1141 Muons are reconstructed using measurements from all levels of the ATLAS detec-  
 1142 tor[99]. They leave a ID track, a small, characteristic deposition in the EM calorime-  
 1143 ter, and then a track in the muon spectrometer. The primary reconstruction technique  
 1144 produces a so-called *combined* muon. “Combined” means using a combination of the  
 1145 ID and MS tracks to produce the final reconstructed muon kinematics. This is done  
 1146 by refitting the hits associated to both tracks, and using this refit track for the muon  
 1147 kinematics. This process produces the best measured muons, although several other  
 1148 worse algorithms are used when the full detector information is missing. An example  
 1149 is in the region  $2.5 < |\eta| < 2.7$  outside the ID acceptance, where MS tracks are used  
 1150 without the corresponding ID tracks.

1151 **Quality Identification**

Several additional criteria are used to assure muon measurements are free of significant background contributions, especially from pion and kaon decays to muons. Muons produced via these decay processes are often characterized by a “kink”. Candidate muons with a poor fit quality, characterized by  $\chi^2/\text{n.d.f.}$ , are thus rejected. Additionally, the absolute difference in momentum measurements between the ID and MS provide another handle, since the other decay products from hadron decays carry away some amount of the initial hadron momentum. This is measured by

$$\rho' = \frac{|p_T^{\text{ID}} - p_T^{\text{MS}}|}{p_T^{\text{Combined}}}. \quad (6.2)$$

Additionally, there is a requirement on the  $q/p$  significance, defined as

$$S_{q/p} = \frac{|(q/p)^{\text{ID}} - (q/p)^{\text{MS}}|}{\sqrt{\sigma_{\text{ID}}^2 + \sigma_{\text{MS}}^2}}. \quad (6.3)$$

1152 The  $\sigma_{\text{ID,MS}}$  in the denominator of Eq.6.3 are the uncertainties on the corresponding  
1153 quantity from the numerator. Finally, cuts are placed on the number of hits in the  
1154 various detector elements.

1155 Subsequently tighter cuts on these variables allow one to define the different muon  
1156 identification criteria. Loose muons have the highest reconstruction efficiency, but  
1157 the highest number of fake muons, since there are no requirements on the number  
1158 of subdetector hits and the loosest requirements on the suite of quality variables.  
1159 Medium muons consist of Loose muons with tighter cuts on the quality variables.  
1160 They also require more than three MDT hits in at least two MDT layers. These are  
1161 the default used by ATLAS analyses. Tight muons have stronger cuts than those of  
1162 the medium selection, and reducing the reconstruction efficiency. The reconstruction  
1163 efficiency as a function of  $p_T$  can be seen for Medium muons in Fig.6.7.

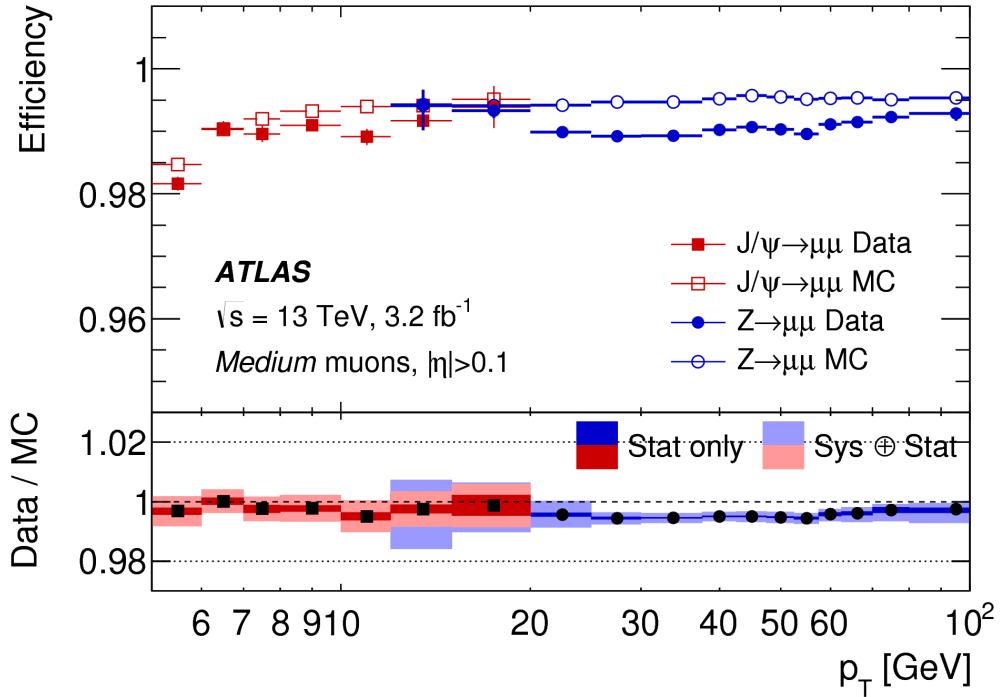


Figure 6.7: Medium muon efficiency as measured in [99].

## 1164 Jets

1165 Jets are composite objects corresponding to many physical particles [56, 100, 101]  
 1166 This is a striking difference from the earlier particles. Fortunately, we normally (and  
 1167 in this thesis) care about the original particle produced in primary collision. In the  
 1168 SM, this corresponds to quarks and gluons. Due to the hadronization process, free  
 1169 quarks and gluons spontaneously hadronize and produce a hadronic shower, which  
 1170 we call a jet. These showers can be measured by the EM and hadronic calorimeters,  
 1171 and the charged portions can be measured in the ID. The first question is how to  
 1172 combine these measurements into a composite object representing the underlying  
 1173 physical parton. This is done via jet algorithms.

1174 **Jet Algorithms**

1175 It might seem straightforward to combine the underlying physical particles into a  
1176 jet. There are three important characteristics required for any jet reconstruction  
1177 algorithm to be used by ATLAS.

- 1178     • Collinear safety - if any particle with four-vector  $p$  is replaced by two particles  
1179       of  $p_1, p_2$  with  $p = p_1 + p_2$ , the subsequent jet should not change  
  
1180     • Radiative (infrared) safety - if any particle with four-vector  $p$  radiates a particle  
1181       of energy  $\alpha \rightarrow 0$ , the subsequent jet should not change  
  
1182     • Fast - the jet algorithm should be “fast enough” to be useable by ATLAS  
1183       computing resources

1184 The first two requirements can be seen in terms of requirements on soft gluon emission.  
1185 Since partons emit arbitrarily soft gluons freely, one should expect the algorithms  
1186 to not be affected by this emission. The final requirement is of course a practical  
1187 limitation.

The algorithms in use by ATLAS (and CMS) which satisfies these requirements are collectively known as the  $k_T$ algorithms [102–104]. These algorithms iteratively combine the “closest” objects, defined using the following distance measures :

$$d_{ij} = \min(k_{T,i}^{2p}, k_{T,j}^{2p}) \frac{\Delta_{ij}^2}{R^2} \quad (6.4)$$
$$d_{iB} = k_{Ti}^{2p}$$

1188 In Eq.6.4,  $k_T, i$  is the transverse momentum of  $i$ -th jet *constituent*,  $\Delta_{ij}$  is the angular  
1189 distance between the constituents. Both  $R$  and  $p$  are adjustable parameters:  $R$  is  
1190 known as the (jet) *cone size* and  $p$  regulates the power of the energy versus the  
1191 geometrical scales. The algorithm sequence, for a given set of objects  $i$  with four-  
1192 vector  $k$  :

- 1193     1. Find the minimum distance in the set of all  $d_{ij}$  and  $d_{iB}$ .

1194     2. If the distance is one of the  $d_{ij}$ , combine the input pair of object  $i, j$  and return  
1195         to (1). If the distance is one of the  $d_{iB}$ , remove the object from the list, call it  
1196         a jet, and return to (1).

1197 This process ends when all objects  $i$  have been added to a jet.

1198 Any choice of  $(p, R)$  has the requirements of collinear and radiative safety. In  
1199 essence, the choice is then to optimize based on speed and the potential for new  
1200 physics discoveries. In ATLAS, we make the choice of  $p = -1$  which is also known  
1201 as the *anti- $k_T$*  algorithm. The choice of  $R = 0.4$  is used for the distance parameter of  
1202 the jets.

1203 The primary “nice” quality of this algorithm can be seen with the following  
1204 example. Consider three inputs to an anti- $k_T$  algorithm, all with  $\eta = 0$  :

- 1205     • Object 1 :  $(p_T, \phi) = (30 \text{ GeV}, 0)$
- 1206     • Object 2 :  $(p_T, \phi) = (20 \text{ GeV}, -0.2)$
- 1207     • Object 3 :  $(p_T, \phi) = (10 \text{ GeV}, 0.2)$
- 1208     • Object 4 :  $(p_T, \phi) = (1 \text{ GeV}, 0.5)$

1209 . In the case shown, it seems natural to first combine the “bigger” objects 1 and 2.  
1210 These then pick up the extra small object 3, and object 4 is not included in the jet.  
1211 This is exactly what is done by the anti- $k_T$  algorithm. The (normal)  $k_T$  algorithm with  
1212  $p = 1$  instead combines the smallest objects, 3 and 4, first. Object 1 and 2 combine  
1213 to form their own jet, instead of these jets picking up object 3. This behavior is not  
1214 ideal due to the effects of pileup, as we will see in the next section.

## 1215 Jet Reconstruction

1216 In ATLAS, jets are reconstructed using multiple different objects as inputs, including  
1217 tracks, “truth” objects, calorimeter clusters, and *particle flow objects* (PFOs). For

1218 physics analyses, ATLAS primarily uses jets reconstructed from calorimeter clusters,  
1219 but we will describe the others here, as they are often used for derivations of  
1220 systematic uncertainties or future prospects.

1221 Calorimeter jets are reconstructed using topoclusters using the anti- $k_T$  algorithm  
1222 with  $R = 0.4$ . The jet reconstruction algorithm is run on the collection of all  
1223 topoclusters reconstructed as in Sec.6.1. Both EM and LCW scale clusters are used  
1224 in the ATLAS reconstruction software and produce two sets of jets for analysis. As  
1225 stated above, this thesis presents an analysis using jets reconstructed using EM scale  
1226 clusters, which we refer to these as *EM jets*.

1227 Tracks can be used as inputs to jet reconstruction algorithms. Jets reconstructed  
1228 from tracks are known as *track jets*. Since the ID tracks do not measure neutral  
1229 objects, these jets measure an incorrect energy. However, these are still useful for  
1230 checks and derivations of systematic uncertainties.

1231 *Truth* jets are reconstructed from *truth* particles. In this case, truth is jargon for  
1232 simulation. In simulation, the actual simulated particles are available and used as  
1233 inputs to the jet reconstruction algorithms. Similarly to track jets, these are not useful  
1234 in and of themselves. Instead, truth jets are used for comparisons and derivations of  
1235 systematic uncertainties.

1236 The last object used as inputs to jet reconstruction algorithms are *particle flow*  
1237 *objects* (PFOs). These are used extensively as the primary input to jet particle  
1238 reconstruction algorithms by the CMS collaboration[105]. Particle flow objects are  
1239 reconstructed by associating tracks and clusters through a combination of angular  
1240 distance measures and detector response measurements to create a composite object  
1241 which contains information from both the ID and the calorimeters. For calorimeter  
1242 clusters which do not have any associated ID track, the cluster is simply the PFO.  
1243 The natural association between tracks and clusters provides easy pileup subtraction  
1244 since tracks are easily associated to the primary vertex. This technique is generally

1245 used in CMS, and ATLAS has been slow to adopt the same. As pileup has increased,  
1246 the utility of using PFOs as inputs to jet reconstruction has increased as well.

1247 **Jet Calibration**

1248 Jets as described in the last section are still *uncalibrated*. Even correcting the cluster  
1249 energies using the LCW does not fully correct the jet energy, due to particles losing  
1250 energy in the calorimeters. The solution to this is the *jet energy scale* (JES). The  
1251 JES is a series of calibrations which on average restore the correct truth jet energy  
1252 for a given reconstructed jet. These steps are shown in Fig.6.8 and described here.

1253 The first step is the origin correction. This adjusts the jet to point at the  
1254 primary vertex. Next, is the jet-area based pileup correction. This step subtracts  
1255 the “average” pileup as measured by the energy density  $\rho$  outside of the jets and  
1256 assumes this is a good approximation for the pileup inside the jet. One then removes  
1257 energy  $\Delta E = \rho \times A_{\text{jet}}$  in this step. The residual pileup correction makes a final offset  
1258 correction by parametrizing the change in jet energy as a function of the number of  
1259 primary vertices  $N_{\text{PV}}$  and the average number of interactions  $\mu$ .

1260 The next step is the most important single correction, known as the AbsoluteEta-  
1261 JES step. Due to the use of non-compensation and sampling calorimeters in ATLAS,  
1262 the measured energy of a jet is a fraction of the true energy of the outgoing parton.  
1263 Additionally, due to the use of different technologies and calorimeters throughout the  
1264 detector, there are directional biases induced by these effects. The correction bins a  
1265 multiplicative factor in  $p_{\text{T}}$  and  $\eta$  which scales the reconstructed jets to corresponding  
1266 truth jet  $p_{\text{T}}$ . This step does not entirely correct the jets, since it is entirely a  
1267 simulation-based approach.

1268 The final steps are known as the global sequential calibration (GSC) and the  
1269 residual in-situ calibration. The GSC uses information about the jet showering shape  
1270 to apply additional corrections based on the expected shape of gluon or quark jets.

1271 The final step is the residual in-situ calibration, which is only applied to data. This  
1272 step uses well-measured objects recoiling off a jet to provide a final correction to the  
1273 jets in data. In the low  $p_T$  region ( $20 \text{ GeV} \sim < p_{T,\text{jet}} \sim < 200 \text{ GeV}$ ),  $Z \rightarrow ll$  events are  
1274 used as a reference object. In the middle  $p_T$  region ( $100 \text{ GeV} \sim < p_{T,\text{jet}} \sim < 600 \text{ GeV}$ ),  
1275 the reference object is a photon, while in the high  $p_T$  region ( $p_{T,\text{jet}} \sim > 200 \text{ GeV}$ ),  
1276 the high  $p_T$  jet is compared to multiple smaller  $p_T$  jets. The reference object is this  
1277 group of multijets. After this final correction, the data and MC scales are identical  
1278 up to the corresponding uncertainties. The combined JES uncertainty as a function  
1279 of  $p_T$  is shown in Fig.6.9.

## 1280 Jet Vertex Tagger

1281 The *jet vertex tagger* (JVT) technique is used to separate pileup jets from those  
1282 associated to the hard primary vertex[106]. The technique for doing so first involves  
1283 *ghost association*[107]. Ghost association runs the anti- $k_T$ jet clustering algorithm on  
1284 a combined collection of the topoclusters and tracks. The tracks *only* momenta are  
1285 set to zero<sup>2</sup>, with only the directional information is included. As discussed above,  
1286 the anti- $k_T$ algorithm is “big to small”; tracks are associated to the “biggest” jet near  
1287 them in  $(\eta, \phi)$ . This method uniquely associates each track to a jet, without changing  
1288 the final jet kinematics.

1289 The JVT technique uses a combination of these track variables to determine the  
1290 likelihood that the jet originated at the primary vertex. For jets which have associated  
1291 tracks from ghost association, this value ranges from 0 (likely pileup jet) to 1 (likely  
1292 hard scatter jet). Jets without associated tracks are assigned  $\text{JVT} = -.1$ . The  
1293 working point of  $\text{JVT} > .59$  is used for jets in this thesis.

---

<sup>2</sup>Well, not exactly zero, since zero momentum tracks wouldn’t have a well-defined  $(\eta, \phi)$  coordinate, but set to a value obeying  $p_{T,\text{track}} << 400 \text{ MeV} = p_{\text{track,min}}$ . This is the minimum momentum for a track to reach the ATLAS inner detector.

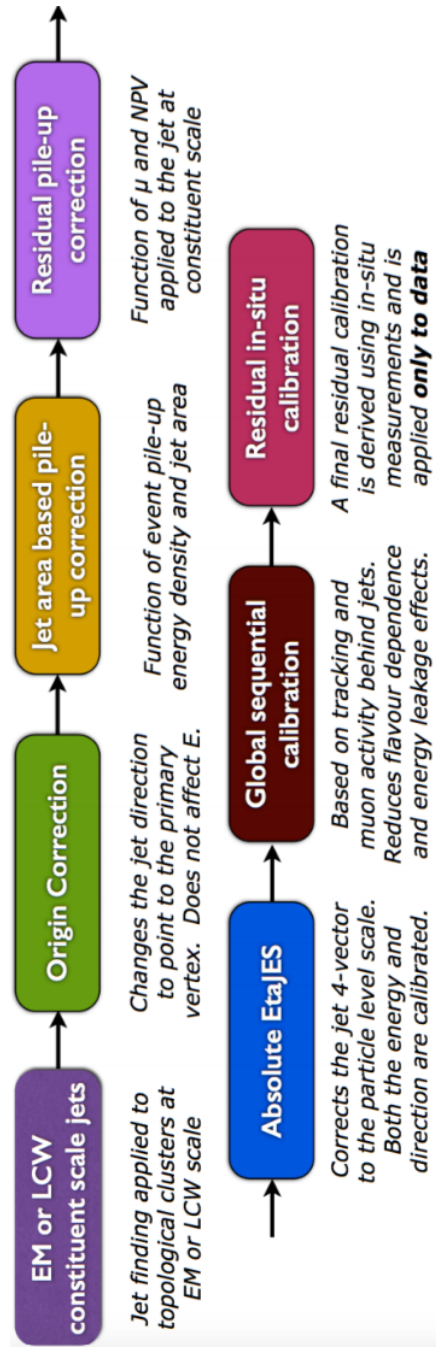


Figure 6.8: The steps used by ATLAS to calibrate jets

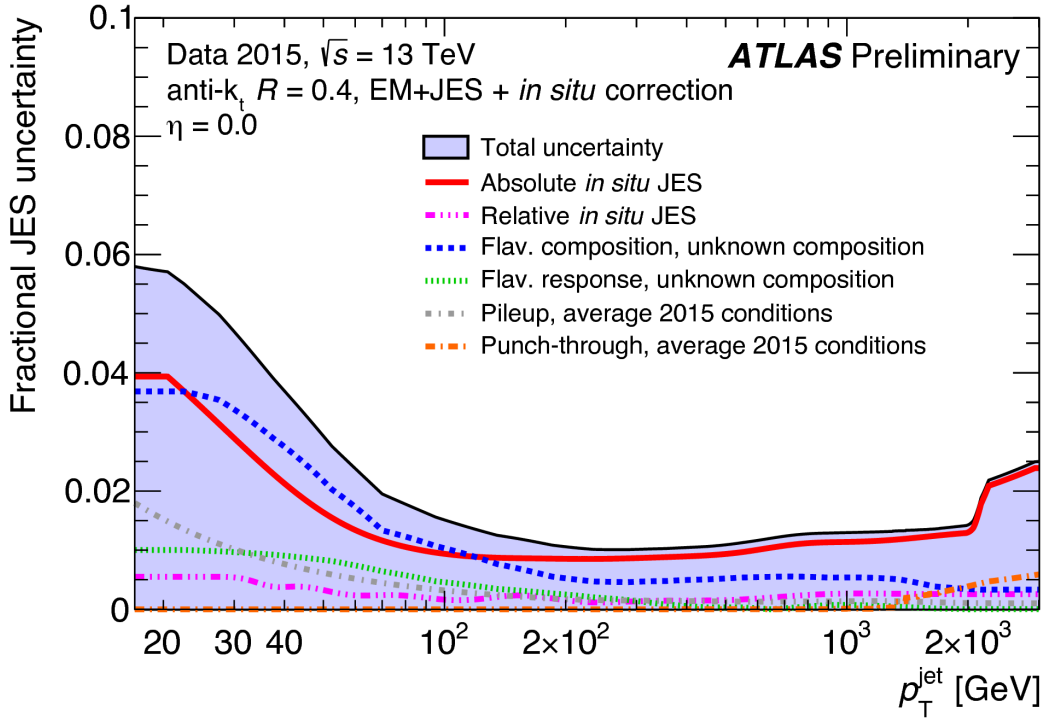


Figure 6.9: Combined jet energy scale uncertainty as a function of  $p_T$  at  $\eta = 0$ .

## 1294 B-jets

1295 Jets originating from bottom quarks (b-jets) are interesting physical phenomena that  
 1296 can be *tagged* by the ATLAS detector[Aad:2015ydr, 108]. B-hadrons, which have  
 1297 a comparatively long lifetime compared to hadrons consisting of lighter quarks, can  
 1298 travel a macroscopic distance inside the ATLAS detector. The high-precision tracking  
 1299 detectors identify the secondary vertices from these decays and the jet matched to  
 1300 that vertex is called a *b-jet*. The “MV2c10” algorithm, based on boosted decision  
 1301 trees, identifies these jets using a combination of variables sensitive to the difference  
 1302 between light-quark and b-quark jets. The efficiency of this tagger is 77%, with a  
 1303 rejection factor of 134 for light-quarks and 6 for charm jets.

## 1304 Missing Transverse Momentum

1305 Missing transverse momentum  $E_T^{\text{miss}}$  [109] is a key observable in searches for new  
1306 physics, especially in SUSY searches[110, 111]. However,  $E_T^{\text{miss}}$  is not a uniquely  
1307 defined object when considered from the detector perspective (as compared to the  
1308 Feynammn diagram), and it is useful to understand the choices that affect the  
1309 performance of this observable in searches for new physics.

### 1310 $E_T^{\text{miss}}$ Definitions

*Hard* objects refers to all physical objects as defined in the previous sections. The  
 $E_T^{\text{miss}}$  reconstruction procedure uses these hard objects and the *soft term* to provide  
a value and direction of the missing transverse momentum. The  $E_{x(y)}^{\text{miss}}$  components  
are calculated as:

$$E_{x(y)}^{\text{miss}} = E_{x(y)}^{\text{miss, } e} + E_{x(y)}^{\text{miss, } \gamma} + E_{x(y)}^{\text{miss, jets}} + E_{x(y)}^{\text{miss, } \mu} + E_{x(y)}^{\text{miss, soft}}, \quad (6.5)$$

1311 where each value  $E_{x(y)}^{\text{miss, } i}$  is the negative vectorial sum of the calibrated objects defined  
1312 in the previous sections.

1313 For purposes of  $E_T^{\text{miss}}$  reconstruction, we must assign an ordering of *overlap*  
1314 *removal*. This is to avoid double counting of the underlying primitive objects (clusters  
1315 and tracks) which are inputs to the reconstruction of the physics objects. We resolve  
1316 this in the following order : electrons, photons , jets and muons. This is motivated  
1317 by the performance of the reconstruction of these objects in the calorimeters.

1318 The soft term  $E_{x(y)}^{\text{miss, soft}}$  contains all of the primitive objects which are not  
1319 associated to any of the reconstructed physics objects. Of course, we need to choose  
1320 which primitive object to use. The primary choices which have been used within  
1321 ATLAS are the *calorimeter-based soft term* (CST) and the *track-based soft term*  
1322 (TST). Based on the soft term choice, we then call  $E_T^{\text{miss}}$  built with a CST (TST)

1323 soft term simply CST (TST)  $E_T^{\text{miss}}$ . An additional option, which will be important  
1324 as pileup continues to increase, particle flow  $E_T^{\text{miss}}$  (PFlow  $E_T^{\text{miss}}$ ).

1325 The CST  $E_T^{\text{miss}}$  was used for much of the early ATLAS data-taking. CST  $E_T^{\text{miss}}$  is  
1326 built from the calibrated hard objects, combined with the calorimeter clusters which  
1327 are *not* assigned to any of those hard objects. In the absence of pileup, it provides the  
1328 best answer for the “true”  $E_T^{\text{miss}}$  in a given event, due to the impressive hermiticity of  
1329 the calorimeters. Unfortunately, the calorimeters do not know “where” from where  
1330 their energy deposition came, and thus CST is susceptible to drastically reduced  
1331 performance as pileup is increased.

1332 TST  $E_T^{\text{miss}}$  is the standard for ATLAS searches as currently performed by ATLAS.  
1333 TST  $E_T^{\text{miss}}$  is built by using the calibrated hard objects and the soft term is built from  
1334 the tracks which are not assigned to any of those hard objects. In particular, due  
1335 to the impressive track-vertex association efficiency, one chooses tracks which only  
1336 come from the primary vertex. This drastically reduces the pileup contributions to  
1337 the  $E_T^{\text{miss}}$  measurement. However, since the ID tracking system is unable to measure  
1338 neutral objects, the TST  $E_T^{\text{miss}}$  is “wrong”. This bias is important to understand for  
1339 many measurements. However, in most searches for new physics, the soft  $E_T^{\text{miss}}$  is  
1340 generally a small fraction of the total  $E_T^{\text{miss}}$ , and thus this bias is not particularly  
1341 hurtful.

1342 PFlow  $E_T^{\text{miss}}$  uses the PFOs described above to build the  $E_T^{\text{miss}}$ . The PFOs which  
1343 are assigned to hard objects are calibrated, and the PFOs which are not assigned  
1344 to any hard object are added to the soft term. In this context, it is convenient to  
1345 distinguish between “charged” and “neutral” PFOs. Charged PFOs can be seen as a  
1346 topocluster which has an associated track, while neutral PFOs do not. This charged  
1347 PFO is essentially a topocluster that we are “sure” comes from the primary vertex.  
1348 The neutral PFOs are in the same status as the original topoclusters. Thus a “full”  
1349 PFlow  $E_T^{\text{miss}}$  should have performance somewhere between TST  $E_T^{\text{miss}}$  and CST  $E_T^{\text{miss}}$ <sup>3</sup>.

1350 A *charged* PFlow  $E_T^{\text{miss}}$  should for sanity be the same as TST.

1351 **Measuring  $E_T^{\text{miss}}$  Performance : event selection**

1352 The question is now straightforward: how do we compare these different algorithms?  
1353 We compare these algorithms in  $Z \rightarrow \ell\ell + \text{jets}$  and  $W \rightarrow \ell\nu + \text{jets}$  events. Due to  
1354 the presence of leptons, these events are well-measured “standard candles”. Here  
1355 we present the results in early 2015 data with  $Z \rightarrow \mu\mu$  and  $W \rightarrow e\nu$  events, as  
1356 shown in [112, 113]. This result was important to assure the integrity of the  $E_T^{\text{miss}}$   
1357 measurements at the higher energy and pileup environment of Run-2.

1358 The  $Z \rightarrow \ell\ell$  selection is used to measure the intrinsic  $E_T^{\text{miss}}$  resolution of the  
1359 detector. The only possible source of neutrinos in these decays is from heavy-flavor  
1360 decays inside of jets, and thus  $Z \rightarrow \ell\ell$  events they have very low  $E_T^{\text{miss}}$ . This provides  
1361 an ideal event topology to understand the modelling of  $E_T^{\text{miss}}$  mismeasurement.  
1362 Candidate  $Z \rightarrow \mu\mu$  events are first required to pass a muon or electron trigger, as  
1363 described in Table 5.1. Offline, the selection of  $Z \rightarrow \mu\mu$  events requires exactly two  
1364 medium muons. The muons are required to have opposite charge and  $p_T > 25 \text{ GeV}$ ,  
1365 and mass of the dimuon system is required to be consistent with the  $Z$  mass  
1366  $|m_{ll} - m_Z| < 25 \text{ GeV}$ .

$W \rightarrow \ell\nu$  events are an important topology to evaluate the  $E_T^{\text{miss}}$  modelling in  
an event with real  $E_T^{\text{miss}}$ . This  $E_T^{\text{miss}}$  is from the neutrino, which is not detected.  
The  $E_T^{\text{miss}}$  in these events has a characteristic distribution with a peak at  $\frac{1}{2}m_W$ . The  
selection of  $W \rightarrow e\nu$  events begins with the selection of exactly one electron of medium  
quality. A selection on TST  $E_T^{\text{miss}} > 25 \text{ GeV}$  drastically reduces the background from  
multijet events where the jet fakes an electron. The transverse mass is used to select

---

<sup>3</sup>Naively, due to approximate isospin symmetry, about 2/3 of the hadrons will be charged and 1/3 will be neutral.

the  $W \rightarrow e\nu$  events :

$$m_T = \sqrt{2p_T^\ell E_T^{\text{miss}}(1 - \cos \Delta\phi)}, \quad (6.6)$$

1367 where  $\Delta\phi$  is the difference in the  $\phi$  between the  $E_T^{\text{miss}}$  and the electron.  $m_T$  is required  
1368 to be greater than 50 GeV.

1369 There are two main ingredients to investigate : the  $E_T^{\text{miss}}$  resolution and the  $E_T^{\text{miss}}$   
1370 scale.

### 1371 Measuring $E_T^{\text{miss}}$ Performance in early 2015 data : metrics

1372 To compare these algorithms we use the  $E_T^{\text{miss}}$  resolution,  $E_T^{\text{miss}}$  scale, and the  
1373 linearity. Representative distributions of TST  $E_x^{\text{miss}}$ ,  $E_y^{\text{miss}}$ , and  $E_T^{\text{miss}}$  from early  
1374 2015 datataking are shown in Fig.6.10.

The  $E_T^{\text{miss}}$  resolution is an important variable due to the fact that the bulk of the distributions associated to  $E_{x(y)}^{\text{miss}}$  are Gaussian distributed [Aad2012]. However, to properly measure the tails of this distribution, especially when considering non-calorimeter based soft terms, it is important to use the root-mean square as the proper measure of the resolution. This is strictly larger than a resolution as measured using a fit to a Gaussian, due to the long tails from i.e. track mismeasurements. The resolution is measured with respect to two separate variables :  $\sum E_T$  and  $N_{\text{PV}}$ .  $\sum E_T$  is an important measure of the “total event activity”. It is defined as

$$\sum E_T = \sum p_T^e + \sum p_T^\gamma + \sum p_T^\tau + \sum p_T^{\text{jets}} + \sum p_T^\mu + \sum p_T^{\text{soft}}. \quad (6.7)$$

1375 The measurement as a function of  $N_{\text{PV}}$  is useful to understand the degradation of  
1376  $E_T^{\text{miss}}$  performance with increasing pileup. Figure 6.11 shows the  $E_T^{\text{miss}}$  resolution in  
1377 the early 2015 data. The degradation of the  $E_T^{\text{miss}}$  performance is shown as a function  
1378 of pileup  $N_{\text{PV}}$  and total event activity  $\sum E_T$ .

Another important performance metric is the  $E_T^{\text{miss}}$  scale, or how “right” we are in our  $E_T^{\text{miss}}$  calculation. This can be off in various directions, as CST  $E_T^{\text{miss}}$  contains

additional particles from pileup, while soft neutral particles<sup>4</sup> are ignored by TST  $E_T^{\text{miss}}$ .

To measure this in data, we again use  $Z \rightarrow \mu\mu$  events, where the  $Z \rightarrow \mu\mu$  system is treated as a well-measured reference object. The component of  $E_T^{\text{miss}}$  which is in the same direction as the reconstructed  $Z \rightarrow \mu\mu$  system is sensitive to potential biases in the detector response. The unit vector  $\mathbf{A}_Z$  of the  $Z$  system is defined as

$$\mathbf{A}_Z = \frac{\vec{p}_T^{\ell^+} + \vec{p}_T^{\ell^-}}{|\vec{p}_T^{\ell^+} + \vec{p}_T^{\ell^-}|}, \quad (6.8)$$

where  $\vec{p}_T^{\ell^+}$  and  $\vec{p}_T^{\ell^-}$  are the transverse momenta of the leptons from the  $Z$  boson decay. The relevant scale metric is then the mean value of the  $\vec{E}_T^{\text{miss}}$  projected onto  $\mathbf{A}_Z$  :  $\langle \vec{E}_T^{\text{miss}} \cdot \mathbf{A}_Z \rangle$ . In Figure 6.12, the scale is shown for the early 2015 dataset. The negative bias, which is maximized at about 5 GeV, is a reflection of two separate effects. The soft neutral particles are missed by the tracking system, and thus ignored in TST  $E_T^{\text{miss}}$ . Missed particles due to the limited ID acceptance can also affect the scale.

For events with real  $E_T^{\text{miss}}$ , one can also look at the *linearity* in simulation. This is defined as

$$\text{linearity} = \left\langle \frac{E_T^{\text{miss}} - E_T^{\text{miss,Truth}}}{E_T^{\text{miss,Truth}}} \right\rangle. \quad (6.9)$$

$E_T^{\text{miss,Truth}}$  refers to “truth” particles as defined before, or the magnitude of the vector sum of all noninteracting particles. The linearity is expected to be zero if the  $E_T^{\text{miss}}$  is reconstructed at the correct scale.

## 1389 Particle Flow Performance

As described above, the resolution, scale, and linearity are the most important metrics to understand the performance of the different  $E_T^{\text{miss}}$  algorithms. In this section, we present comparisons of the different algorithms, including particle flow, in simulation

---

<sup>4</sup>“Soft” here means those particles which are not hard enough to be reconstructed as their own particle, using the reconstruction algorithms above.

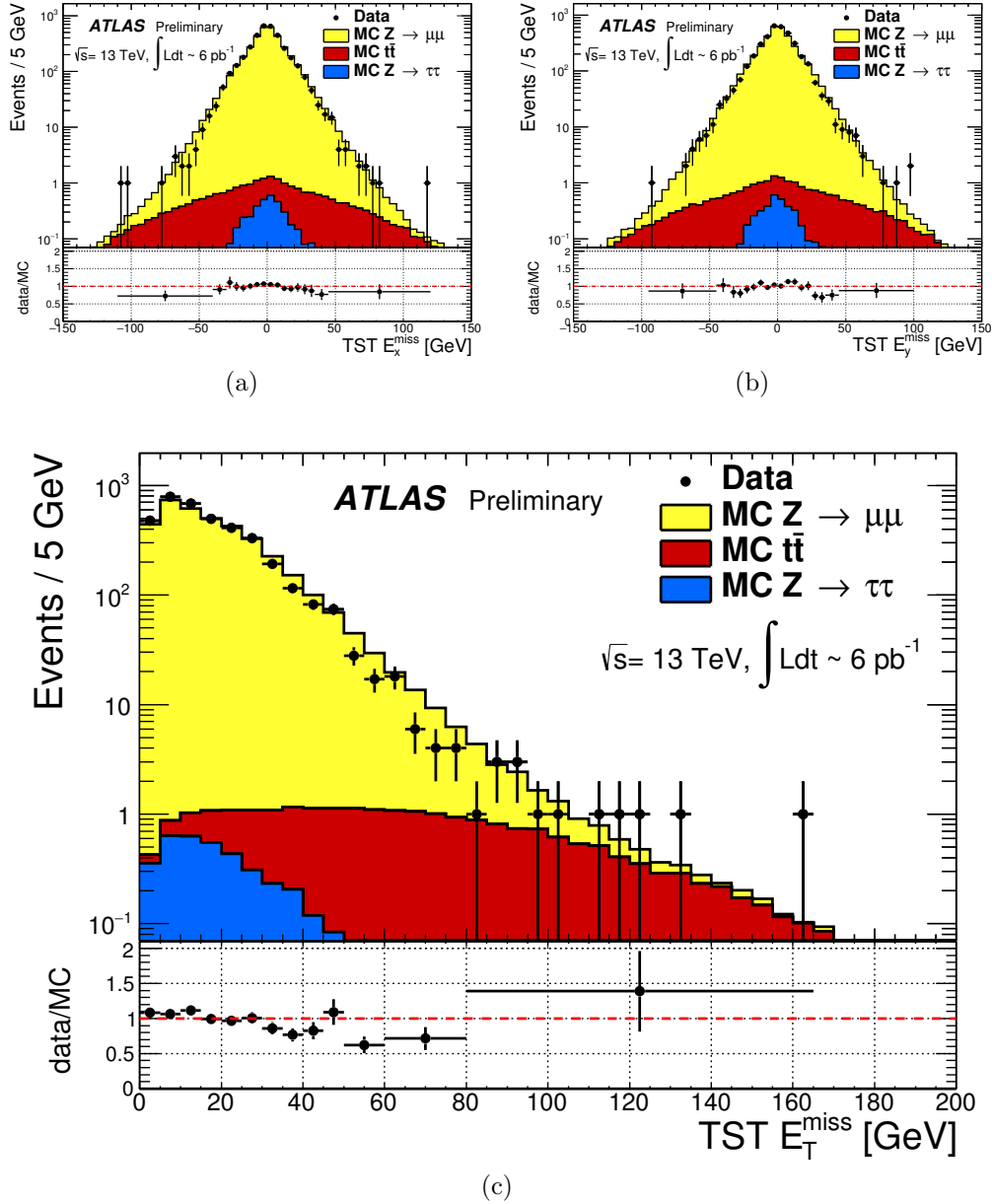


Figure 6.10: TST  $E_{x}^{\text{miss}}$ ,  $E_{y}^{\text{miss}}$ , and  $E_{\text{T}}^{\text{miss}}$  distributions of early  $\sqrt{s} = 13$  TeV data compared with simulation after the  $Z \rightarrow \mu\mu$  selection described in Sec. 6.2. The data sample consists of  $6 \text{ pb}^{-1}$ .

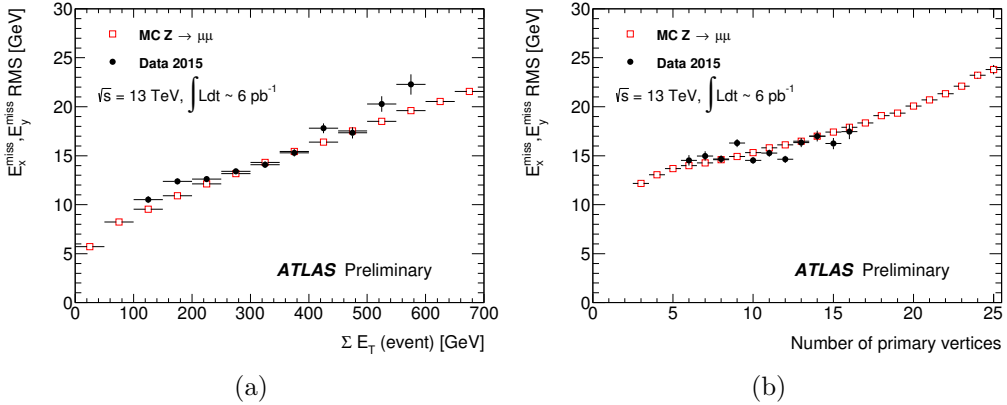


Figure 6.11: Resolution of TST  $E_T^{\text{miss}}$  of early  $\sqrt{s} = 13$  TeV data compared with simulation after the  $Z \rightarrow \mu\mu$  selection described in Sec.6.2. The data sample consists of  $6 \text{ pb}^{-1}$ .

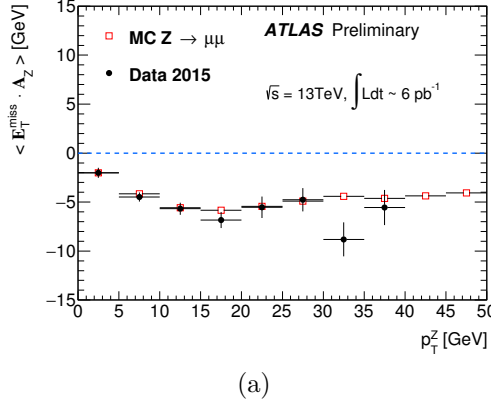


Figure 6.12: Scale of TST  $E_T^{\text{miss}}$  of early  $\sqrt{s} = 13$  TeV data compared with simulation after the  $Z \rightarrow \mu\mu$  selection described in Sec.6.2. The data sample consists of  $6 \text{ pb}^{-1}$ .

1393 and using a data sample from 2015 of  $80 \text{ pb}^{-1}$ . In these plots, ‘‘MET\_PFlow-TST’’  
 1394 refers to charged PFlow  $E_T^{\text{miss}}$ , while the other algorithms are as described above.

1395 Figures ?? show the resolution and scale in simulated  $Z \rightarrow \mu\mu$  events. The  
 1396 resolution curves follow the ‘‘intuitive’’ behavior discussed before. Due to the high  
 1397 pileup in 2015 run conditions, the CST  $E_T^{\text{miss}}$  resolution is poor, and becomes even  
 1398 poorer with increasing pileup and event activity. The ‘‘regular’’ PFlow  $E_T^{\text{miss}}$  shows  
 1399 reduces pileup and event activity dependence as compared to the CST. As stated  
 1400 earlier, the  $E_T^{\text{miss}}$  from the PFlow algorithm can be seen as a hybrid of TST  $E_T^{\text{miss}}$

1401 and CST  $E_T^{\text{miss}}$ . The charged PFOs ( $\sim 2/3$ ) are pileup suppressed, while the neutral  
1402 PFOs (or topoclusters) are not. Both charged PFlow and TST  $E_T^{\text{miss}}$  show only a  
1403 small residual dependence on  $N_{\text{PV}}$  and  $\sum E_T$ , since they have fully pileup suppressed  
1404 inputs through the track associations.

1405 The scale plots are shown for  $Z + \text{jets}$  events and  $Z$  events with no jets. For the  
1406 nonsuppressed CST, the scale continues to worsen with increasing  $p_T^Z$ . It is almost  
1407 always the worst performing algorithm. The standard PFlow algorithm performs the  
1408 second worst in the region of high  $p_T^Z$ , but is the best at low  $p_T^Z$ . The most exciting note  
1409 in this plot is the improved scale of the charged PFlow  $E_T^{\text{miss}}$  compared to the TST  
1410  $E_T^{\text{miss}}$ . Considering the resolution is essentially identical, the PFlow algorithm is better  
1411 picking up the contributions from additional neutral particles. In events with no jets,  
1412 the soft term is essentially the only indication of the  $E_T^{\text{miss}}$  mismeasurement, since  
1413 the muons will be well-measured. In this case, the pileup effects cancel, on average,  
1414 due to the  $U(1)_\phi$  symmetry of the ATLAS detector, and CST performs rather well  
1415 compared to the more complicated track-based algorithms. The full PFlow algorithm  
1416 performs best, since it provides a small amount of pileup suppression on the neutral  
1417 components from CST.

1418 The resolution and linearity are shown in simulated  $W \rightarrow e\nu$  events in Figure ???.  
1419 The resolution in  $W \rightarrow e\nu$  events shows a similar qualitative behavior to that shown  
1420 in  $Z \rightarrow \mu\mu$  events. The CST  $E_T^{\text{miss}}$  has the worst performance, with charged PFlow  
1421  $E_T^{\text{miss}}$  performing best. The surprise here is that the scale associated to TST  $E_T^{\text{miss}}$  in  
1422 these events is best throughout the space parameterized by  $E_T^{\text{miss,Truth}}$ , except for one  
1423 bin at  $40 \text{ GeV} < E_T^{\text{miss,Truth}} < 50 \text{ GeV}$ . The scale in these events is best measured  
1424 using a track-based soft term.

1425 The resolution also investigated in real data passing the  $Z \rightarrow \mu\mu$  selection  
1426 described above. A comparison of the  $E_T^{\text{miss}}$  between real data and simulation for  
1427 each algorithm is presented in Figure 6.16. The resolution as a function of  $\sum E_T$  and

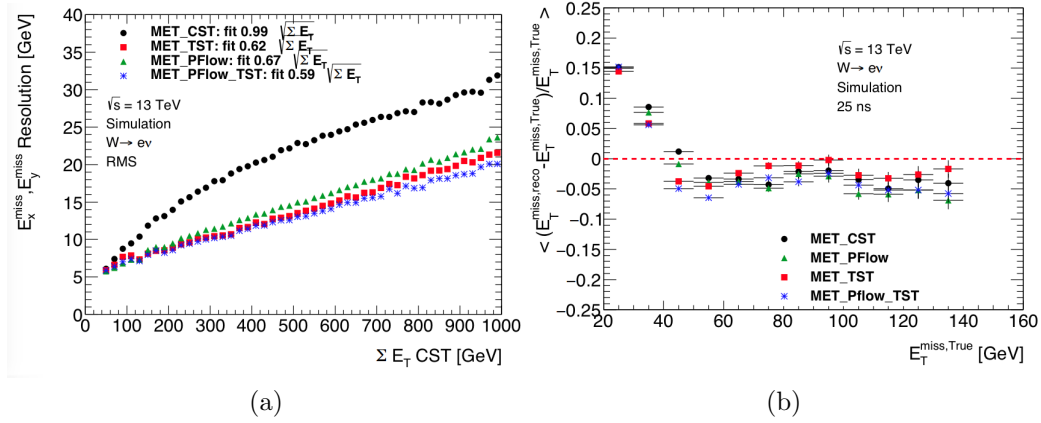


Figure 6.13: Comparison of  $E_T^{\text{miss}}$  resolution and linearity using different  $E_T^{\text{miss}}$  algorithms with simulated  $W \rightarrow e\nu$  events.

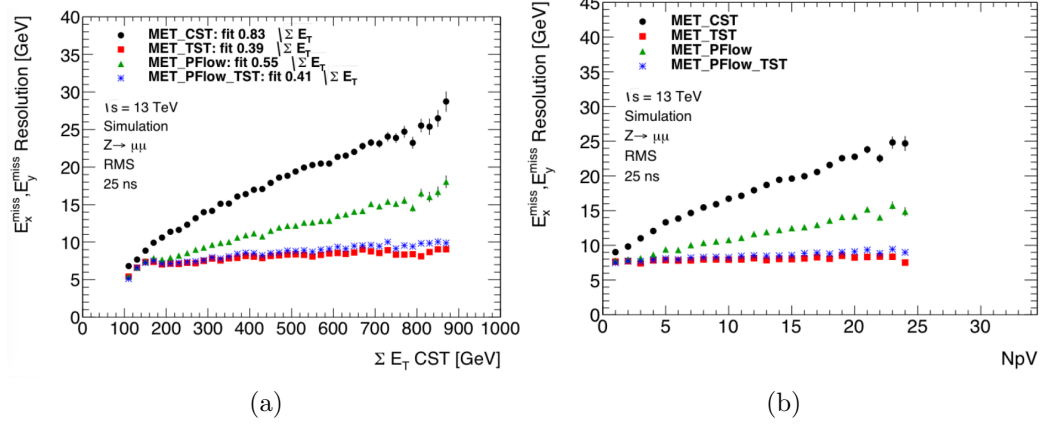


Figure 6.14: Comparison of  $E_T^{\text{miss}}$  resolution using different  $E_T^{\text{miss}}$  algorithms with simulated  $Z \rightarrow \mu\mu$  events.

1428  $N_{\text{PV}}$  is shown in Figure 6.17 for this dataset. Overall, this plot shows the same general  
 1429 features as the simulation dataset in terms of algorithm performance. However, the  
 1430 performance of all algorithms seems to be significantly worse in data. This is likely due  
 1431 to simplifications made in the simulation: soft interactions that cannot be simulated  
 1432 can have a significant effect on an event level variable such as the  $E_T^{\text{miss}}$  resolution.

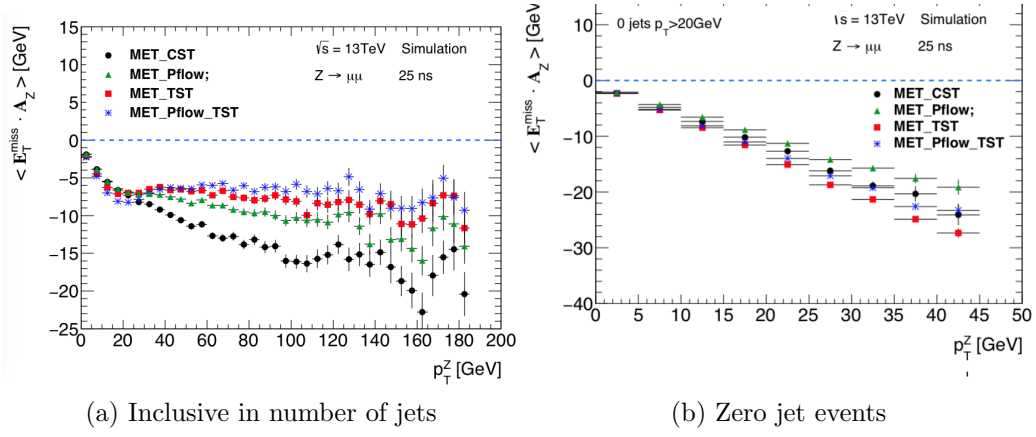


Figure 6.15: Comparison of  $E_T^{\text{miss}}$  scale using different  $E_T^{\text{miss}}$  algorithms with simulated  $Z \rightarrow \mu\mu$  events.

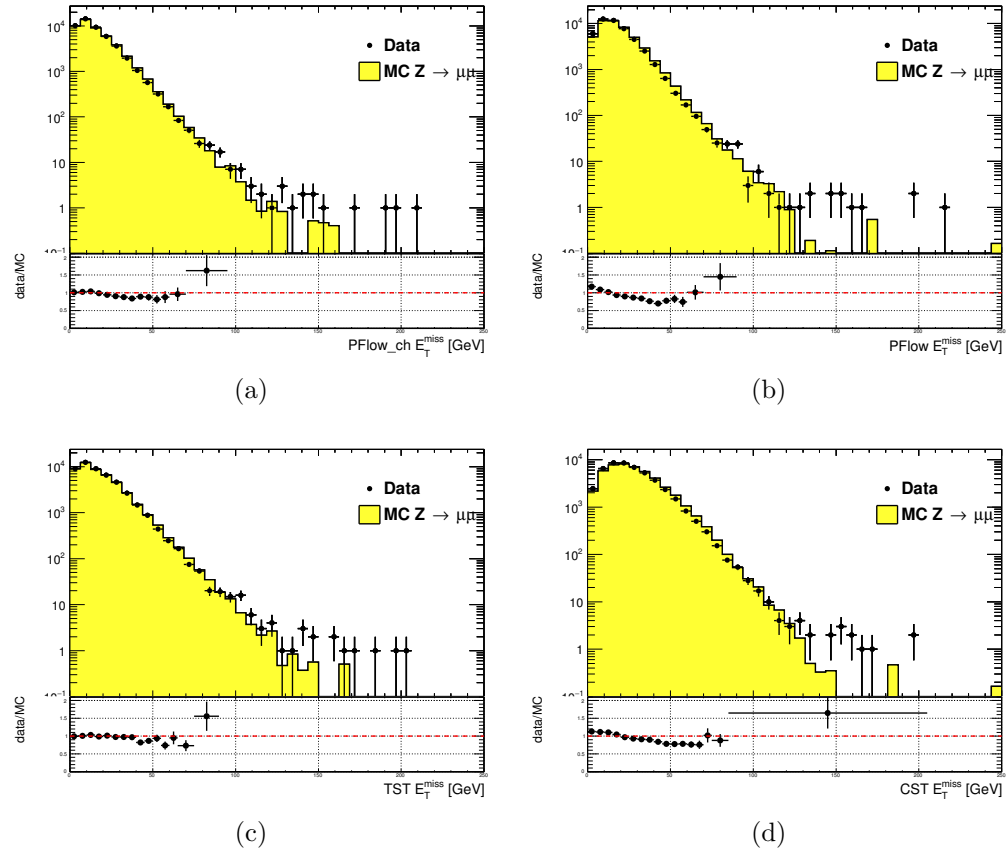


Figure 6.16: Comparison of  $E_T^{\text{miss}}$  distributions using different  $E_T^{\text{miss}}$  algorithms with a data sample of  $80 \text{ pb}^{-1}$  after the  $Z \rightarrow \mu\mu$  selection described in Sec.6.2

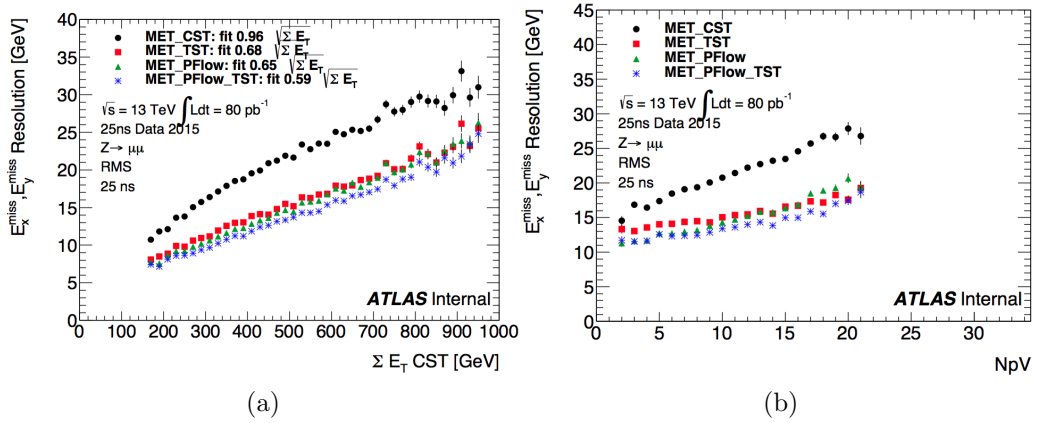


Figure 6.17: Comparison of  $E_T^{\text{miss}}$  resolution using different  $E_T^{\text{miss}}$  algorithms with a data sample of  $80 \text{ pb}^{-1}$  after the  $Z \rightarrow \mu\mu$  selection described in Sec. 6.2

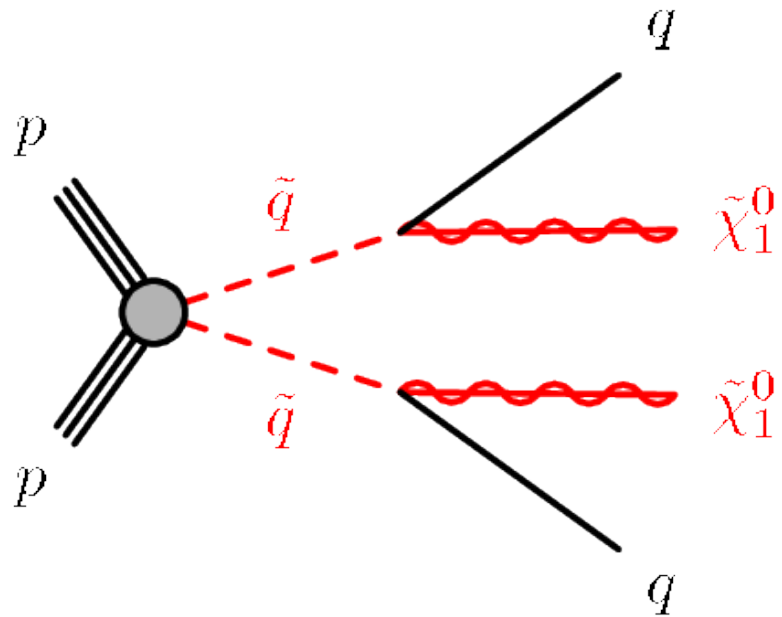
*Recursive Jigsaw Reconstruction*

1435 *Recursive Jigsaw Reconstruction* (RJR) [114, 115] is a novel algorithm used for the  
 1436 analysis presented in this thesis. RJR is the conceptual successor to the razor  
 1437 technique [116, 117], which has been used successfully in many new physics searches  
 1438 [37, 38, 40, 41, 47, 118]. In this chapter, we will first present the razor technique,  
 1439 and describe the razor variables. We will then present the RJR algorithm. After the  
 1440 description of the algorithm, we will describe the precise RJR variables used by this  
 1441 thesis and attempt to provide some physical intuition of what they describe.

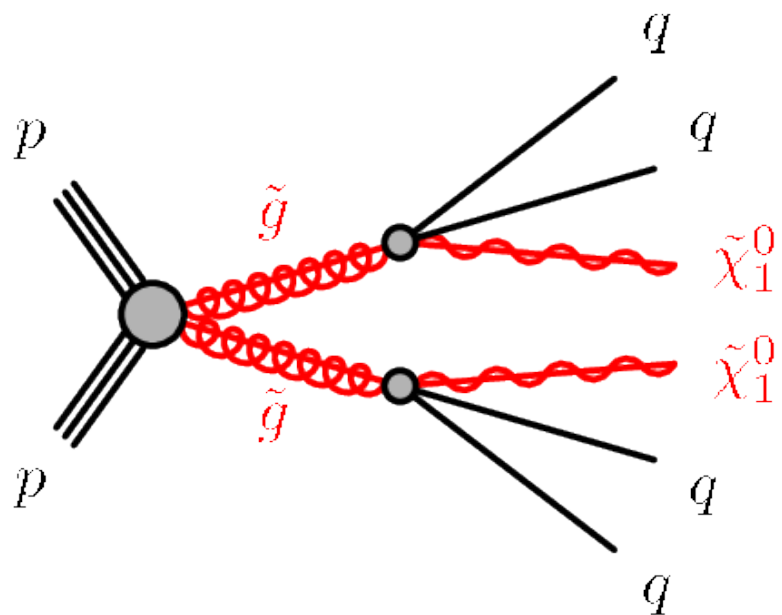
1442 **7.1 Razor variables**1443 **Motivation**

1444 In this thesis, we consider SUSY models where gluinos and squarks are pair-produced.  
 1445 Pair-production is a consequence of the  $R$ -parity imposed in many SUSY models.  
 1446  $R$ -parity violation is highly constrained by limits on proton decay[15], and is often  
 1447 assumed in SUSY model building. The Feynman diagrams considered are shown in  
 1448 Fig.7.1.

1449 As discussed previously, the consequences of this  $\mathbb{Z}_2$  symmetry are drastic. To un-  
 1450 derstand the utility of the razor variables, the stability of the lightest supersymmetric  
 1451 particle is very important. In many SUSY models, including the ones considered in  
 1452 this thesis, this is the lightest neutralino  $\tilde{\chi}_1^0$ . This means that on either side of a  
 1453 SUSY decay process, where we begin with disparticle production, we have a final



(a) Disquark production



(b) Digluino production

Figure 7.1: Feynman diagrams for the SUSY signals considered in this thesis

1454 state particle which is not detected. Generically, this leads to  $E_T^{\text{miss}}$ . Selections based  
1455 on  $E_T^{\text{miss}}$  are very good at reducing dominant backgrounds, for example from QCD  
1456 backgrounds.

1457 However, there are limitations to searches based on  $E_T^{\text{miss}}$ . Due to jet mismeasurements,  
1458 instrumental failures, finite detector acceptance, nongaussian tails in the  
1459 detector response, and production of neutrinos inside of jets, there are many sources of  
1460 “fake”  $E_T^{\text{miss}}$  which does not correspond to a Standard Model neutrino or new physics  
1461 object such as an LSP. An additional limitation is the complete lack of longitudinal  
1462 information. As events from i.e. QCD backgrounds tend to have higher boosts along  
1463 the  $z$ -direction, this is ignoring an important handle in searches for new physics.  
1464 Finally,  $E_T^{\text{miss}}$  is only one object, which is a measurement for *two* separate LSPs. If one  
1465 could factorize this information somehow, this would provide additional information  
1466 to potentially discriminate against backgrounds. The *razor variables* ( $M_{\Delta}^R, R^2$ ) are  
1467 more robust than standard variables against these effects[[116](#), [117](#)].

## 1468 Derivation of the razor variables

1469 To derive the razor variables ( $M_{\Delta}^R, R^2$ ), we start with a generic situation of the pair  
1470 production of heavy sparticles with mass  $m_{\text{Heavy}}$ .<sup>1</sup> Each sparticle decays to a number  
1471 of observable objects (in this thesis, jets), and an unobservable  $\tilde{\chi}_1^0$  of mass  $m_{\tilde{\chi}_1^0}$ . We  
1472 will combine all of the jets into a *megajet*; this process will be described below. We  
1473 begin by analyzing the decay in the “rough-approximation”, or in modern parlance,  
1474 *razor frame* (*R-frame*). This is the frame where each sparticle is at rest. The complete  
1475 set of frames considered in the case of the razor variables is shown in [7.2](#).

In the *R-frame*, the decay is straightforward to analyze. By construction, there  
are in fact two *R-frame* s, and they have identical kinematics. Each megajet has

---

<sup>1</sup>The razor variables have undergone confusing notational changes over the years. We will be self-consistent, but the notation used here may be different from references.

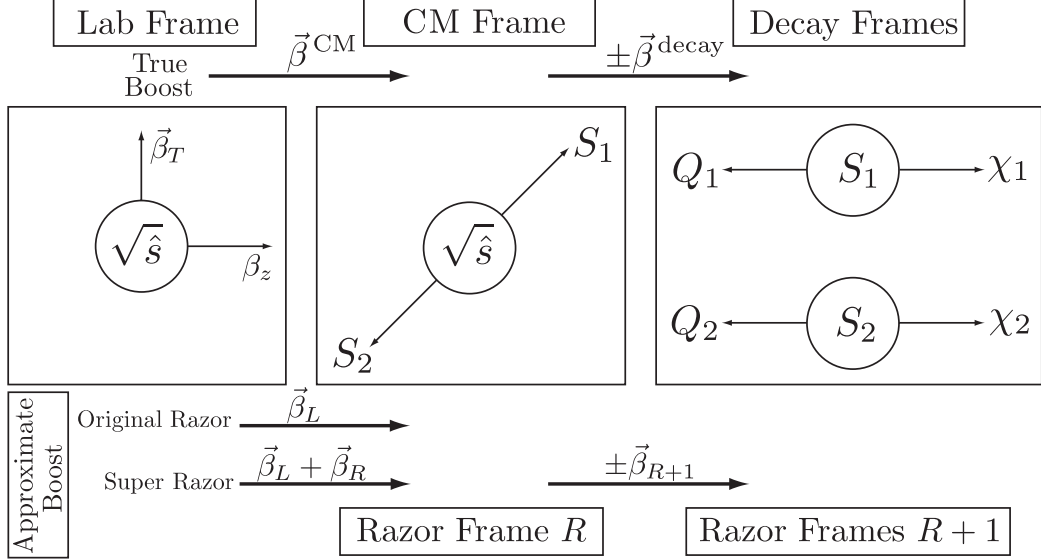


Figure 7.2: Frames considered when applying the razor technique, from [117].

energy  $E_1^R, E_2^R$  in the frame of its parent sparticle, and we define a characteristic mass  $M_R$ :

$$E_1^R = E_2^R = \frac{m_{\text{Heavy}}^2 - m_{\tilde{\chi}_1^0}^2}{2m_{\text{Heavy}}} \quad (7.1)$$

$$M_R = 2 \times E_1^R = 2 \times E_2^R = \frac{m_{\text{Heavy}}^2 - m_{\tilde{\chi}_1^0}^2}{m_{\text{Heavy}}} \quad (7.2)$$

For cases where  $m_{\text{Heavy}} \gg m_{\tilde{\chi}_1^0}$ ,  $M_R$  is an estimator of  $m_{\text{Heavy}}$ . This scenario happens in the SM, such as in  $t\bar{t}$  and  $WW$  events, where the  $\tilde{\chi}_1^0$  is instead a neutrino.

The question now is how to use this simple derivation in the lab frame, where we actually have measurements. There are two related issues: how to combine the jets into the megajets, and how to “transform” (or *boost*) to the  $R$ -frame.

To construct the megajets, the procedure is the following. For a given set of jets  $j_i, i = 0, \dots, n_{\text{jet}}$ , we construct *all* combinations of their four-momenta such that there is at least one jet inside each megajet. Among this set of possible megajets  $\{J_{1,2}\}$ , we make the following unique choice for the megajets. We minimize the following quantity:

$$m_{J_1}^2 + m_{J_2}^2. \quad (7.3)$$

1481 In modern parlance, this is known as a *jigsaw*. It is important to note, this is a  
 1482 *choice*. It may have nice physical qualities or satisfy some convenient intuition about  
 1483 the events, but as we will see later, other choices are possible.

We now describe how we translate our megajet kinematics, measured in the lab frame, to the  $R$ -frame. This is a two-step procedure. We perform two *boosts*: a longitudinal boost  $\beta_L$  and a transverse boost  $\beta_T$ . Schematically,

$$J_1^R \xrightarrow{\beta_T} J_1^{CM} \xrightarrow{\beta_L} J_1^{\text{lab}} \quad (7.4)$$

$$J_2^R \xrightarrow{-\beta_T} J_2^{CM} \xrightarrow{\beta_L} J_2^{\text{lab}} \quad (7.5)$$

$$(7.6)$$

1484 The  $J_{1,2}^{\text{lab}}$  correspond directly to those in the megajet construction. We drop the  
 1485 “lab” designation for the rest of the discussion. The question is how to compute the  
 1486 magnitudes of these boosts, given the missing degrees of freedom.

For the transverse boost  $\beta_T$ , recall the two megajets have equal energies in their  $R$ -frame by construction. This constraint can be reexpressed as a constraint on the magnitude of this boost, in terms of the boost velocity  $\beta_L$  (and Lorentz factor  $\gamma_L$ ):

$$\beta_T = \frac{\gamma_L(E_1 - E_2) - \gamma_L\beta_L(p_{1,z} - p_{2,z})}{\hat{\beta}_T \cdot (\vec{p}_{1,T} + \vec{p}_{2,T})} \quad (7.7)$$

where we have denoted the lab frame four-vectors as  $p_i = (E_i, \vec{p}_{i,T}, p_z)$ . We now make the *choice* for the direction of the transverse boost  $\hat{\beta}_T$ :

$$\hat{\beta}_T = \frac{\vec{p}_{1,T} + \vec{p}_{2,T}}{|\vec{p}_{1,T} + \vec{p}_{2,T}|}. \quad (7.8)$$

1487 This choice forces the denominator of 7.7 to unity, and corresponds to aligning the  
 1488 transverse boost direction with the sum of the two megajets transverse directions.

For the longitudinal boost, we choose  $\vec{\beta}_L$  along the  $z$ -direction, with magnitude:

$$\beta_L = \frac{p_{1,z} + p_{2,z}}{E_1 + E_2}. \quad (7.9)$$

1489 Viewed in terms of the original parton-parton interactions, this is the choice which  
 1490 “on average” gives  $p_{z,\text{CM}} = 0$ , as we would expect. This well-motivated choice due to  
 1491 the total  $z$  symmetry.

We now have well-motivated guesses for both boosts, which allow us write our original characteristic mass  $M_R$  in terms of the lab frame variables, by application of these two Lorentz boosts to the energies of 7.1:

$$M_R^2 \xrightarrow{\beta_T} M_{R,\text{CM}}^2 \xrightarrow{\beta_L} M_{R,\text{lab}}^2 = (E_1 + E_2)^2 - (p_{1,z} + p_{2,z})^2. \quad (7.10)$$

Finally, we define an additional mass variable, which include the missing transverse energy  $E_{\text{T}}^{\text{miss}}$ . Importantly, note that we did not use the  $E_{\text{T}}^{\text{miss}}$  in the definition of  $M_R$ , which depends only on the energies of the megajets. Backgrounds with no invisible particles (such as multijet events) must have  $J_1$  and  $J_2$  back to back. Thus, we define the transverse mass:

$$(M_R^T)^2 = \frac{1}{2} \left[ E_{\text{T}}^{\text{miss}}(p_{1,T} + p_{2,T}) - \vec{E}_{\text{T}}^{\text{miss}} \cdot (\vec{p}_{1,T} + \vec{p}_{2,T}) \right]. \quad (7.11)$$

Generally, we have  $M_R^T < M_R$ , so we define a dimensionless ratio (“the razor”):

$$R^2 = \left( \frac{M_R^T}{M_R} \right)^2. \quad (7.12)$$

1492 For signal events, we expect  $R$  to peak around  $R \sim 1/4$ , while backgrounds without  
 1493 real  $E_{\text{T}}^{\text{miss}}$  are expected to have  $R \sim 0$ .

## 1494 7.2 Recursive Jigsaw Reconstruction

1495 Recursive Jigsaw Reconstruction is an algorithm allowing the imposition of a decay  
 1496 tree interpretation on an particular event[114, 115]. The idea is to construct the  
 1497 underlying kinematic variables (the masses and decay angles) on an event-by-event  
 1498 level. This is done “recursively” through a decay tree which corresponds (sometimes  
 1499 approximately) to the Feynmann diagram for the signal process of interest. After

1500 each step of the recursive procedure, the objects are “placed” into one bucket (or  
1501 branch) of the decay tree, and the process is repeated on each frame we have imposed.  
1502 The imposition of these decay trees is done by *jigsaw* rule: a procedure to resolve  
1503 combinatoric or kinematic ambiguities while traversing the decay tree. This procedure  
1504 is performed by the `RestFrames` software packages [119]

1505 In events where all objects are fully reconstructed, this is straightforward, and  
1506 of course has been used for many years in particle physics experiments. Events  
1507 which contain  $E_T^{\text{miss}}$  are more difficult, due to the loss of information: the potential  
1508 for multiple mismeasured or simply unmeasureable objects, such as neutrinos or the  
1509 LSP in SUSY searches. There can also be combinatoric ambiguities in deciding how  
1510 to group objects of the same type; specifically here, we will be concerned with the  
1511 jigsaw rule to associate jets to a particular branch of a decay tree. The jigsaw rules  
1512 we impose will remove these ambiguities. First, we will describe the decay trees used  
1513 in this thesis, and then describe the jigsaw rules we will use. Finally, we will describe  
1514 the variables used in the all-hadronic SUSY search presented in this thesis.

## 1515 Decay Trees

1516 The decay trees imposed in this thesis are shown in 7.3. Leaving temporarily the  
1517 question of “how” we apply the jigsaw rules, let us compare these trees to the signal  
1518 processes of interest. In particular, we want to compare the Feynman diagrams of 7.1  
1519 with the decay trees of 7.3. The decay tree in ?? corresponds exactly to that expected  
1520 from disquark production, and matches very closely with the principles of the razor  
1521 approach. We first apply a jigsaw rule, indicated by a line, to the kinematics of the  
1522 objects in the *lab* frame. This outputs the kinematics of our event in the *parent-parent*  
1523 (*PP*) frame, or in the razor terminology, the CM frame. That is, the kinematics of  
1524 this frame are an estimator for the kinematics in the center of mass frame of the  
1525 disquark system. We apply another jigsaw, which splits the objects in the *PP* frame

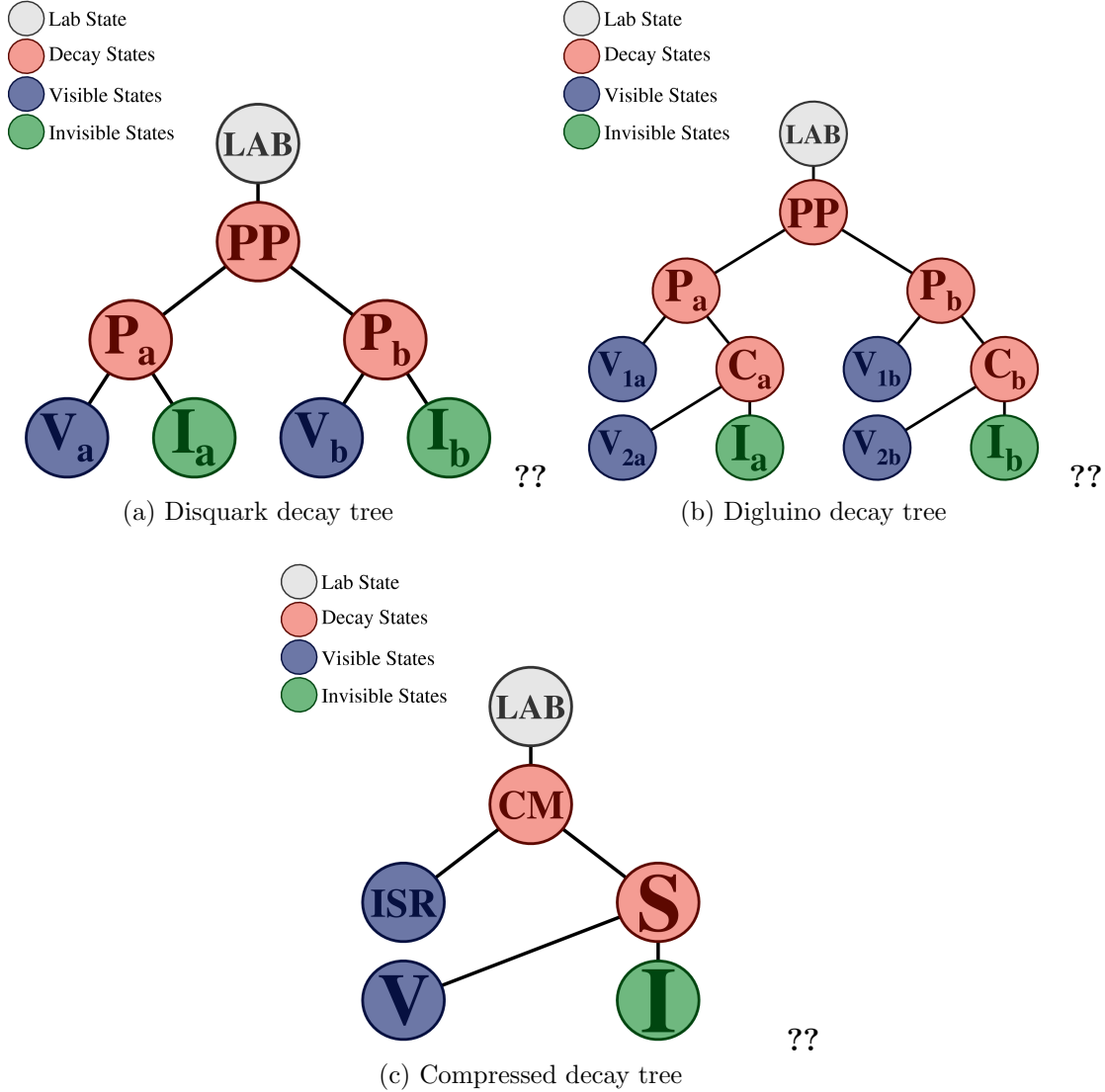


Figure 7.3: RJR decay trees imposed in this thesis

1526 into two new frames, known as the  $P_a$  and  $P_b$  systems. These are equivalent to the  
 1527 razor frames of the razor technique, and represent proxy frames where each squark  
 1528 is at rest. In  $P_a(P_b)$ , the decay is symmetric between the visible  $V_a(V_b)$  objects and  
 1529 the invisible system  $I_a(I_b)$ . To generate the estimator of the kinematics of the  $V_a$ ,  $V_b$ ,  
 1530  $I_a$ , and  $I_b$  systems in the  $P_a$  and  $P_b$  systems, we apply another jigsaw rule to split the  
 1531 total  $E_T^{\text{miss}}$  between  $P_a$  and  $P_b$ , which allows calculations of these kinematics in these  
 1532 frames. For the case of disquark production, this is the expected decay tree, and we

1533 stop the recursive calculation at that level.

1534 In the case of digluino production, we expect two additional jets, and we can  
1535 perform an additional boost in each of  $P_a$  and  $P_b$ , to what we call the  $C_a$  and  $C_b$  frames.  
1536 The decay tree is shown in ?? . In this case we apply a jigsaw at the level of  $P_a(P_b)$   
1537 which separates a single visible object  $V_{1a}$  ( $V_{2a}$ ) from the child frame  $C_a(C_b)$ . This  
1538 child frame represents the hypothesized squark after the decay  $\tilde{g} \rightarrow g\tilde{q}$ , which then  
1539 decays as in the squark case. This gives additional information which will be exploited  
1540 for the gluino specific search regions.

The final decay tree used in this thesis is the *compressed* decay tree. Compressed refers to signal models which have a small splitting between the mass of the proposed sparticle and the  $\tilde{\chi}_1^0$ . In this case, the sparticle decay products (i.e. the jets and  $E_T^{\text{miss}}$ ) do not generally have large scale[114]. Instead, the strategy is generally to look for a large-scale initial state radiation (ISR) jet which is recoiling off the disparticle system. In the case where the LSPs receive no momentum from the sparticle decays, the following approximation holds:

$$E_T^{\text{miss}} \sim -p_T^{\text{ISR}} \times \frac{m_{\tilde{\chi}_1^0}}{m_{\text{sparticle}}} \quad (7.13)$$

1541 where  $p_T^{\text{ISR}}$  is the transverse momentum associated to the entire ISR system.

1542 RJR offers a natural and straightforward way to exploit this feature in events  
1543 containing ISR. One imposes the simple decay tree in ?? with associated jigsaw rules.  
1544 With suitable jigsaw rules, this decay tree “picks out” the large  $p_T$  ISR jet, recoiling  
1545 off the  $E_T^{\text{miss}}$  and additional radiation from the sparticle decays. This provides a  
1546 convenient set of variables to understand compressed scenarios.

1547 In this section, we have seen how one imposes particular decay trees on an event  
1548 to produce a basis of kinematic variables in the approximated frames relevant to  
1549 the hypothesized sparticle decay chain. This explains why we call this procedure  
1550 “recursive”: we can continue the procedure through as many steps of a decay tree as

1551 we want, and each application of a jigsaw rule is dependent on the variables produced  
1552 in the last step. The question, of course, is *what are these jigsaw rules?*.

1553 **Jigsaw Rules**

1554 Jigsaw rules are the fundamental step that allow the recursive definitions of the  
1555 variables of interest. We want rules which allow us to fully define kinematic variables  
1556 at each step in a decay tree. The only possible solution to fully define the event  
1557 kinematics in terms of the frames of the hypothesized decays is the imposition of  
1558 external constraints to eliminate additional degrees of freedom. In principle, these  
1559 need not have any particular physical motivation. Instead, the jigsaw rules are a  
1560 way to resolve the mathematical ambiguities to fully reconstruct the full decay chain  
1561 kinematics. However, most practical jigsaw rules also have some reasonable physical  
1562 motivation, which we will also elucidate.

1563 In the original razor point of view, some jigsaw rules can be seen as the definitions  
1564 of the boosts which relate the different frames of interest, while other rules allow one  
1565 to combine multiple objects and place them into a particular hemisphere (previously  
1566 megajet). These are the two forms of jigsaw rules: combinatoric and kinematic. As  
1567 we have stressed before, the jigsaw rules are a *choice*; as long as a particular jigsaw  
1568 rule allows the definition of variables at each step in a decay tree, it is “as valid” as  
1569 any other rule.

Practically speaking, in this thesis we use only a small subset of possible jigsaw rules. The combinatoric jigsaw rule we use has already been introduced as megajet construction above. The minimization of

$$m_{J_1}^2 + m_{J_2}^2. \quad (7.14)$$

1570 is a jigsaw rule to deal with the combinatoric ambiguity implicit in which jets go in  
1571 which hemisphere. This is the jigsaw rule used in the decay trees when going from

1572 one frame to two frames such as  $PP \rightarrow P_a, P_b$ .

1573 We will use three other jigsaw rules, which are both kinematic jigsaw rules. One  
1574 has already been used in the razor technique. The minimization of  $\beta_L$  will be used  
1575 as the jigsaw rule in the first step of each decay tree: the lab frame to the  $PP/\text{CM}$   
1576 frame. This is in effect the imposition of longitudinal boost invariance, as we expect  
1577 on average  $p_{z,PP,\text{CM}} = 0$ . One defines a unique longitudinal boost by imposition of  
1578 this external constraint.

1579 The final two jigsaw rules used in this thesis was not used in the razor technique.

1580 We describe them here.

The first kinematic ambiguity is the total mass of the invisible system  $M_I$ . We  
guess this to be:

$$M_I^2 = M_V^2 - 4M_{V_a}M_{V_b}. \quad (7.15)$$

1581 As we stated above, there is no need to “justify” the jigsaw rules, as they are in some  
1582 ways a mathematical trick to fully resolve the event kinematics. However in this case,  
1583 there is a nice property of this guess. The symmetry of the production mechanism,  
1584 where we have two decay products  $V_i$  and  $I_i$  produced from the decay of the same  
1585 heavy sparticle, is explicit with this jigsaw choice.

1586 The final jigsaw rule we employ in this thesis is used to resolve the “amount” of  
1587  $E_T^{\text{miss}}$  that “belongs” to each hemisphere, and therefore how to impose the transverse  
1588 boost onto each of i.e.  $P_a$  and  $P_b$  from  $PP$ . Equivalently, it can be seen as the  
1589 resolution of the kinematics of the  $I_a$  and  $I_b$  objects in the disquark and digluino  
1590 decay trees. Recall that at this point, we have already approximated the boost  
1591 of the  $PP$  frame. The choice we use is to minimize the masses  $P_a$  and  $P_b$ , while  
1592 simultaneously constraining  $P_a = P_b$ . As is the case in the last step, there is a  
1593 straightforward physical interpretation of this choice. In the signal models we are  
1594 considering,  $P_a$  and  $P_b$  are the estimated frames of the squark or gluino pair-produced  
1595 as a heavy resonance. We then of course expect  $M_{P_a} = M_{P_b}$ .

1596     The imposition of the decay trees, with ambiguities resolved through the jigsaw  
1597    rules, give a full set of boosts relating the frames of each decay tree. In each frame,  
1598    we have estimates for the frame mass and decay angles, which can be used in searches  
1599    for new physics. In the next section, we describe the variables that are used in this  
1600    thesis in more details.

## 1601   **7.3 Variables used in the search for zero lepton**

### 1602   **SUSY**

1603   We describe here the variables used in the search described in ???. These were  
1604   reconstructed using the RJR algorithm as just described, using the RestFrames  
1605   packages[119]. In these frames, the momenta of all objects placed into that branch  
1606   of the decay tree are available (after application of the approximated boost), and in  
1607   principle we can calculate any variable of interest such as invariant masses or the  
1608   angles between these objects. The truly useful set of variables are highly dependent  
1609   on the signal process, and we leave their discussion to the subsequent chapters. It is  
1610   useful to understand the philosophy employed in the construction of these variables.

1611   In general, we can split variables useful for searches for new physics into two  
1612   categories: *scaleful* and *scaleless* variables. In this search, we will use a set of scaleful  
1613   variables called the  $H$  variables. The scaleless variables will consists of ratios and  
1614   angles. In general, we want to limit the number of scaleful cuts we apply, for two  
1615   reasons. Different scaleful variables are often highly correlated, and this of course  
1616   limits the utility of additional cuts. Addtionally, selections based on many scaleful  
1617   variables often “over-optimize” for particular signal model of interest, especially as  
1618   related to the mass difference chosen between the sparticle and the LSP. To avoid  
1619   this, each decay tree will only use two scale variables, one of which quantifies the  
1620   overall mass scale of the event, and another which acts as a measure of the event

1621 balance.

## 1622 Squark and gluino variables

1623 Taking our general philosophy to a particular case, we here describe the variables  
1624 used by the squark and gluino searches. We have a suite of scale variables which we  
1625 will call the  $H$  variables, and a suite of angles and ratios.

1626 As we have described above, the RJR algorithm gives us access to the masses of  
1627 each frame of interest. It maybe seem natural, then, that these variables would be the  
1628 most useful for discrimination of the signal from background processes. However, due  
1629 to the all hadronic state considered in this thesis, the that can be constructed such  
1630 as  $M_{PP}$  can be affected by extra QCD radiation, which can promote the background  
1631 processes to large scales. The  $H$  variables show a resilience to this effect. They  
1632 take their name from the commonly used variable  $H_T$ , which is the scalar sum of  
1633 the visible momentum. However, due to the RJR technique, we can evaluate these  
1634 variables in the non-lab frame, including longitudinal information. They are also  
1635 constructed with *aggregate* momenta using a similar mass minimization procedure  
1636 as we have already described.

We label these variables as  $H_{n,m}^F$ . The frame from where they are evaluated is denoted  $F$ ; practically, this means  $F \in \{\text{lab}, PP, P_a, P_b\}$ . When the discussion applies to both  $P_a$  and  $P_b$ , we will write  $P_i$ . The subscripts  $n$  and  $m$  denote the number of visible and invisible vectors considered, respectively. When there are more vectors available than  $n$  or  $m$ , we add up vectors using the hemisphere (megajet) jigsaw rule until there are  $n$  ( $m$ ) objects.<sup>2</sup> In the opposite case, where  $n$  or  $m$  is greater than the number of available objects, one simply considers the available objects. The  $H_{n,m}^F$

---

<sup>2</sup>Recall that these vectors are constructed by the imposition of the decay tree with the relevant jigsaw rules.

variables are then defined as

$$H_{n,m}^F = \sum_i^n |\vec{p}_{\text{vis},i}^F| + \sum_j^m |\vec{p}_{\text{inv},i}^F|. \quad (7.16)$$

It may not be clear that these variables encode independent information. Fundamentally, this is just an expression of the triangle inequality  $\sum |\vec{p}| \geq |\sum \vec{p}|$ . The different combinations can then include independent information. The final note on the  $H$  variables is that we can also consider purely transverse versions of these variables, which we will denote  $H_{T,n,m}^F$ . Including this view, it is easy to see how the  $H$  variables are extensions of the normal  $H_T$  variables, as

$$H_T = H_{T,\infty,0}^{\text{lab}}. \quad (7.17)$$

1637     Although the  $H$  variables are interesting in their own right, the true power of the  
 1638     RJR technique comes from the construction of scaleless variables with the technique.  
 1639     This is because the scaleless ratios and angles are in fact measured in the “right”  
 1640     frame, where right here means an approximation of the correct frame. This provides  
 1641     a less correlated set of variables than those measured in the lab frame, due to the  
 1642     corrections to the disparticle or sparticle system boosts from the RJR technique.  
 1643     For the search for noncompressed disquark production, we use will use the  
 1644     following set of RJR variables.

- 1645     •  $H_{1,1}^{PP}$  - scale variable useful for discrimination against QCD backgrounds and  
 1646         used in a similar way to  $E_T^{\text{miss}}$
- 1647     •  $H_{T,2,1}^{PP}$  - scale variable providing information on the overall mass scale of the  
 1648         event for disquark signal production. We will often call this the *full* scale  
 1649         variable.
- 1650     •  $H_{T,1,1}^{PP}/H_{2,1}^{PP}$  - ratio used to prevent imbalanced events where the scale variable  
 1651         is dominated by one high  $p_T$  jet or high  $E_T^{\text{miss}}$

1652     •  $p_{PP,z}^{\text{LAB}}/(p_{PP,z}^{\text{LAB}} + H_{T,2,1}^{PP})$  - ratio to used to prevent significant boosts in the  
1653        $z$ -direction.  $p_{PP,z}^{\text{LAB}}$  is a measure of the total boost of the  $PP$  system from the lab  
1654       frame

1655     •  $p_{T,j2}^{PP}/H_{T,2,1}^{PP}$  - ratio to force the second leading jet in the  $PP$  frame to carry a  
1656       significant portion of the total scalar sum in that frame. This requirement is  
1657       another balance requirement, on the total  $p_T$  of that second jet in the  $PP$  frame.

1658     First, we note that there is an implicit requirement that each hemisphere has at least  
1659       one jet (to even reconstruct the  $P_a$  and  $P_b$  frames), these variables are implicitly using  
1660       two or more jets, as we expect in disquark production. The other important thing  
1661       to note is that all of the ratios use the full scale variable as the denominator. This  
1662       is sensible, as we expect all of these effects to be scaled with the full scale variable  
1663        $H_{T,2,1}^{PP}$ . We will see a similar behavior for the gluino regions, with a new full scale  
1664       variable.

1665     For the search for noncompressed digluino production, we use will use the following  
1666       set of RJR variables. Due to the increased complexity of the event topology with four  
1667       jets, there are additional handles we can exploit:

1668     •  $H_{1,1}^{PP}$  - same as disquark production

1669     •  $H_{T,4,1}^{PP}$  - scale variable providing information on the overall mass scale of the  
1670       event for digluino signal production. As before, we often call this the *full* scale  
1671       variable. Since this variable allows the jets to be separated in the  $PP$  frame, it  
1672       is more appropriate for digluino production.

1673     •  $H_{T,1,1}^{PP}/H_{4,1}^{PP}$  - ratio used to prevent imbalanced events where the scale variable  
1674       is dominated by one high  $p_T$  jet or high  $E_T^{\text{miss}}$

1675     •  $H_{T,4,1}^{PP}/H_{4,1}^{PP}$  - ratio used to measure the fraction of the total scalar sum of the  
1676       momentum in the transverse plane. Digluino production is expected to be fairly

- 1677            central
- 1678        •  $p_{PP,z}^{\text{LAB}}/(p_{PP,z}^{\text{LAB}} + H_{T,4,1}^{PP})$  - ratio to used to prevent significant boosts in the  
 1679             $z$ -direction
- 1680        •  $\min(p_{T,j2}^{PP}/H_{T,2,1}^{PP})$ - ratio to require the second leading jet in *both* squark-like  
 1681            hemispheres  $C_a$ and  $C_b$ to contain a significant portion of *that frame's* momenta.  
 1682            This is similar to the  $p_{T,j2}^{PP}/H_{T,2,1}^{PP}$ disquark discriminator, but applied to both  
 1683            hemispheres  $C_a$ and  $C_b$ .
- 1684        •  $\max(H_{1,0}^{P_i}/H_{2,0}^{P_i})$ - ratio requiring one jet in each of the  $P_i$  to not take too much  
 1685            of the total momentum of that frame. This ratio is generally a very loose cut.

## 1686 Compressed variables

1687 As we saw above, the decay tree imposed for compressed spectra is simpler. We do  
 1688 not attempt to fully reconstruct the details of the system recoiling of the ISR system,  
 1689 but use a straightforward set of variables in this case. One additional simplification  
 1690 is that all variables are force to be transverse in this case; we simply do not include  
 1691 the  $\eta/z$  information of the objects as inputs to the RJR reconstruction. We still use  
 1692 the philosophy of limiting our scaleful variables to just two. The compressed scenario  
 1693 uses the following set of RJR variables:

- 1694        •  $p_{T,S}^{\text{ISR}}$ - scale variable that is the magnitude of the total transverse momenta of all  
 1695            jets associated to the ISR system, as evaluated in the CM frame
- 1696        •  $R_{\text{ISR}} \equiv p_I^{\vec{C}\text{M}} \cdot p_{T,S}^{\hat{C}\text{M}}/p_{T,S}^{\text{CM}}$  - this ratio is our measurement for the ratio of the LSP  
 1697            mass to the compressed sparticle mass. These are the values in the CM frame  
 1698            In compressed cases, this should be large, as this estimates the amount of the  
 1699            total  $\text{CM} \rightarrow S$  boost is carried by the invisible system.
- 1700        •  $M_{T,S}$ - the transverse mass of the S system

- 1701 •  $N_{\text{jet}}^V$ - the number of jets associated to the visible system V
- 1702 •  $\Delta\phi_{ISR,I^-}$  the opening angle between the ISR system and the invisible system  
1703 measured in the lab frame. As the invisible system is expected to carry much  
1704 of the total  $S$  system momentum, this should be large, as we expect the ISR  
1705 system to recoil directly opposite the  $I$  system in that case.



*Title of Chapter 1*

1708 This section presents the details of the first search employing RJR variables as  
 1709 discriminating variables, as described in ???. We will describe the data and simulation  
 1710 samples used, and then define the selections where we search for new SUSY  
 1711 phenomena, which we call the *signal regions* (SRs) Afterwards, we describe the  
 1712 background estimation techniques used in the analysis. Finally, we discuss the  
 1713 treatment of systematic uncertainties, and how we combine them using a likelihood  
 1714 method[120].

1715 **8.1 Collision data and simulation samples**

1716 Simulated data is fundamentally important to the ATLAS physics program. Cali-  
 1717 brations, measurements, and searches use Monte Carlo (MC) simulations<sup>1</sup>to compare  
 1718 with collision data. In this thesis, MC samples are used to optimize the signal region  
 1719 selections, assist in background estimation, and assess the sensitivity to specific SUSY  
 1720 signal models. The details of Monte Carlo production, accuracy, and utility are far  
 1721 beyond the scope of this thesis, but we provide a short description here.

1722 The first step is MC *generation*. A program is run which does a matrix-element  
 1723 calculation, sometimes with additional corrections, which produces a set of output  
 1724 particles from the parton interactions. These output particles are then decayed via  
 1725 another (or the same) simulation program. This produces a set of *truth* particles,

---

<sup>1</sup>In jargon, often just called “Monte Carlo” or MC.

1726 which are the output of event generation. The details of which generator to use are  
1727 the subject of much discussion, and generally (many) comparisons are made between  
1728 them, for different processes of interest. Additionally, differences between generators  
1729 are often a starting point for the calculation of systematic uncertainties.

1730 The next step is the *simulation*. The detector response to the truth particles  
1731 is simulated, and simulated hits are produced. After simulation, the standard  
1732 reconstruction algorithms described previously are run with the simulated hits. This  
1733 procedure ensures “as close as possible” treatment of simulation and collision data.

1734 We give a brief description of which samples use which generators; additional  
1735 details are available in ??.

1736 **MAKE BETTER** Signal (digluino and disquark) samples are generated with up to two extra  
1737 partons in the matrix element using MG5\_aMC@NLO 2.2.2 event generator [Alwall:2014hca] interfaced to PYTHIA 8.186 [Sjostrand:2014zea]. The  
1738 nominal cross-section is taken from an envelope of cross-section predictions using  
1739 different PDF sets and factorization and renormalization scales, as described in  
1740 Ref. [Kramer:2012bx], considering only light-flavour quarks ( $u, d, s, c$ ). For the  
1741 light-flavour squarks (gluinos) in case of gluino- (squark-) pair production, cross-  
1742 sections are evaluated assuming masses of 450 TeV. The free parameters are  $m_{\tilde{\chi}_1^0}$  and  
1743

1744  $m_{\tilde{g}}$  ( $m_{\tilde{s}}$ ) for gluino-pair (squark-pair) production models.

1745 we have a **grid** of these signal models samples **explain** Boson ( $W, Z, \gamma$ ) plus jet events are simulated using different SHERPA generators,  
1746 with COMIX and OPENLOOPS matrix-element generators[comix, openloops, 121].

1747 Photons are required to have transverse momentum of  $> 35$  GeV. Importantly, the  $W(Z)$ +jet events are calculated at NLO while the the  $\gamma$ +jet events are calculated  
1748 at LO. The  $W/Z +$  jets events are normalized to their NNLO cross-sections

1750 **Catani:2009sm**. The  $\gamma$ +jets LO cross-section is taken directly from SHERPA; we  
1751 **THISSSSSS** will apply a correction factor to be described later.

1752 The various  $t\bar{t}$  and single-top processes[122] are generated using two versions of

1753 POWHEG-Box [[powheg-box](#), [122](#)]. These are calculated at NLO and normalized  
1754 to various orders ranging from NLO to NNLO+NNLL in the different processes,  
1755 which can be seen in [8.1](#)[[Czakon:2013goa](#), [Czakon:2011xx](#), [Aliev:2010zk](#),  
1756 [Kant:2014oha](#), [Kidonakis:2010ux](#), [Kidonakis:2011wy](#)].

1757 Diboson processes ( $WW$ ,  $WZ$ ,  $ZZ$ ) [[123](#)] are simulated using the SHERPA 2.1.1  
1758 generator. For processes with four charged leptons ( $4\ell$ ), three charged leptons and  
1759 a neutrino ( $3\ell+1\nu$ ) or two charged leptons and two neutrinos ( $2\ell+2\nu$ ), the matrix  
1760 elements contain all diagrams with four electroweak vertices, and are calculated for  
1761 up to one ( $4\ell$ ,  $2\ell+2\nu$ ) or no partons ( $3\ell+1\nu$ ) at NLO and up to three partons at LO  
1762 using the COMIX and OPENLOOPS matrix-element generators, and merged with the  
1763 SHERPA parton shower using the ME+PS@NLO prescription. For processes in which  
1764 one of the bosons decays hadronically and the other leptonically, matrix elements  
1765 are calculated for up to one ( $ZZ$ ) or no ( $WW$ ,  $WZ$ ) additional partons at NLO  
1766 and for up to three additional partons at LO using the COMIX and OPENLOOPS  
1767 matrix-element generators, and merged with the SHERPA parton shower using the  
1768 ME+PS@NLO prescription. In all cases, the CT10 PDF set is used in conjunction  
1769 with a dedicated parton-shower tuning developed by the authors of SHERPA. The  
1770 generator cross-sections are used in this case.

1771 The multi-jet background is generated with PYTHIA 8.186 using the A14  
1772 underlying-event tune and the NNPDF2.3LO parton distribution functions.

1773 A summary of the SM background processes together with the MC generators,  
1774 cross-section calculation orders in  $\alpha_s$ , PDFs, parton shower and tunes used is given  
1775 in Table [8.1](#).

Physics process	Generator	Cross-section normalization	PDF set	Parton shower	Tune
$W(\rightarrow \ell\nu) + \text{jets}$	SHERPA 2.2.0	NNLO	NNPDF3.0NNLO	SHERPA	SHERPA default
$Z/\gamma^*(\rightarrow \ell\bar{\ell}) + \text{jets}$	SHERPA 2.2.0	NNLO	NNPDF3.0NNLO	SHERPA	SHERPA default
$\gamma + \text{jets}$	SHERPA 2.1.1	LO	CT10	SHERPA	SHERPA default
$t\bar{t}$	Powheg-Box v2	NNLO+NNLL	CT10	PYTHIA 6.428	PERUGIA2012
Single top ( $Wt$ -channel)	Powheg-Box v2	NNLO+NNLL	CT10	PYTHIA 6.428	PERUGIA2012
Single top ( $s$ -channel)	Powheg-Box v2	NLO	CT10	PYTHIA 6.428	PERUGIA2012
Single top ( $t$ -channel)	Powheg-Box v1	NLO	CT10f4	PYTHIA 6.428	PERUGIA2012
$t\bar{t} + W/Z/WW$	MG5_aMC@NLO 2.2.3	NLO	NNPDF2.3LO	PYTHIA 8.186	A14
$WW, WZ, ZZ$	SHERPA 2.1.1	NLO	CT10	SHERPA	SHERPA default
Multi-jet	PYTHIA 8.186	LO	NNPDF2.3LO	PYTHIA 8.186	A14

Table 8.1: The Standard Model background Monte Carlo simulation samples used in this thesis. The generators, the order in  $\alpha_s$  of cross-section calculations used for yield normalization, PDF sets, parton showers and tunes used for the underlying event are shown.

1776 For all SM background samples the response of the detector to particles is  
 1777 modelled with a full ATLAS detector simulation [**:2010wqa**] based on GEANT4  
 1778 [**Agostinelli:2002hh**]. Signal samples are prepared using a fast simulation based on  
 1779 a parameterization of the performance of the ATLAS electromagnetic and hadronic  
 1780 calorimeters [**ATLAS:2010bfa**] and on GEANT4 elsewhere.

1781 All simulated events are overlaid with multiple  $pp$  collisions simulated with  
 1782 the soft QCD processes of PYTHIA 8.186 using the A2 tune [**A14tune**] and the  
 1783 MSTW2008LO parton distribution functions [**Martin:2009iq**]. The simulations are  
 1784 reweighted to match the distribution of the mean number of interactions observed in  
 1785 data.

1786 **8.2 Event selection**

1787 This section describes the selection of events. We begin by describing the *preselection*,  
1788 which is used to remove problematic events and reduce the dataset to a manageable  
1789 size. We then describe the signal region strategy, and present the signal regions used  
1790 in the analysis.

1791 **Preselection**

1792 The preselection is used to reduce the dataset to that of interest in this thesis. The  
1793 table containing the preselection cuts is shown in 8.2. This selection is also used for  
1794 the samples used for background estimation, except for the lepton veto.

1795 The cuts [1] and [4] are a set of cleaning cuts to remove problematic events.  
1796 The *Good Runs List* is a centrally-maintained list of data runs which have been  
1797 determined to be “good for physics”. This determination is made by analysis of the  
1798 various subdetectors, and monitoring of their status. Event cleaning is used to veto  
1799 events which could be affected by noncollision background, noise bursts, or cosmic  
1800 rays.

1801 We require the lowest unprescaled  $E_T^{\text{miss}}$  trigger for the data run of interest, as  
1802 described previously, in cut [2]. The lepton veto is applied in cut [5]. These two cuts  
1803 are only used for the signal region selection.

1804 The rest of the preselection is used for the signal region and background estimation  
1805 samples. These cuts are mostly used for the reduction of the dataset to a manageable  
1806 Signal models with sensitivity to lower values of these scale variables have been ruled  
1807 out by previous searches . The final cut is on  $m_{\text{eff}}$ , which is the scalar sum of all jets [cite](#)  
1808 and  $E_T^{\text{miss}}$ . This is the final discriminating variable used in the complementary search  
1809 to this thesis, which is also presented in ??.

Cut	Description	
1	Good Runs List	Veto events with intolerable detector errors
2	Trigger	HLT_xe70 (2015), HLT_xe80_tclcw_L1XE50, or HLT_xe100_mht_L1XE50 (2016)
3	Event cleaning	Veto for noncollision background, noise bursts, and cosmic rays
4	Lepton veto	No leptons with $p_T > 10$ GeV after overlap removal
5	$E_T^{\text{miss}}$ [GeV] >	250
6	$p_T(j_1)$ [GeV] >	200
7	$p_T(j_2)$ [GeV] >	50
8	$m_{\text{eff}}$ [GeV] >	800

Table 8.2: Preselection for the various event topologies used in the analysis.

## 1810 Signal regions

1811 We define a set of signal regions using the RJR variables previously described.  
 1812 These signal regions are split into three general categories: squark pair production  
 1813 SRs, gluino pair production SRs, and compressed production SRs. Within these  
 1814 general SRs, we have a set of signal regions targetting different mass splittings of the  
 1815 sparticle and LSP.

1816 A schematic of this strategy is shown in ???. This type of plane is how most  
 1817 ( $R-$  parity conserving) SUSY searches are organized in both ATLAS and CMS. The  
 1818 horizontal axis is the mass of the sparticle considered. In the case of this thesis,  
 1819 this will the squark or gluino mass. On the horizontal axis, we place the LSP mass.  
 1820 These are the two free parameters of the simplified models considered here. Our  
 1821 search occurs in this two-parameter space. Each signal region targets some portion  
 1822 of this plane. As shown in the figure, a new iteration of a search will use a set of  
 1823 signal regions which have sensitivity just beyond those of the previous exclusions.  
 1824 The choice of how many signal regions to use to fully cover this plane is in many  
 1825 ways a matter of judgment, as it is essentially a matter of under/over-fitting to the  
 1826 signal models of interest. One signal region will obscure the different phenomena in

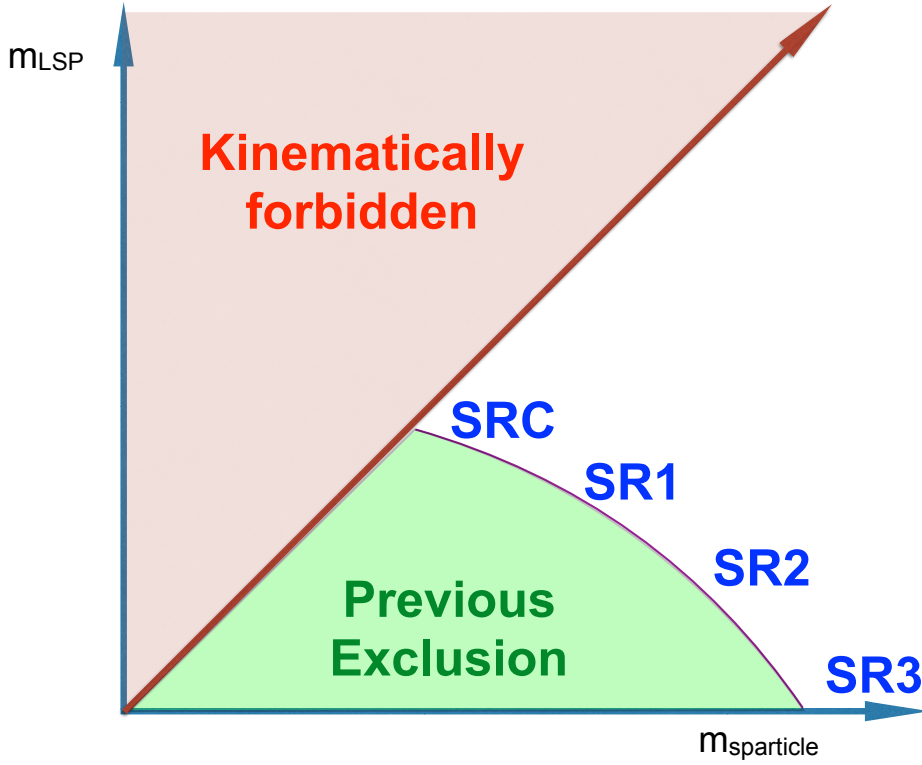


Figure 8.1: Schematic leading the development of the SUSY signal regions in this thesis. A variant of this schematic is used for most SUSY searches on ATLAS and CMS.

1827 signal events with large versus small mass splittings, leading to underfitting. Binning  
 1828 as finely as possible<sup>2</sup> leads to overfitting due to the fluctuations present in the signal  
 1829 and background events passing this selection. In this thesis, we use six squark signal  
 1830 regions, six gluino signal regions, and five compressed regions, which we describe  
 1831 below.

1832 The full table defining all signal regions is shown in 8.3. In all cases, the signal  
 1833 region selections contain a combination of scaleful and scaleless cuts. Emphasis  
 1834 on cuts on scaleful variables provide stronger sensitivity to larger mass splittings,  
 1835 while additional sensitivity to smaller mass splittings is found using stronger cuts on  
 1836 scaleless variables. One envisions walking from SR1 (with tight scaleless cuts and

---

<sup>2</sup>This can be defined as having a signal region for each simulated signal sample, which for this analysis is  $\sim 100$ .

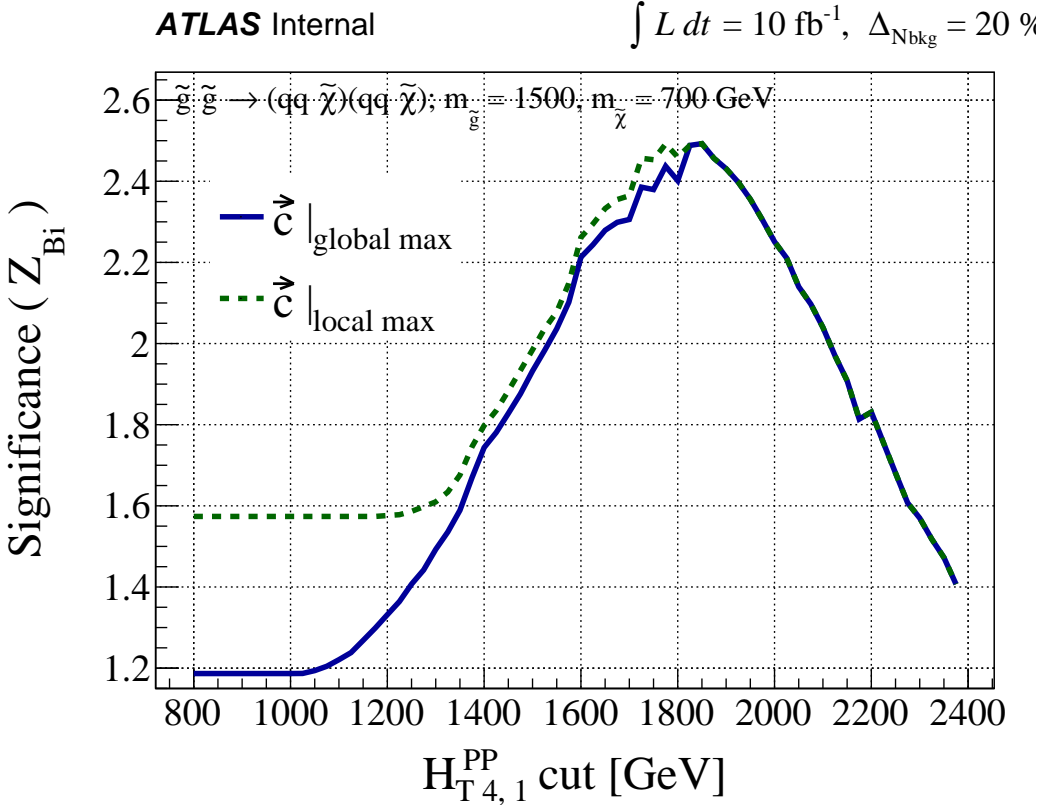


Figure 8.2: Optimization of the  $H_{T,4,1}^{PP}$  cut for a gluino signal model with  $(m_{\tilde{g}}, m_{\tilde{\chi}_1^0}) = (1500, 700)$  GeV assuming  $10 \text{ fb}^{-1}$  and an uncertainty of 20% on the background estimate.

1837 loose scaleful cuts) in 8.1 towards SR3 by loosening the scaleless cuts and tightening  
 1838 the scaleful cuts. We will see this strategy at work in each set of signal regions.

1839 We have already described the useful variables in the previous chapter. The  
 1840 question is how to choose the optimal cuts for a given set of signal models, which are  
 1841 grouped in the mass splitting space. This was done by a brute force scan over the  
 1842 cut values, using a guess of integrated luminosity with a fixed systematic uncertainty  
 1843 scenario, motivated by that from previous analyses. We choose the lowest cut value  
 1844 that maximizes the  $Z_{Bi}$ , as described in [124]. This figure of merit gives conservative  
 1845 estimates, as compared to i.e.  $S/\sqrt{B}$ . A figure showing an example of this selection  
 1846 tuning procedure is shown in 8.2.

1847 The compressed selections are split into five regions (SRC1-5), and due to the

1848 simplified nature of the compressed decay tree, has sensitivity in both the gluino  
1849 and squark planes. The compressed regions target mass splittings with  $m_{\text{sparticle}} -$   
1850  $m_{\text{LSP}} \tilde{<} 200 \text{ GeV}$ . For the compressed region,  $M_{T,S}$  is the primary scaleful variable.  
1851 We can see the general strategy of lowering increasing scale cuts while decreasing the  
1852 scaleless cuts here. SRC1 targets the most compressed scenarios, with mass splittings  
1853 of less than 25 GeV, and has the loosest  $M_{T,S}$  cut coupled with the tightest  $R_{\text{ISR}}$  and  
1854  $\Delta\phi_{\text{ISR},I}$  cuts. SRC4 and SRC5 target mass splittings of  $\sim 200$  GeV, and are coupled  
1855 with the loosest scaleless cuts on  $R_{\text{ISR}}$  and  $\Delta\phi_{\text{ISR},I}$ . We also note that SRC4 and  
1856 SRC5 have differing cuts on  $N_{\text{jet}}^V$ , since these SRs are closest to the regions we will  
1857 describe below, and can be seen as the “cross-over” where the differences between  
1858 squark and gluino production begins to become manifest.

1859 The squark regions (for noncompressed spectra) are organized into six signal  
1860 regions. These are labeled by a numeral 1-3 and letter a/b. SRs sharing a common  
1861 numeral i.e. SRS1a and SRS1b share a common set of scaleless cuts, while differing  
1862 in the main scale variable  $H_{T,2,1}^{PP}$ . The two SRs for each set of scaleless cuts, only  
1863 differing in the main scale variable, can be seen in way as providing sensitivity to a naive  
1864 range of luminosity scenarios<sup>3</sup>. As before, we see that the scaleless cuts are loosened  
1865 as we tighten the scaleful cuts, as we move across the table from SRS1a to SRS3b.  
1866 This provides strong sensitivity to signal models with intermediate mass splittings with  
1867 SRS1a to large mass splittings with SR3b.

1868 The gluino signal regions are organized entirely analogously to the squark signal  
1869 regions. There are six gluino signal regions, again labeled via a numeral 1-3 and letter  
1870 a/b. Those SRs sharing a common numeral have a common set of scaleless cuts, but  
1871 differ in their main scale variable  $H_{T,4,1}^{PP}$ . The SRs follow the strategy, with SRG1  
1872 having the loosest scaleful cut cuts coupled with the strongest scaleless cuts, and the

---

<sup>3</sup>These SRs were defined before the entire collision dataset was produced, and thus need to be robust in cases where the LHC provides significantly different than expected performance.

1873 converse being true in SRG3. As in the squark case, this strategy provides strong  
1874 expected sensitivity throughout the gluino-LSP plane.

PLOT      1874  
expected  
sensitivity  
with these  
assump-  
tions?

Targeted signal	$\tilde{s}\tilde{s}, \tilde{s} \rightarrow q\tilde{\chi}_1^0$									
Requirement	Signal Region									
	<b>RJR-S1</b>		<b>RJR-S2</b>		<b>RJR-S3</b>					
$H_{1,1}^{PP}/H_{2,1}^{PP} \geq$	0.6		0.55		0.5					
$H_{1,1}^{PP}/H_{2,1}^{PP} \leq$	0.95		0.96		0.98					
$p_{PP, z}^{lab}/(p_{PP, z}^{lab} + H_{T, 2,1}^{PP}) \leq$	0.5		0.55		0.6					
$p_{j2, T}^{PP}/H_{T, 2,1}^{PP} \geq$	0.16		0.15		0.13					
$\Delta_{QCD} >$	0.001									
	<b>RJR-S1a</b>	<b>RJR-S1b</b>	<b>RJR-S2a</b>	<b>RJR-S2b</b>	<b>RJR-S3a</b>	<b>RJR-S3b</b>				
$H_{T, 2,1}^{PP} [\text{GeV}] >$	1000	1200	1400	1600	1800	2000				
$H_{1,1}^{PP} [\text{GeV}] >$	1000		1400		1600					
Targeted signal	$\tilde{g}\tilde{g}, \tilde{g} \rightarrow q\bar{q}\tilde{\chi}_1^0$									
Requirement	Signal Region									
	<b>RJR-G1</b>		<b>RJR-G2</b>		<b>RJR-G3</b>					
$H_{1,1}^{PP}/H_{4,1}^{PP} \geq$	0.35		0.25		0.2					
$H_{T, 4,1}^{PP}/H_{4,1}^{PP} \geq$	0.8		0.75		0.65					
$p_{PP, z}^{lab}/(p_{PP, z}^{lab} + H_{T, 4,1}^{PP}) \leq$	0.5		0.55		0.6					
$\min(p_{j2, T}^{PP}/H_{T, 2,1}^{PP}) \geq$	0.12		0.1		0.08					
$\max(H_{1,0}^{Pi}/H_{2,0}^{Pi}) \leq$	0.95		0.97		0.98					
$ \frac{2}{3}\Delta\phi_{V,P}^{PP} - \frac{1}{3}\cos\theta_p  \leq$	0.5		-							
$\Delta_{QCD} >$	0									
	<b>RJR-G1a</b>	<b>RJR-G1b</b>	<b>RJR-G2a</b>	<b>RJR-G2b</b>	<b>RJR-G3a</b>	<b>RJR-G3b</b>				
$H_{T, 4,1}^{PP} [\text{GeV}] >$	1000	1200	1500	1900	2300	2800				
$H_{1,1}^{PP} [\text{GeV}] >$	600		800		900					
Targeted signal	compressed spectra in $\tilde{s}\tilde{s}$ ( $\tilde{s} \rightarrow q\tilde{\chi}_1^0$ ); $\tilde{g}\tilde{g}$ ( $\tilde{g} \rightarrow q\bar{q}\tilde{\chi}_1^0$ )									
Requirement	Signal Region									
	<b>RJR-C1</b>	<b>RJR-C2</b>	<b>RJR-C3</b>	<b>RJR-C4</b>	<b>RJR-C5</b>					
$R_{ISR} \geq$	0.9	0.85	0.8	0.75	0.70					
$\Delta\phi_{ISR, I} \geq$	3.1	3.07	2.95	2.95	2.95					
$\Delta\phi(\text{jet}_{1,2}, \mathbf{E}_T^{\text{miss}})_{\text{min}}$	-	-	-	0.4	0.4					
$M_{TS} [\text{GeV}] \geq$	100	100	200	500	500					
$p_{TS}^{CM} [\text{GeV}] \geq$	800	800	600	600	600					
$N_{jet}^V \geq$	1	1	2	2	3					

Table 8.3: Selection criteria and targeted signal model used to define signal regions in the RJR-based search, indicated by the prefix ‘RJR’. Each SR is labelled with the targeted SUSY particle or the targeted region of parameter space, such that ‘S’, ‘G’ and ‘C’ denote regions searching for squark-, gluino-pair production, or compressed spectra, respectively.

## 1875 Scale variable distributions in the signal regions

1876 In ??, we can see the distributions of the last scale cut used for each signal region.

1877 These distributions include scale factors derived via the fitting procedure which are  
1878 applied to the Standard Model background, which we will describe later in this  
1879 chapter. These scale factors are all  $\sim 1$ . The systematic uncertainties, shown in  
1880 the banded stripe, are also described later in this section. Each plot shows the  
1881 distribution from a signal model which is targeted by the given signal region.

1882 These distributions have all cuts applied except for the cut on this scale variable,  
1883 which allows us to see the additional discrimination provided by the given variable.

1884 Since signal regions with the same numeral have identical cuts on all cuts other than  
1885 the main scale variable, we show (a) and (b) on the same figure. The left-most (right-  
1886 most) arrow shown is the location of the a (b) cut applied in the analysis. We call  
1887 these plots  $N - 1$  plots, where  $N$  refers to the number of cuts applied in the analysis.

1888 The full set of  $N - 1$  plots in the signal regions for the other variables used in the  
1889 analysis are shown in 9.5. We can see that for the signal models targeted by each  
1890 signal region, each cut provides unique discrimination against the Standard Model  
1891 backgrounds.

captions for  
these figures

## 1893 8.3 Background estimation

1894 We describe here the method of background estimation. In this thesis, we detail what  
1895 is colloquially called a “cut-and-count” analysis. This is in contrast to a “shape fit”  
1896 analysis, where one needs to consider the details of the variable distribution shapes.  
1897 Instead, we must ensure the overall normalization of the Standard Model backgrounds  
1898 are correct in the regions of phase space considered in the analysis. In order to do  
1899 this, we define a set of *control regions* which are free of SUSY contamination based

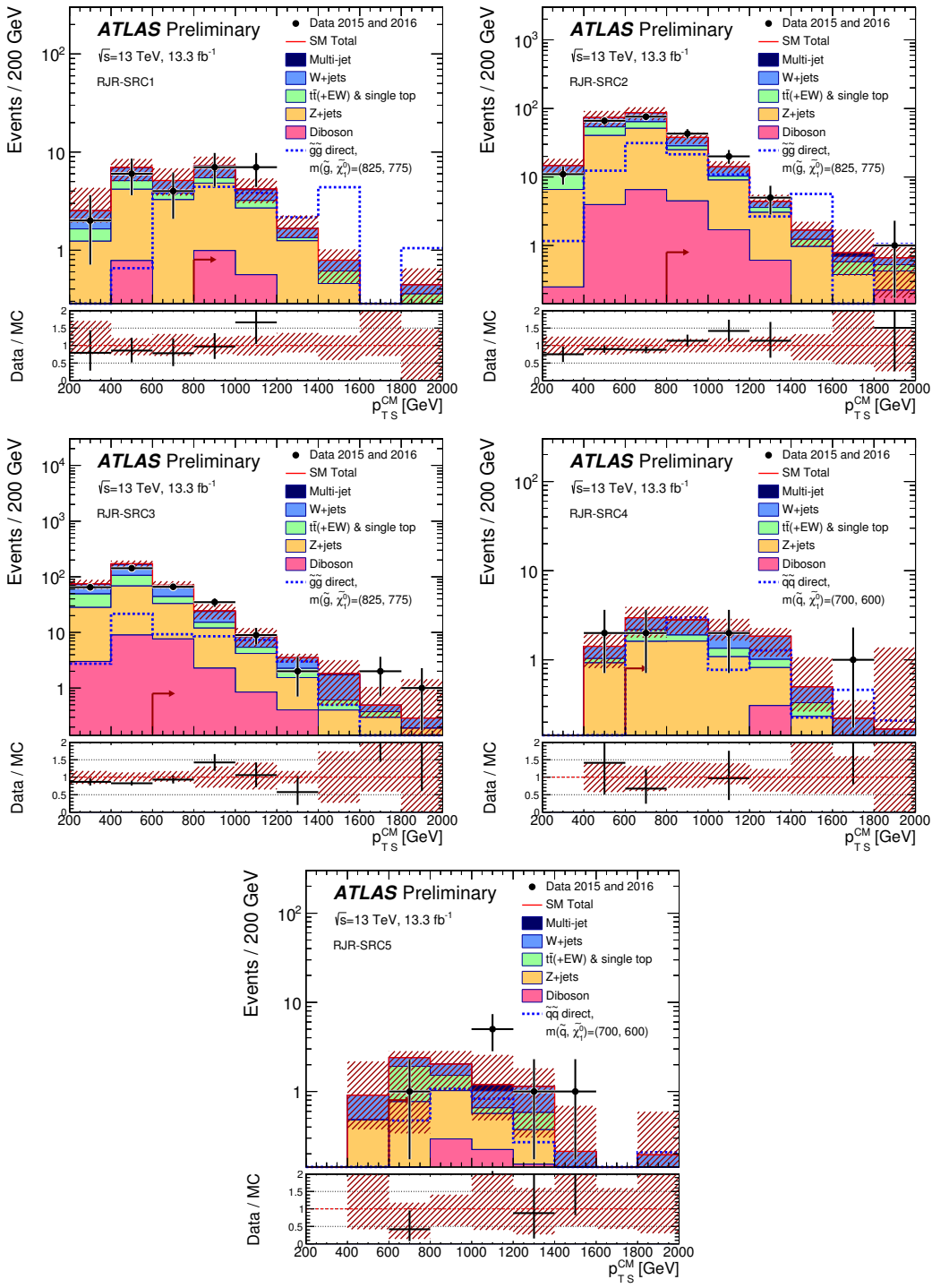


Figure 8.3

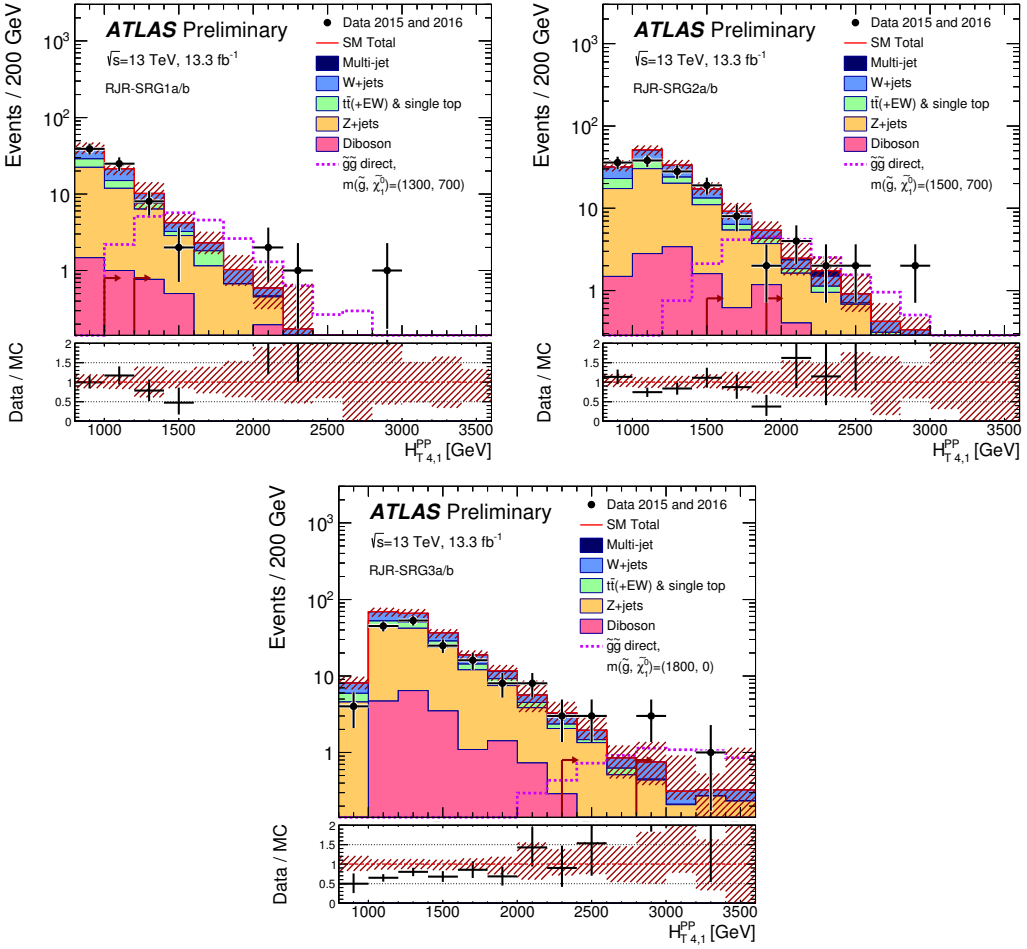


Figure 8.4

1900 on the previously excluded analysis. We compare the number of events present in the  
 1901 control regions in simulation with that in data to define a *transfer factor* (TF). We  
 1902 extrapolate the number of expected events from each background using this transfer  
 1903 factor to translate from the , which provides our final estimate of the SM background  
 1904 in the various signal regions.

More precisely, for a given signal region, we are attempting to estimate the value  
 $N_{SR}^{data}$  for a given background. This value is estimated using the following equation:

$$N_{SR}^{data,est} = N_{CR}^{data,obs} \times TF \equiv N_{CR}^{data,obs} \times \left( \frac{N_{SR}^{MC}}{N_{CR}^{MC}} \right) \quad (8.1)$$

1905 where the transfer factor TF is taken directly from MC. The two ingredients to our

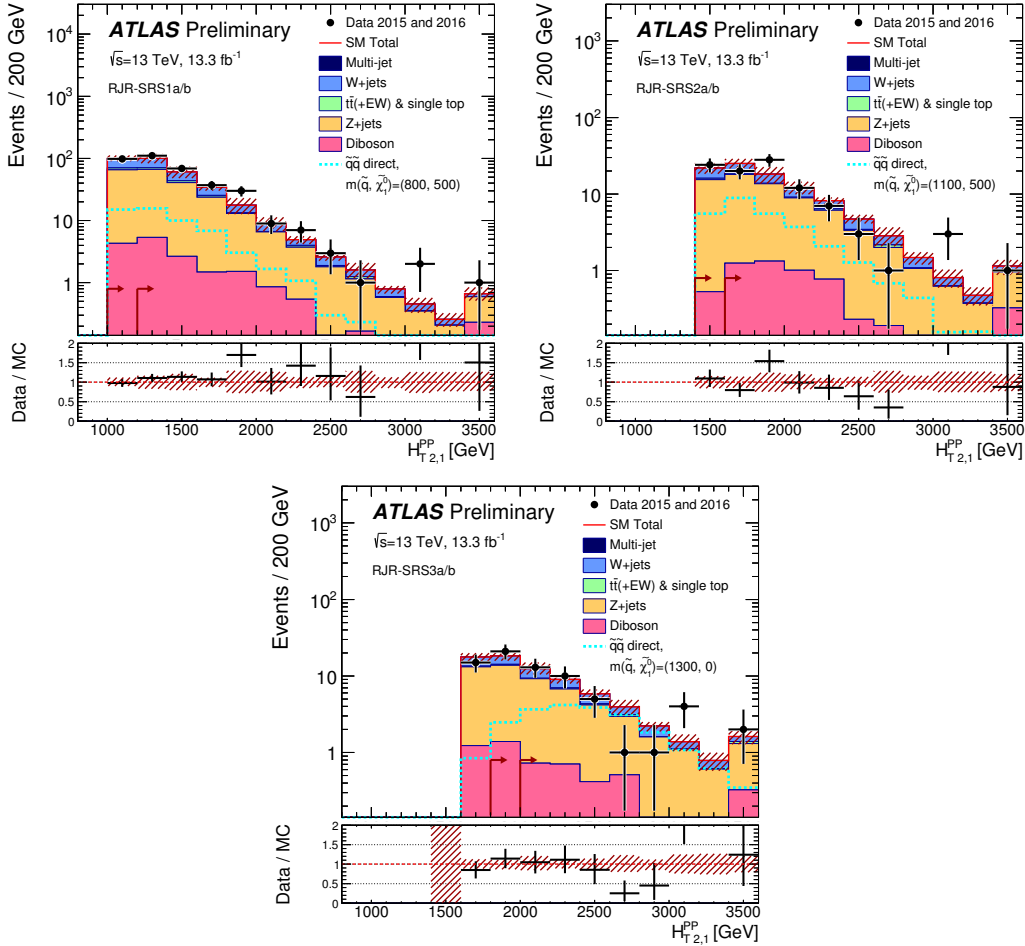


Figure 8.5

1906 estimation of  $N_{\text{SR}}^{\text{data,obs}}$  is thus  $N_{\text{CR}}^{\text{data,obs}}$  and the transfer factor taken from MC. The  
 1907 CR definitions are motivated and designed according to two (generally competing)  
 1908 requirements:

- 1909 1. Statistical uncertainties due to low CR statistics  
 1910 2. Systematic uncertainties related to the extrapolation from the CR to the SR.

1911 This motivates the desire to make the control regions as similar as possible to  
 1912 the signal regions without risking signal contamination and while ensuring high  
 1913 purity in the targeted SM background.

1914 In order to validate the transfer factors obtained from MC, we also develop a series

1915 of *validation regions* (VRs). These regions are generally designed to be “in between”  
1916 the control region and signal region selections in phase space, and thus provide a  
1917 check on the extrapolation from the control regions into the signal regions. Despite  
1918 their closeness in phase space to the signal regions, they are also designed to have  
1919 low signal contamination.

1920 In practice, we perform this estimation procedure simultaneously across all control  
1921 regions; we describe this later. We only note this here since in principle, we can apply  
1922 Eq.8.1 to measure the contamination of backgrounds within control regions as well.  
1923 We next describe the control region selection for the major SM backgrounds for the  
1924 analysis.

## 1925 **Control and Validation Regions**

1926 As was hinted at in the discussion of Monte Carlo generators, the primary back-  
1927 grounds of note in this analysis are  $Z + \text{jets}$ ,  $W + \text{jets}$ ,  $t\bar{t}$ , and QCD events. We describe  
1928 the strategy to estimate these various backgrounds here. A summary table is shown  
1929 in ??.

1930 Events with a  $Z$  boson decaying to neutrinos in association with jets are the  
1931 primary irreducible background in the analysis. These events have true  $E_T^{\text{miss}}$  from  
1932 the decaying neutrinos, and can have significant  
1933 CRT,CRW,CRY,CRQ

## 1934 **R Z/ $\gamma$ method**

## 1935 **Systematic Uncertainties**

1936

## Chapter 9

---

1937

### *Title of Chapter 1*

1938 Here you can write some introductory remarks about your chapter. I like to give each

1939 sentence its own line.

1940 When you need a new paragraph, just skip an extra line.

### **9.1 Statistical Analysis**

1942 maybe to be moved to an appendix

### **9.2 Signal Region distributions**

### **9.3 Pull Plots**

### **9.4 Exclusion plots**



---

1946

## *Conclusion*

1947 Here you can write some introductory remarks about your chapter. I like to give each  
1948 sentence its own line.

1949 When you need a new paragraph, just skip an extra line.

1950 **9.5 New Section**

1951 By using the asterisk to start a new section, I keep the section from appearing in the  
1952 table of contents. If you want your sections to be numbered and to appear in the  
1953 table of contents, remove the asterisk.



---

1954

## Bibliography

- 1955 [1] O. Perdereau, *Planck 2015 cosmological results*,  
1956 [AIP Conf. Proc. \*\*1743\*\* \(2016\) p. 050014](#).
- 1957 [2] N. Aghanim et al.,  
1958 *Planck 2016 intermediate results. LI. Features in the cosmic microwave*  
1959 *background temperature power spectrum and shifts in cosmological parameters*  
1960 (2016), arXiv: [1608.02487 \[astro-ph.CO\]](#).
- 1961 [3] J. S. Schwinger,  
1962 *On Quantum electrodynamics and the magnetic moment of the electron*,  
1963 [Phys. Rev. \*\*73\*\* \(1948\) p. 416](#).
- 1964 [4] S. Laporta and E. Remiddi,  
1965 *The Analytical value of the electron (g-2) at order alpha\*\*3 in QED*,  
1966 [Phys. Lett. \*\*B379\*\* \(1996\) p. 283](#), arXiv: [hep-ph/9602417 \[hep-ph\]](#).
- 1967 [5] S. Schael et al., *Precision electroweak measurements on the Z resonance*,  
1968 [Phys. Rept. \*\*427\*\* \(2006\) p. 257](#), arXiv: [hep-ex/0509008 \[hep-ex\]](#).
- 1969 [6] S. L. Glashow, *Partial Symmetries of Weak Interactions*,  
1970 [Nucl. Phys. \*\*22\*\* \(1961\) p. 579](#).
- 1971 [7] S. Weinberg, *A Model of Leptons*, [Phys. Rev. Lett. \*\*19\*\* \(1967\) p. 1264](#).
- 1972 [8] A. Salam, *Weak and Electromagnetic Interactions*,  
1973 [Conf. Proc. \*\*C680519\*\* \(1968\) p. 367](#).
- 1974 [9] M. Gell-Mann, *A Schematic Model of Baryons and Mesons*,  
1975 [Phys. Lett. \*\*8\*\* \(1964\) p. 214](#).
- 1976 [10] G. Zweig, “An SU(3) model for strong interaction symmetry and its  
1977 breaking. Version 2,” *DEVELOPMENTS IN THE QUARK THEORY OF*  
1978 *HADRONS. VOL. 1. 1964 - 1978*, ed. by D. Lichtenberg and S. P. Rosen,  
1979 1964 p. 22,  
1980 URL: <http://inspirehep.net/record/4674/files/cern-th-412.pdf>.

- 1981 [11] S. Weinberg, *Implications of Dynamical Symmetry Breaking*,  
 1982 Phys. Rev. **D13** (1976) p. 974.
- 1983 [12] S. Weinberg, *Implications of Dynamical Symmetry Breaking: An Addendum*,  
 1984 Phys. Rev. **D19** (1979) p. 1277.
- 1985 [13] E. Gildener, *Gauge Symmetry Hierarchies*, Phys. Rev. **D14** (1976) p. 1667.
- 1986 [14] L. Susskind, *Dynamics of Spontaneous Symmetry Breaking in the*  
 1987 *Weinberg-Salam Theory*, Phys. Rev. **D20** (1979) p. 2619.
- 1988 [15] S. P. Martin, “A Supersymmetry Primer,” 1997,  
 1989 eprint: [arXiv:hep-ph/9709356](https://arxiv.org/abs/hep-ph/9709356).
- 1990 [16] V. C. Rubin and W. K. Ford Jr., *Rotation of the Andromeda Nebula from a*  
 1991 *Spectroscopic Survey of Emission Regions*, Astrophys. J. **159** (1970) p. 379.
- 1992 [17] M. S. Roberts and R. N. Whitehurst,  
 1993 “*The rotation curve and geometry of M31 at large galactocentric distances*,  
 1994 Astrophys. J. **201** (1970) p. 327.
- 1995 [18] V. C. Rubin, N. Thonnard, and W. K. Ford Jr.,  
 1996 *Rotational properties of 21 SC galaxies with a large range of luminosities and*  
 1997 *radii, from NGC 4605 /R = 4kpc/ to UGC 2885 /R = 122 kpc/*,  
 1998 Astrophys. J. **238** (1980) p. 471.
- 1999 [19] V. C. Rubin et al., *Rotation velocities of 16 SA galaxies and a comparison of*  
 2000 *Sa, Sb, and SC rotation properties*, Astrophys. J. **289** (1985) p. 81.
- 2001 [20] A. Bosma,  
 2002 *21-cm line studies of spiral galaxies. 2. The distribution and kinematics of*  
 2003 *neutral hydrogen in spiral galaxies of various morphological types.*,  
 2004 Astron. J. **86** (1981) p. 1825.
- 2005 [21] M. Persic, P. Salucci, and F. Stel, *The Universal rotation curve of spiral*  
 2006 *galaxies: 1. The Dark matter connection*,  
 2007 Mon. Not. Roy. Astron. Soc. **281** (1996) p. 27,  
 2008 arXiv: [astro-ph/9506004](https://arxiv.org/abs/astro-ph/9506004) [astro-ph].
- 2009 [22] M. Lisanti, “Lectures on Dark Matter Physics,” 2016,  
 2010 eprint: [arXiv:1603.03797](https://arxiv.org/abs/1603.03797).
- 2011 [23] H. Miyazawa, *Baryon Number Changing Currents*,  
 2012 Prog. Theor. Phys. **36** (1966) p. 1266.

- 2013 [24] J.-L. Gervais and B. Sakita, *Generalizations of dual models*,  
 2014 *Nucl. Phys.* **B34** (1971) p. 477.
- 2015 [25] J.-L. Gervais and B. Sakita,  
 2016 *Field Theory Interpretation of Supergauges in Dual Models*,  
 2017 *Nucl. Phys.* **B34** (1971) p. 632.
- 2018 [26] Yu. A. Golfand and E. P. Likhtman, *Extension of the Algebra of Poincare  
 Group Generators and Violation of p Invariance*,  
 2019 JETP Lett. **13** (1971) p. 323, [Pisma Zh. Eksp. Teor. Fiz.13,452(1971)].
- 2021 [27] A. Neveu and J. H. Schwarz, *Factorizable dual model of pions*,  
 2022 *Nucl. Phys.* **B31** (1971) p. 86.
- 2023 [28] A. Neveu and J. H. Schwarz, *Quark Model of Dual Pions*,  
 2024 *Phys. Rev.* **D4** (1971) p. 1109.
- 2025 [29] D. V. Volkov and V. P. Akulov, *Is the Neutrino a Goldstone Particle?*  
 2026 *Phys. Lett.* **B46** (1973) p. 109.
- 2027 [30] J. Wess and B. Zumino,  
 2028 *A Lagrangian Model Invariant Under Supergauge Transformations*,  
 2029 *Phys. Lett.* **B49** (1974) p. 52.
- 2030 [31] A. Salam and J. A. Strathdee, *Supersymmetry and Nonabelian Gauges*,  
 2031 *Phys. Lett.* **B51** (1974) p. 353.
- 2032 [32] S. Ferrara, J. Wess, and B. Zumino, *Supergauge Multiplets and Superfields*,  
 2033 *Phys. Lett.* **B51** (1974) p. 239.
- 2034 [33] J. Wess and B. Zumino, *Supergauge Transformations in Four-Dimensions*,  
 2035 *Nucl. Phys.* **B70** (1974) p. 39.
- 2036 [34] J. D. Lykken, “Introduction to supersymmetry,” *Fields, strings and duality.  
 Proceedings, Summer School, Theoretical Advanced Study Institute in  
 Elementary Particle Physics, TASI’96, Boulder, USA, June 2-28, 1996*, 1996  
 2037 p. 85, arXiv: [hep-th/9612114](https://arxiv.org/abs/hep-th/9612114) [hep-th],  
 2038 URL: [http://lss.fnal.gov/cgi-bin/find\\_paper.pl?pub=96-445-T](http://lss.fnal.gov/cgi-bin/find_paper.pl?pub=96-445-T).
- 2041 [35] A. Kobakhidze, “Intro to SUSY,” 2016, URL: <https://indico.cern.ch/event/443176/page/5225-pre-susy-programme>.
- 2043 [36] G. R. Farrar and P. Fayet, *Phenomenology of the Production, Decay, and  
 2044 Detection of New Hadronic States Associated with Supersymmetry*,  
 2045 *Phys. Lett.* **B76** (1978) p. 575.

- 2046 [37] ATLAS Collaboration,  
 2047 *Search for the electroweak production of supersymmetric particles in*  
 2048  *$\sqrt{s} = 8 \text{ TeV}$  pp collisions with the ATLAS detector,*  
 2049 *Phys. Rev. D* **93** (2016) p. 052002, arXiv: [1509.07152 \[hep-ex\]](#).
- 2050 [38] ATLAS Collaboration, *Summary of the searches for squarks and gluinos*  
 2051 *using  $\sqrt{s} = 8 \text{ TeV}$  pp collisions with the ATLAS experiment at the LHC,*  
 2052 *JHEP* **10** (2015) p. 054, arXiv: [1507.05525 \[hep-ex\]](#).
- 2053 [39] ATLAS Collaboration, *ATLAS Run 1 searches for direct pair production of*  
 2054 *third-generation squarks at the Large Hadron Collider,*  
 2055 *Eur. Phys. J. C* **75** (2015) p. 510, arXiv: [1506.08616 \[hep-ex\]](#).
- 2056 [40] CMS Collaboration, *Search for supersymmetry with razor variables in pp*  
 2057 *collisions at  $\sqrt{s} = 7 \text{ TeV}$ , Phys. Rev. D* **90** (2014) p. 112001,  
 2058 arXiv: [1405.3961 \[hep-ex\]](#).
- 2059 [41] CMS Collaboration, *Inclusive search for supersymmetry using razor variables*  
 2060 *in pp collisions at  $\sqrt{s} = 7 \text{ TeV}$ , Phys. Rev. Lett.* **111** (2013) p. 081802,  
 2061 arXiv: [1212.6961 \[hep-ex\]](#).
- 2062 [42] CMS Collaboration, *Search for Supersymmetry in pp Collisions at 7 TeV in*  
 2063 *Events with Jets and Missing Transverse Energy,*  
 2064 *Phys. Lett. B* **698** (2011) p. 196, arXiv: [1101.1628 \[hep-ex\]](#).
- 2065 [43] CMS Collaboration, *Search for Supersymmetry at the LHC in Events with*  
 2066 *Jets and Missing Transverse Energy, Phys. Rev. Lett.* **107** (2011) p. 221804,  
 2067 arXiv: [1109.2352 \[hep-ex\]](#).
- 2068 [44] CMS Collaboration, *Search for supersymmetry in hadronic final states using*  
 2069  *$M_{T2}$  in pp collisions at  $\sqrt{s} = 7 \text{ TeV}$ , JHEP* **10** (2012) p. 018,  
 2070 arXiv: [1207.1798 \[hep-ex\]](#).
- 2071 [45] CMS Collaboration, *Searches for supersymmetry using the  $M_{T2}$  variable in*  
 2072 *hadronic events produced in pp collisions at 8 TeV, JHEP* **05** (2015) p. 078,  
 2073 arXiv: [1502.04358 \[hep-ex\]](#).
- 2074 [46] CMS Collaboration, *Search for new physics with the  $M_{T2}$  variable in all-jets*  
 2075 *final states produced in pp collisions at  $\sqrt{s} = 13 \text{ TeV}$ , JHEP* (2016),  
 2076 arXiv: [1603.04053 \[hep-ex\]](#).
- 2077 [47] ATLAS Collaboration, *Multi-channel search for squarks and gluinos in*  
 2078  *$\sqrt{s} = 7 \text{ TeV}$  pp collisions with the ATLAS detector at the LHC,*  
 2079 *Eur. Phys. J. C* **73** (2013) p. 2362, arXiv: [1212.6149 \[hep-ex\]](#).

- 2080 [48] Y. Grossman, “Introduction to the SM,” 2016, URL: <https://indico.fnal.gov/sessionDisplay.py?sessionId=3&confId=11505#20160811>.
- 2081
- 2082 [49] W Buchmuller and C Ludeling, *Field Theory and Standard Model* (Sept. 2006) p. 70, URL: <https://cds.cern.ch/record/984122>.
- 2083
- 2084 [50] P. W. Higgs, *Broken Symmetries and the Masses of Gauge Bosons*, Phys. Rev. Lett. **13** (1964) p. 508.
- 2085
- 2086 [51] ATLAS Collaboration, *Observation of a new particle in the search for the Standard Model Higgs boson with the ATLAS detector at the LHC*, Phys. Lett. B **716** (2012) p. 1, arXiv: [1207.7214 \[hep-ex\]](https://arxiv.org/abs/1207.7214).
- 2087
- 2088
- 2089 [52] CMS Collaboration, *Observation of a new boson at a mass of 125 GeV with the CMS experiment at the LHC*, Phys. Lett. B **716** (2012) p. 30, arXiv: [1207.7235 \[hep-ex\]](https://arxiv.org/abs/1207.7235).
- 2090
- 2091
- 2092 [53] A. Chodos et al., *A New Extended Model of Hadrons*, Phys. Rev. **D9** (1974) p. 3471.
- 2093
- 2094 [54] A. Chodos et al., *Baryon Structure in the Bag Theory*, Phys. Rev. **D10** (1974) p. 2599.
- 2095
- 2096 [55] J. C. Collins, D. E. Soper, and G. F. Sterman, *Factorization of Hard Processes in QCD*, Adv. Ser. Direct. High Energy Phys. **5** (1989) p. 1, arXiv: [hep-ph/0409313 \[hep-ph\]](https://arxiv.org/abs/hep-ph/0409313).
- 2097
- 2098
- 2099
- 2100 [56] K. A. Olive et al., *Review of Particle Physics*, Chin. Phys. **C38** (2014) p. 090001.
- 2101
- 2102 [57] N. Cabibbo, *Unitary Symmetry and Leptonic Decays*, Phys. Rev. Lett. **10** (1963) p. 531, [[648\(1963\)](#)].
- 2103
- 2104 [58] M. Kobayashi and T. Maskawa, *CP Violation in the Renormalizable Theory of Weak Interaction*, Prog. Theor. Phys. **49** (1973) p. 652.
- 2105
- 2106
- 2107 [59] W. F. L. Hollik, *Radiative Corrections in the Standard Model and their Role for Precision Tests of the Electroweak Theory*, Fortsch. Phys. **38** (1990) p. 165.
- 2108
- 2109
- 2110 [60] D. Yu. Bardin et al., *ELECTROWEAK RADIATIVE CORRECTIONS TO DEEP INELASTIC*
- 2111

- 2112            *SCATTERING AT HERA! CHARGED CURRENT SCATTERING,*  
 2113            *Z. Phys. C***44** (1989) p. 149.
- 2114 [61] D. C. Kennedy et al.,  
 2115            *Electroweak Cross-Sections and Asymmetries at the Z0,*  
 2116            *Nucl. Phys. B***321** (1989) p. 83.
- 2117 [62] A. Sirlin, *Radiative Corrections in the SU(2)-L x U(1) Theory: A Simple*  
 2118            *Renormalization Framework*, *Phys. Rev. D***22** (1980) p. 971.
- 2119 [63] S. Fanchiotti, B. A. Kniehl, and A. Sirlin,  
 2120            *Incorporation of QCD effects in basic corrections of the electroweak theory*,  
 2121            *Phys. Rev. D***48** (1993) p. 307, arXiv: [hep-ph/9212285 \[hep-ph\]](#).
- 2122 [64] C. Quigg, “Cosmic Neutrinos,” *Proceedings, 35th SLAC Summer Institute on*  
 2123            *Particle Physics: Dark matter: From the cosmos to the Laboratory (SSI*  
 2124            *2007): Menlo Park, California, July 30- August 10, 2007*, 2008,  
 2125            arXiv: [0802.0013 \[hep-ph\]](#),  
 2126            URL: [http://lss.fnal.gov/cgi-bin/find\\_paper.pl?conf-07-417](http://lss.fnal.gov/cgi-bin/find_paper.pl?conf-07-417).
- 2127 [65] S. R. Coleman and J. Mandula, *All Possible Symmetries of the S Matrix*,  
 2128            *Phys. Rev. 159* (1967) p. 1251.
- 2129 [66] R. Haag, J. T. Lopuszanski, and M. Sohnius,  
 2130            *All Possible Generators of Supersymmetries of the s Matrix*,  
 2131            *Nucl. Phys. B***88** (1975) p. 257.
- 2132 [67] A. Salam and J. A. Strathdee, *On Superfields and Fermi-Bose Symmetry*,  
 2133            *Phys. Rev. D***11** (1975) p. 1521.
- 2134 [68] S. Dimopoulos and H. Georgi, *Softly Broken Supersymmetry and SU(5)*,  
 2135            *Nucl. Phys. B***193** (1981) p. 150.
- 2136 [69] S. Dimopoulos, S. Raby, and F. Wilczek,  
 2137            *Supersymmetry and the Scale of Unification*, *Phys. Rev. D***24** (1981) p. 1681.
- 2138 [70] L. E. Ibanez and G. G. Ross,  
 2139            *Low-Energy Predictions in Supersymmetric Grand Unified Theories*,  
 2140            *Phys. Lett. B***105** (1981) p. 439.
- 2141 [71] W. J. Marciano and G. Senjanovic,  
 2142            *Predictions of Supersymmetric Grand Unified Theories*,  
 2143            *Phys. Rev. D***25** (1982) p. 3092.

- 2144 [72] L. Girardello and M. T. Grisaru, *Soft Breaking of Supersymmetry*,  
 2145 *Nucl. Phys.* **B194** (1982) p. 65.
- 2146 [73] D. J. H. Chung et al.,  
 2147 *The Soft supersymmetry breaking Lagrangian: Theory and applications*,  
 2148 *Phys. Rept.* **407** (2005) p. 1, arXiv: [hep-ph/0312378 \[hep-ph\]](#).
- 2149 [74] J. Hisano et al., *Lepton flavor violation in the supersymmetric standard*  
 2150 *model with seesaw induced neutrino masses*, *Phys. Lett.* **B357** (1995) p. 579,  
 2151 arXiv: [hep-ph/9501407 \[hep-ph\]](#).
- 2152 [75] F. Gabbiani et al., *A Complete analysis of FCNC and CP constraints in*  
 2153 *general SUSY extensions of the standard model*,  
 2154 *Nucl. Phys.* **B477** (1996) p. 321, arXiv: [hep-ph/9604387 \[hep-ph\]](#).
- 2155 [76] F. Gabbiani and A. Masiero,  
 2156 *FCNC in Generalized Supersymmetric Theories*,  
 2157 *Nucl. Phys.* **B322** (1989) p. 235.
- 2158 [77] J. S. Hagelin, S. Kelley, and T. Tanaka, *Supersymmetric flavor changing*  
 2159 *neutral currents: Exact amplitudes and phenomenological analysis*,  
 2160 *Nucl. Phys.* **B415** (1994) p. 293.
- 2161 [78] J. S. Hagelin, S. Kelley, and V. Ziegler, *Using gauge coupling unification and*  
 2162 *proton decay to test minimal supersymmetric SU(5)*,  
 2163 *Phys. Lett.* **B342** (1995) p. 145, arXiv: [hep-ph/9406366 \[hep-ph\]](#).
- 2164 [79] D. Choudhury et al.,  
 2165 *Constraints on nonuniversal soft terms from flavor changing neutral currents*,  
 2166 *Phys. Lett.* **B342** (1995) p. 180, arXiv: [hep-ph/9408275 \[hep-ph\]](#).
- 2167 [80] R. Barbieri and L. J. Hall, *Signals for supersymmetric unification*,  
 2168 *Phys. Lett.* **B338** (1994) p. 212, arXiv: [hep-ph/9408406 \[hep-ph\]](#).
- 2169 [81] B. de Carlos, J. A. Casas, and J. M. Moreno,  
 2170 *Constraints on supersymmetric theories from mu —> e gamma*,  
 2171 *Phys. Rev.* **D53** (1996) p. 6398, arXiv: [hep-ph/9507377 \[hep-ph\]](#).
- 2172 [82] J. A. Casas and S. Dimopoulos,  
 2173 *Stability bounds on flavor violating trilinear soft terms in the MSSM*,  
 2174 *Phys. Lett.* **B387** (1996) p. 107, arXiv: [hep-ph/9606237 \[hep-ph\]](#).
- 2175 [83] C. Borschensky et al., *Squark and gluino production cross sections in pp*  
 2176 *collisions at  $\sqrt{s} = 13, 14, 33$  and 100 TeV*,  
 2177 *Eur. Phys. J.* **C74** (2014) p. 3174, arXiv: [1407.5066 \[hep-ph\]](#).

- 2178 [84] M. Klasen, M. Pohl, and G. Sigl, *Indirect and direct search for dark matter*,  
2179 Prog. Part. Nucl. Phys. **85** (2015) p. 1, arXiv: [1507.03800](https://arxiv.org/abs/1507.03800) [hep-ph].
- 2180 [85] L. Evans and P. Bryant, *LHC Machine*, JINST **3** (2008) S08001.
- 2181 [86] Vladimir Shiltsev, “Accelerator Physics and Technology,” Aug. 2016,  
2182 URL: [https://indico.fnal.gov/sessionDisplay.py?sessionId=3&](https://indico.fnal.gov/sessionDisplay.py?sessionId=3&confId=11505#20160811)  
2183 [confId=11505#20160811](https://indico.fnal.gov/sessionDisplay.py?sessionId=3&confId=11505#20160811).
- 2184 [87] *LEP design report*, Copies shelved as reports in LEP, PS and SPS libraries,  
2185 Geneva: CERN, 1984, URL: <https://cds.cern.ch/record/102083>.
- 2186 [88] ATLAS Collaboration,  
2187 *The ATLAS Experiment at the CERN Large Hadron Collider*,  
2188 JINST **3** (2008) S08003.
- 2189 [89] ATLAS Collaboration, *2015 start-up trigger menu and initial performance  
2190 assessment of the ATLAS trigger using Run-2 data*,  
2191 ATL-DAQ-PUB-2016-001, 2016,  
2192 URL: <https://cds.cern.ch/record/2136007/>.
- 2193 [90] ATLAS Collaboration, *Performance of the ATLAS Inner Detector Track and  
2194 Vertex Reconstruction in High Pile-Up LHC Environment*,  
2195 ATLAS-CONF-2012-042, 2012,  
2196 URL: <https://cds.cern.ch/record/1435196>.
- 2197 [91] ATLAS Collaboration, *Early Inner Detector Tracking Performance in the  
2198 2015 Data at  $\sqrt{s} = 13$  TeV*, ATL-PHYS-PUB-2015-051, 2015,  
2199 URL: <https://cds.cern.ch/record/2110140>.
- 2200 [92] K Hamano, A Morley, and A Salzburger,  
2201 “Track Reconstruction Performance and Efficiency Estimation using different  
2202 ID geometry samples,” tech. rep. ATL-COM-PHYS-2012-1541,  
2203 plots for a poster at HCP: CERN, Oct. 2012,  
2204 URL: <https://cds.cern.ch/record/1489674>.
- 2205 [93] ATLAS Collaboration,  
2206 *Electron reconstruction and identification efficiency measurements with the*  
2207 *ATLAS detector using the 2011 LHC proton–proton collision data*,  
2208 Eur. Phys. J. C **74** (2014) p. 2941, arXiv: [1404.2240](https://arxiv.org/abs/1404.2240) [hep-ex].
- 2209 [94] ATLAS Collaboration, *Topological cell clustering in the ATLAS calorimeters  
2210 and its performance in LHC Run 1* (2016), arXiv: [1603.02934](https://arxiv.org/abs/1603.02934) [hep-ex].

- 2211 [95] ATLAS Collaboration, *Jet energy resolution in proton–proton collisions at*  
 2212  $\sqrt{s} = 7 \text{ TeV}$  *recorded in 2010 with the ATLAS detector,*  
 2213 *Eur. Phys. J. C* **73** (2013) p. 2306, arXiv: [1210.6210](https://arxiv.org/abs/1210.6210) [hep-ex].
- 2214 [96] M. Aaboud et al., *Measurement of the photon identification efficiencies with*  
 2215 *the ATLAS detector using LHC Run-1 data* (2016),  
 2216 arXiv: [1606.01813](https://arxiv.org/abs/1606.01813) [hep-ex].
- 2217 [97] ATLAS Collaboration, *Electron and photon energy calibration with the*  
 2218 *ATLAS detector using LHC Run 1 data*, *Eur. Phys. J. C* **74** (2014) p. 3071,  
 2219 arXiv: [1407.5063](https://arxiv.org/abs/1407.5063) [hep-ex].
- 2220 [98] “Electron and photon energy calibration with the ATLAS detector using  
 2221 data collected in 2015 at  $\sqrt{s} = 13 \text{ TeV}$ ,”  
 2222 tech. rep. ATL-PHYS-PUB-2016-015, CERN, Aug. 2016,  
 2223 URL: <https://cds.cern.ch/record/2203514>.
- 2224 [99] ATLAS Collaboration, *Muon reconstruction performance of the ATLAS*  
 2225 *detector in proton–proton collision data at  $\sqrt{s} = 13 \text{ TeV}$ ,*  
 2226 *Eur. Phys. J. C* **76** (2016) p. 292, arXiv: [1603.05598](https://arxiv.org/abs/1603.05598) [hep-ex].
- 2227 [100] ATLAS Collaboration, *Jet energy measurement with the ATLAS detector in*  
 2228 *proton–proton collisions at  $\sqrt{s} = 7 \text{ TeV}$* , *Eur. Phys. J. C* **73** (2013) p. 2304,  
 2229 arXiv: [1112.6426](https://arxiv.org/abs/1112.6426) [hep-ex].
- 2230 [101] ATLAS Collaboration,  
 2231 *Jet energy measurement and its systematic uncertainty in proton–proton*  
 2232 *collisions at  $\sqrt{s} = 7 \text{ TeV}$  with the ATLAS detector,*  
 2233 *Eur. Phys. J. C* **75** (2015) p. 17, arXiv: [1406.0076](https://arxiv.org/abs/1406.0076) [hep-ex].
- 2234 [102] S. D. Ellis and D. E. Soper,  
 2235 *Successive combination jet algorithm for hadron collisions*,  
 2236 *Phys. Rev.* **D48** (1993) p. 3160, arXiv: [hep-ph/9305266](https://arxiv.org/abs/hep-ph/9305266) [hep-ph].
- 2237 [103] M. Cacciari and G. P. Salam, *Dispelling the  $N^3$  myth for the  $k_t$  jet-finder*,  
 2238 *Phys. Lett.* **B641** (2006) p. 57, arXiv: [hep-ph/0512210](https://arxiv.org/abs/hep-ph/0512210) [hep-ph].
- 2239 [104] M. Cacciari, G. P. Salam, and G. Soyez,  
 2240 *The Anti- $k(t)$  jet clustering algorithm*, *JHEP* **04** (2008) p. 063,  
 2241 arXiv: [0802.1189](https://arxiv.org/abs/0802.1189) [hep-ph].
- 2242 [105] *Particle-Flow Event Reconstruction in CMS and Performance for Jets, Taus,*  
 2243 *and MET* (2009).

- 2244 [106] ATLAS Collaboration,  
2245 *Tagging and suppression of pileup jets with the ATLAS detector*,  
2246 ATLAS-CONF-2014-018, 2014,  
2247 URL: <https://cds.cern.ch/record/1700870>.
- 2248 [107] M. Cacciari, G. P. Salam, and G. Soyez, *The Catchment Area of Jets*,  
2249 JHEP **04** (2008) p. 005, arXiv: [0802.1188 \[hep-ph\]](https://arxiv.org/abs/0802.1188).
- 2250 [108] “Optimisation of the ATLAS  $b$ -tagging performance for the 2016 LHC Run,”  
2251 tech. rep. ATL-PHYS-PUB-2016-012, CERN, June 2016,  
2252 URL: <https://cds.cern.ch/record/2160731>.
- 2253 [109] G. Aad et al., *Performance of algorithms that reconstruct missing transverse*  
2254 *momentum in  $\sqrt{s} = 8$  TeV proton-proton collisions in the ATLAS detector*  
2255 (2016), arXiv: [1609.09324 \[hep-ex\]](https://arxiv.org/abs/1609.09324).
- 2256 [110] ATLAS Collaboration,  
2257 *Prospects for Supersymmetry discovery based on inclusive searches at a*  
2258 *7 TeV centre-of-mass energy with the ATLAS detector*,  
2259 ATL-PHYS-PUB-2010-010, 2010,  
2260 URL: <https://cds.cern.ch/record/1278474>.
- 2261 [111] ATLAS Collaboration,  
2262 *Expected sensitivity studies for gluino and squark searches using the early*  
2263 *LHC 13 TeV Run-2 dataset with the ATLAS experiment*,  
2264 ATL-PHYS-PUB-2015-005, 2015, URL:  
2265 <https://atlas.web.cern.ch/Atlas/GROUPS/PHYSICS/PUBNOTES/ATL-PHYS-PUB-2015-005>.
- 2267 [112] ATLAS Collaboration, *Expected performance of missing transverse*  
2268 *momentum reconstruction for the ATLAS detector at  $\sqrt{s} = 13$  TeV*,  
2269 ATL-PHYS-PUB-2015-023, 2015,  
2270 URL: <https://cds.cern.ch/record/2037700>.
- 2271 [113] ATLAS Collaboration,  
2272 *Performance of missing transverse momentum reconstruction with the*  
2273 *ATLAS detector in the first proton–proton collisions at  $\sqrt{s} = 13$  TeV*,  
2274 ATL-PHYS-PUB-2015-027, 2015,  
2275 URL: <https://cds.cern.ch/record/2037904>.
- 2276 [114] P. Jackson, C. Rogan, and M. Santoni, *Sparticles in Motion - getting to the*  
2277 *line in compressed scenarios with the Recursive Jigsaw Reconstruction*  
2278 (2016), arXiv: [1607.08307 \[hep-ph\]](https://arxiv.org/abs/1607.08307).

- 2279 [115] ATLAS Collaboration,  
2280 *Further searches for squarks and gluinos in final states with jets and missing*  
2281 *transverse momentum at  $\sqrt{s} = 13$  TeV with the ATLAS detector,*  
2282 ATLAS-CONF-2016-078, 2016,  
2283 URL: <https://cds.cern.ch/record/2206252>.
- 2284 [116] C. Rogan, *Kinematical variables towards new dynamics at the LHC* (2010),  
2285 arXiv: [1006.2727 \[hep-ph\]](https://arxiv.org/abs/1006.2727).
- 2286 [117] M. R. Buckley et al.,  
2287 *Super-Razor and Searches for Sleptons and Charginos at the LHC*,  
2288 Phys. Rev. D **89** (2014) p. 055020, arXiv: [1310.4827 \[hep-ph\]](https://arxiv.org/abs/1310.4827).
- 2289 [118] CMS Collaboration, *Search for supersymmetry using razor variables in*  
2290 *events with b-tagged jets in pp collisions at  $\sqrt{s} = 8$  TeV,*  
2291 Phys. Rev. D **91** (2015) p. 052018, arXiv: [1502.00300 \[hep-ex\]](https://arxiv.org/abs/1502.00300).
- 2292 [119] Chris Rogan, “RestFrames,” URL: [{http://restframes.com}](http://restframes.com).
- 2293 [120] M. Baak et al., *HistFitter software framework for statistical data analysis*,  
2294 Eur. Phys. J. C **75** (2015) p. 153, arXiv: [1410.1280 \[hep-ex\]](https://arxiv.org/abs/1410.1280).
- 2295 [121] ATLAS Collaboration, *Monte Carlo Generators for the Production of a W*  
2296 *or Z/ $\gamma^*$  Boson in Association with Jets at ATLAS in Run 2*,  
2297 ATL-PHYS-PUB-2016-003, 2016,  
2298 URL: <https://cds.cern.ch/record/2120133>.
- 2299 [122] ATLAS Collaboration, *Simulation of top-quark production for the ATLAS*  
2300 *experiment at  $\sqrt{s} = 13$  TeV*, ATL-PHYS-PUB-2016-004, 2016,  
2301 URL: <https://cds.cern.ch/record/2120417>.
- 2302 [123] ATLAS Collaboration, *Multi-boson simulation for 13 TeV ATLAS analyses*,  
2303 ATL-PHYS-PUB-2016-002, 2016,  
2304 URL: <https://cds.cern.ch/record/2119986>.
- 2305 [124] R. D. Cousins, J. T. Linnemann, and J. Tucker,  
2306 *Evaluation of three methods for calculating statistical significance when*  
2307 *incorporating a systematic uncertainty into a test of the background-only*  
2308 *hypothesis for a Poisson process*, Nucl. Instrum. Meth. A **595** (2008) p. 480.



2309

## *The Standard Model*

2310 In this appendix, we provide a brief overview of the basic ingredients involved in  
2311 construction of the Standard Model Lagrangian : quantum field theory, symmetries,  
2312 and symmetry breaking.

## **2313 Quantum Field Theory**

2314

2315 In this section, we provide a brief overview of the necessary concepts from  
2316 Quantum Field Theory (QFT).

cite Yuval's  
lectures  
and notes  
somehow

2317 In modern physics, the laws of nature are described by the “action”  $S$ , with the  
2318 imposition of the principle of minimum action. The action is the integral over the cite  
2319 spacetime coordinates of the “Lagrangian density”  $\mathcal{L}$ , or Lagrangian for short. The  
2320 Lagrangian is a function of “fields”; general fields will be called  $\phi(x^\mu)$ , where the  
2321 indices  $\mu$  run over the space-time coordinates. We can then write the action  $S$  as

$$S = \int d^4x \mathcal{L}[\phi_i(x^\mu), \partial_\mu \phi_i(x^\mu)] \quad (9.1)$$

2322 where we have an additional summation over  $i$  (of the different fields). Generally,  
2323 we impose the following constraints on the Lagrangian :

- 2324 1. Translational invariance - The Lagrangian is only a function of the fields  $\phi$  and  
2325 their derivatives  $\partial_\mu \phi$
- 2326 2. Locality - The Lagrangian is only a function of one point  $x_\mu$  in spacetime.

- 2327     3. Reality condition - The Lagrangian is real to conserve probability.
- 2328     4. Lorentz invariance - The Lagrangian is invariant under the Poincarégroup of  
2329       spacetime.
- 2330     5. Analyticity - The Lagrangian is an analytical function of the fields; this is to  
2331       allow the use of perturbation theory.
- 2332     6. Invariance and Naturalness - The Lagrangian is invariant under some internal  
2333       symmetry groups; in fact, the Lagrangian will have *all* terms allowed by the  
imposed symmetry groups.
- maybe add 2334  
in ref here
- 2335     7. Renormalizability - The Lagrangian will be renormalizable - in practice, this  
2336       means there will not be terms with more than power 4 in the fields.
- 2337     The key item from the point of view of this thesis is that of “Invariance and  
2338       Natural”. We impose a set of “symmetries” and then our Lagrangian is the most  
2339       general which is allowed by those symmetries.

## 2340     **Symmetries**

2341     Symmetries can be seen as the fundamental guiding concept of modern physics.

cite?     2342     Symmetries are described by “groups”. To illustrate the importance of symmetries  
2343       and their mathematical description, groups, we start here with two of the simplest  
2344       and most useful examples :  $\mathbb{Z}_2$  and  $U(1)$ .

### 2345      $\mathbb{Z}_2$ symmetry

2346      $\mathbb{Z}_2$  symmetry is the simplest example of a “discrete” symmetry. Consider the most  
2347       general Lagrangian of a single real scalar field  $\phi(x_\mu)$

$$\mathcal{L}_\phi = \frac{1}{2}\partial_\mu\phi\partial^\mu\phi - \frac{m^2}{2}\phi^2 - \frac{\mu}{2\sqrt{2}}\phi^3 - \lambda\phi^4 \quad (9.2)$$

Now we *impose* the symmetry

$$\mathcal{L}(\phi) = \mathcal{L}(-\phi) \quad (9.3)$$

2348 This has the effect of restricting the allowed terms of the Lagrangian. In particular,  
 2349 we can see the term  $\phi^3 \rightarrow -\phi^3$  under the symmetry transformation, and thus must  
 2350 be disallowed by this symmetry. This means under the imposition of this particular  
 2351 symmetry, our Lagrangian should be rewritten as

$$\mathcal{L}_\phi = \frac{1}{2}\partial_\mu\phi\partial^\mu\phi - \frac{m^2}{2}\phi^2 - \lambda\phi^4 \quad (9.4)$$

2352 The effect of this symmetry is that the total number of  $\phi$  particles can only change  
 2353 by even numbers, since the only interaction term  $\lambda\phi^4$  is an even power of the field.  
 2354 This symmetry is often imposed in supersymmetric theories, as we will see in Chapter  
 2355 3.

## 2356 **$U(1)$ symmetry**

2357  $U(1)$  is the simplest example of a continuous (or *Lie*) group. Now consider a theory  
 2358 with a single complex scalar field  $\phi = \text{Re } \phi + i \text{Im } \phi$

$$\mathcal{L}_\phi = \delta_{i,j} \frac{1}{2}\partial_\mu\phi_i\partial^\mu\phi_j - \frac{m^2}{2}\phi_i\phi_j - \frac{\mu}{2\sqrt{2}}\phi_i\phi_j\phi_k\phi_l - \lambda\phi_i\phi_j\phi_k\phi_l \quad (9.5)$$

2359 where  $i, j, k, l = \text{Re}, \text{Im}$ . In this case, we impose the following  $U(1)$  symmetry  
 2360 :  $\phi \rightarrow e^{i\theta}, \phi^* \rightarrow e^{-i\theta}$ . We see immediately that this again disallows the third-order  
 2361 terms, and we can write a theory of a complex scalar field with  $U(1)$  symmetry as

$$\mathcal{L}_\phi = \partial_\mu\phi\partial^\mu\phi^* - \frac{m^2}{2}\phi\phi^* - \lambda(\phi\phi^*)^2 \quad (9.6)$$

## 2362 Local symmetries

2363 The two examples considered above are “global” symmetries in the sense that the  
2364 symmetry transformation does not depend on the spacetime coordinate  $x_\mu$ . We know  
2365 to look at local symmetries; in this case, for example with a local  $U(1)$  symmetry, the  
2366 transformation has the form  $\phi(x_\mu) \rightarrow e^{i\theta(x_\mu)}\phi(x_\mu)$ . These symmetries are also known  
2367 as “gauge” symmetries; all symmetries of the Standard Model are gauge symmetries.

There are wide-ranging consequences to the imposition of local symmetries. To begin, we note that the derivative terms of the Lagrangian 9.2 are *not* invariant under a local symmetry transformation

$$\partial_\mu \phi(x_\mu) \rightarrow \partial_\mu(e^{i\theta(x_\mu)}\phi(x_\mu)) = (1 + i\theta(x_\mu))e^{i\theta(x_\mu)}\phi(x_\mu) \quad (9.7)$$

GET THIS  
RIGHT

2368 This leads us to note that the kinetic terms of the Lagrangian are also not invariant  
2369 under a gauge symmetry. This would lead to a model with no dynamics, which is  
2370 clearly unsatisfactory.

2372 Let us take inspiration from the case of global symmetries. We need to define a  
2373 so-called “covariant” derivative  $D^\mu$  such that

$$D^\mu \phi \rightarrow e^{iq\theta(x^\mu)D^\mu}\phi \quad (9.8)$$

$$D^\mu \phi^* \rightarrow e^{-iq\theta(x^\mu)D^\mu}\phi^* \quad (9.9)$$

$$(9.10)$$

2374 Since  $\phi$  and  $\phi^*$  transforms with the opposite phase, this will lead the invariance  
2375 of the Lagrangian under our local gauge transformation. This  $D^\mu$  is of the following  
2376 form

$$D^\mu = \partial_\mu - igqA^\mu \quad (9.11)$$

2377 where  $A^\mu$  is a vector field we introduce with the transformation law

$$A^\mu \rightarrow A^\mu - \frac{1}{g} \partial_\mu \theta \quad (9.12)$$

2378 and  $g$  is the coupling constant associated to vector field. This vector field  $A^\mu$  is  
2379 also known as a “gauge” field.

2380 Since we need to add all allowed terms to the Lagrangian, we define

$$F^{\mu\nu} = A^\mu A^\nu - A^\nu A^\mu \quad (9.13)$$

2381 and then we must also add the kinetic term :

$$\mathcal{L}_{\text{gauge}} = -\frac{1}{4} F^{\mu\nu} F_{\mu\nu} \quad (9.14)$$

2382 The most general renormalizable Lagrangian with fermion and scalar fields can  
2383 be written in the following form

$$\mathcal{L} = \mathcal{L}_{\text{kin}} + \mathcal{L}_\phi + \mathcal{L}_\psi + \mathcal{L}_{\text{Yukawa}} \quad (9.15)$$

## 2384 Symmetry breaking and the Higgs mechanism

2385 Here we view some examples of symmetry breaking. We investigate breaking of a  
2386 global  $U(1)$  symmetry and a local  $U(1)$  symmetry. The SM will break the electroweak  
2387 symmetry  $SU(2)xU(1)$ , and in Chapter 3 we will see how supersymmetry must also  
2388 be broken.

2389 There are two ideas of symmetry breaking

- 2390 • Explicit symmetry breaking by a small parameter - in this case, we have a small  
2391 parameter which breaks an “approximate” symmetry of our Lagrangian. An  
2392 example would be the theory of the single scalar field 9.2, when  $\mu \ll m^2$  and

2393         $\mu \ll \lambda$ . In this case, we can often ignore the small term when considering  
 2394        low-energy processes.

2395     • Spontaneous symmetry breaking (SSB) - spontaneous symmetry breaking  
 2396        occurs when the Lagrangian is symmetric with respect to a given symmetry  
 2397        transformation, but the ground state of the theory is *not* symmetric with respect  
 2398        to that transformation. This can have some fascinating consequences, as we  
 2399        will see in the following examples

2400       Symmetry breaking a

## 2401       **U(1) global symmetry breaking**

Consider the theory of a complex scalar field under the  $U(1)$  symmetry, or the transformation

$$\phi \rightarrow e^{i\theta} \phi \quad (9.16)$$

The Lagrangian for this theory is

$$\mathcal{L} = \partial^\mu \phi^\dagger \partial_\mu \phi + \frac{\mu^2}{2} \phi^\dagger \phi + \frac{\lambda}{4} (\phi^\dagger \phi)^2 \quad (9.17)$$

Let us write this theory in terms of two scalar fields,  $h$  and  $\xi$  :  $\phi = (h + i\xi)/\sqrt{2}$ .

The Lagrangian can then be written as

$$\mathcal{L} = \partial^\mu h \partial_\mu h + \partial^\mu \xi d\mu \xi - \frac{\mu^2}{2} (h^2 + \xi^2) - \frac{\lambda}{4} (h^2 + \xi^2)^2 \quad (9.18)$$

First, note that the theory is only stable when  $\lambda > 0$ . To understand the effect of SSB, we now enforce that  $\mu^2 < 0$ , and define  $v^2 = -\mu^2/\lambda$ . We can then write the scalar potential of this theory as :

$$V(\phi) = \lambda(\phi^\dagger \phi - v^2/2)^2 \quad (9.19)$$

Minimizing this equation with respect to  $\phi$ , we can see that the “vacuum expectation value” of the theory is

$$2 < \phi^\dagger \phi > = < h^2 + \xi^2 > = v^2 \quad (9.20)$$

2402        We now reach the “breaking” point of this procedure. In the  $(h, \xi)$  plane, the  
 2403        minima form a circle of radius  $v$ . We are free to choose any of these minima to expand  
 2404        our Lagrangian around; the physics is not affected by this choice. For convenience,  
 2405        choose  $\langle h \rangle = v, \langle \xi^2 \rangle = 0$ .

Now, let us define  $h' = h - v, \xi' = \xi$  with VEVs  $\langle h' \rangle = 0, \langle \xi' \rangle = 0$ . We can  
 then write our spontaneously broken Lagrangian in the form

$$\mathcal{L} = \frac{1}{2}\partial_\mu h'\partial^\mu h' + \frac{1}{2}\partial_\mu \xi'\partial^\mu \xi' - \lambda v^2 h'^2 - \lambda v h'(h'^2 + \xi'^2) - \lambda(h'^2 + \xi'^2)^2 \quad (9.21)$$



---

2406

## *The Standard Model*

2407

2408 **Compressed region N-1 plots**

add some  
text or cut  
this

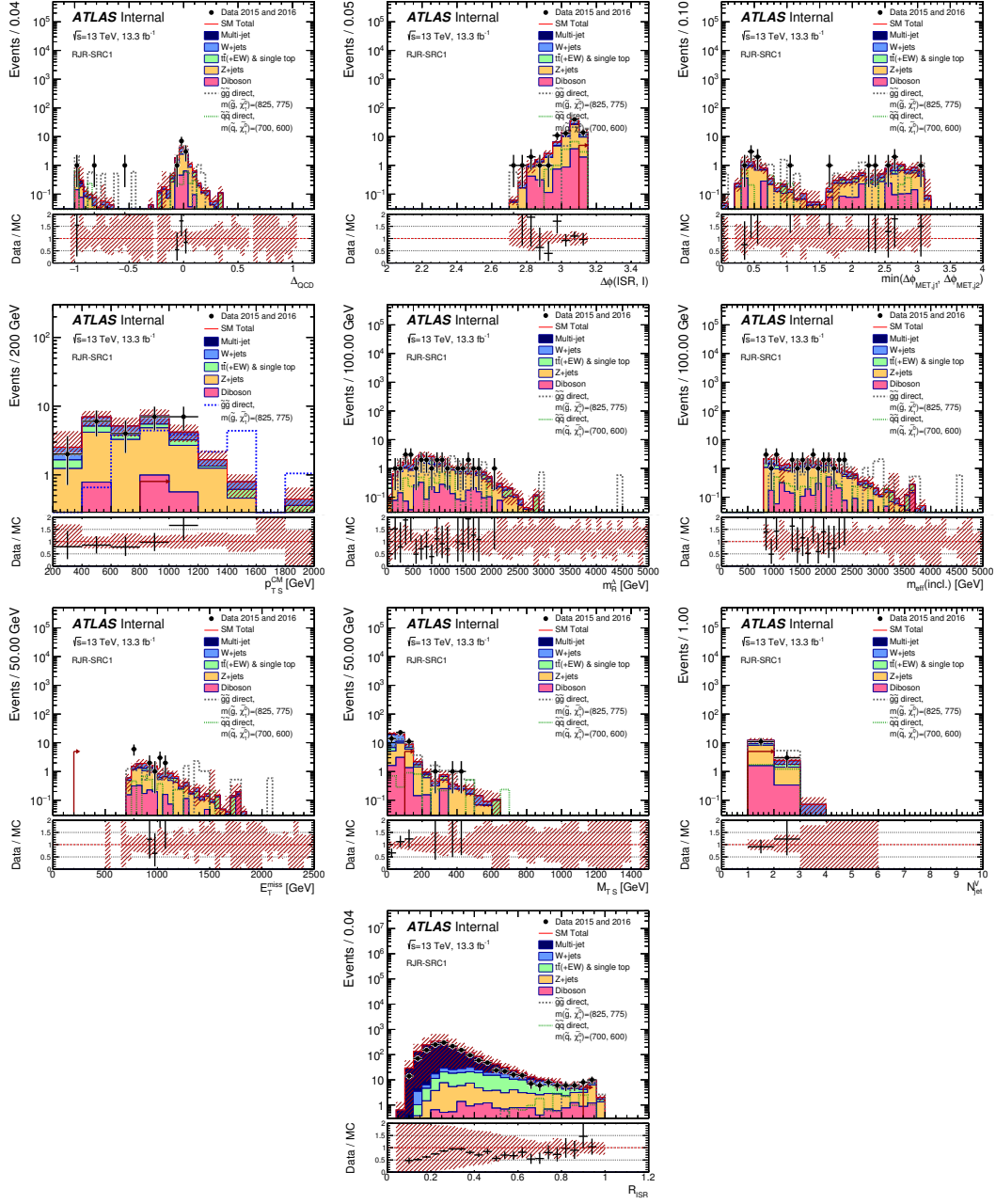


Figure 1

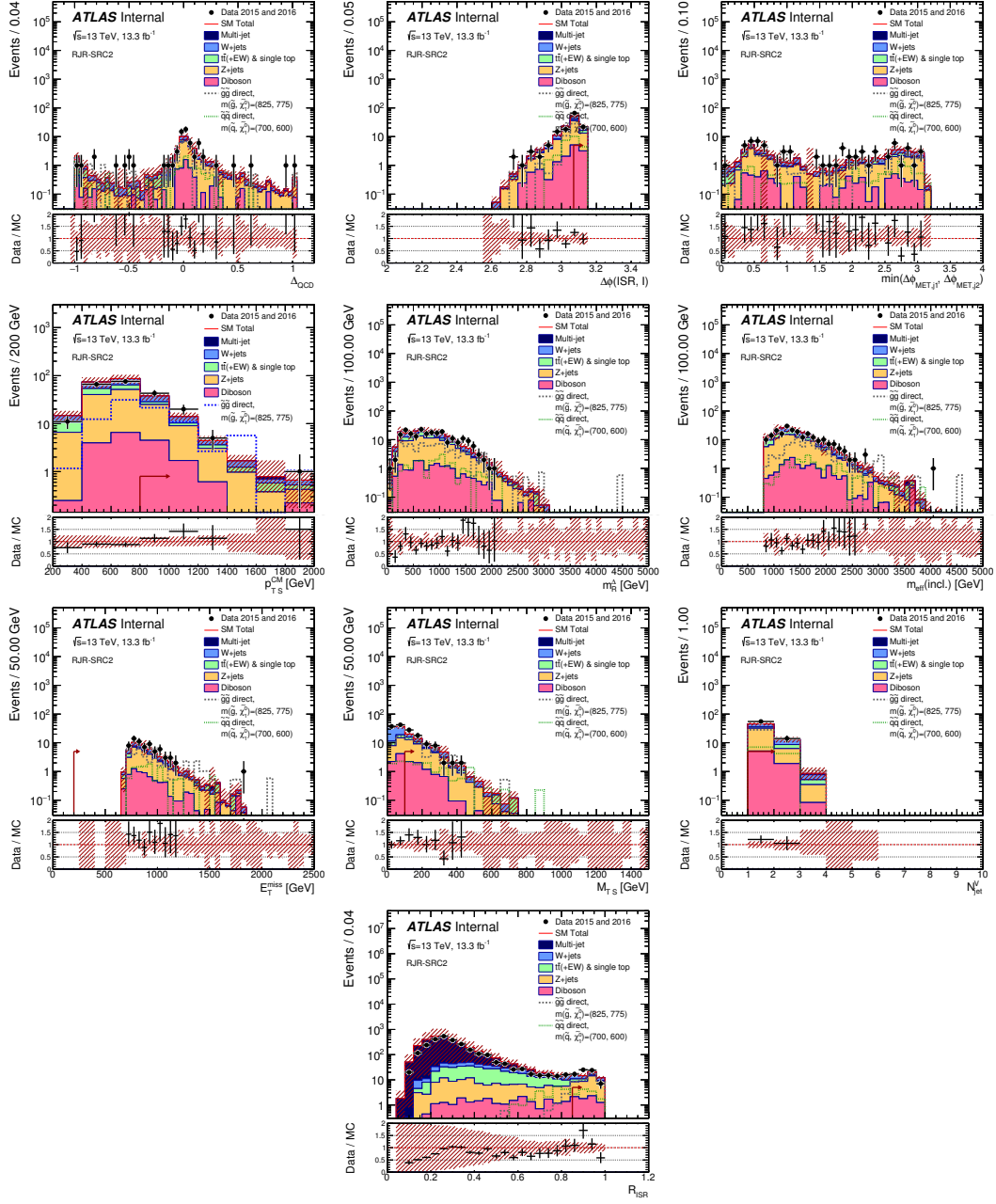


Figure 2

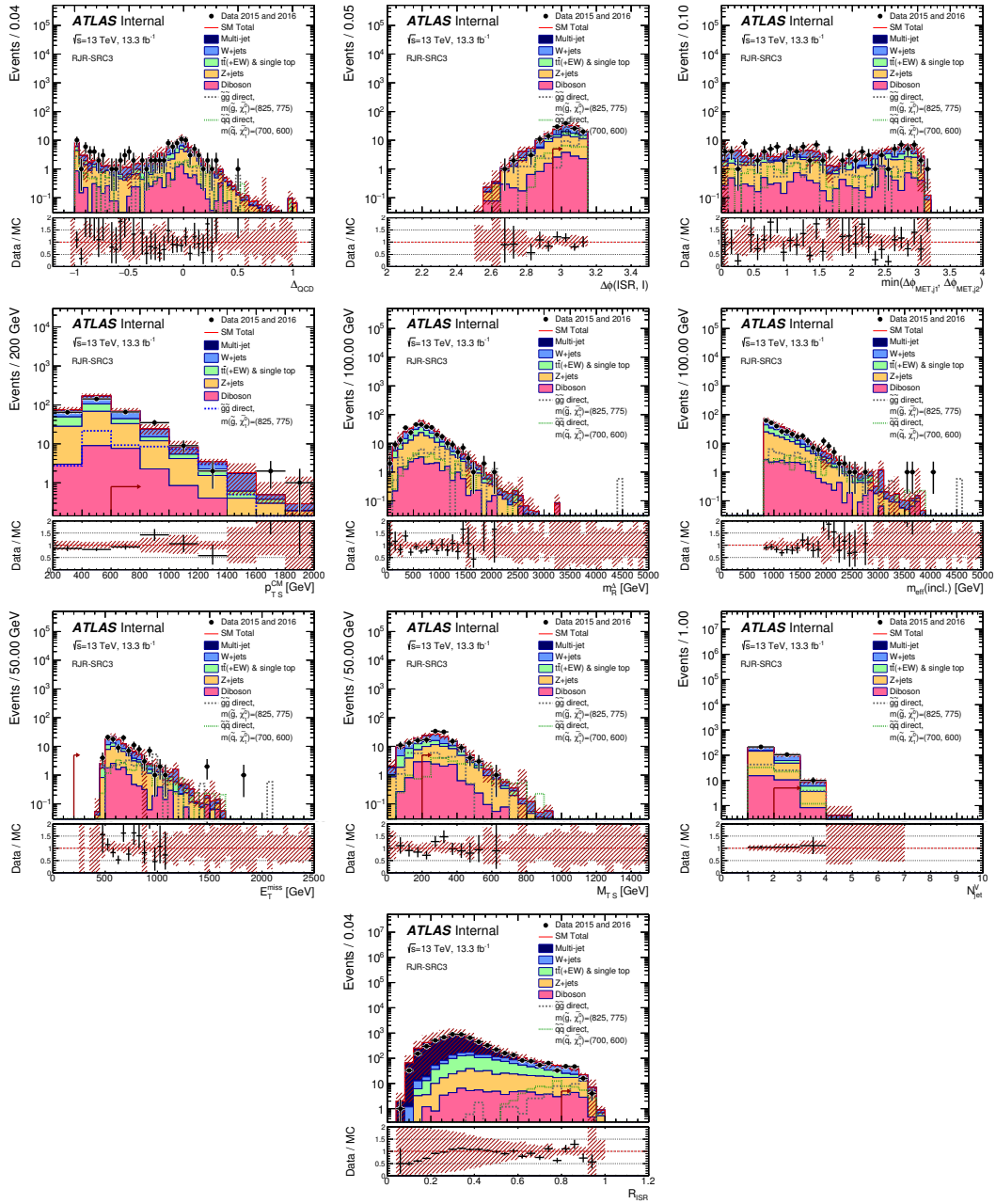


Figure 3

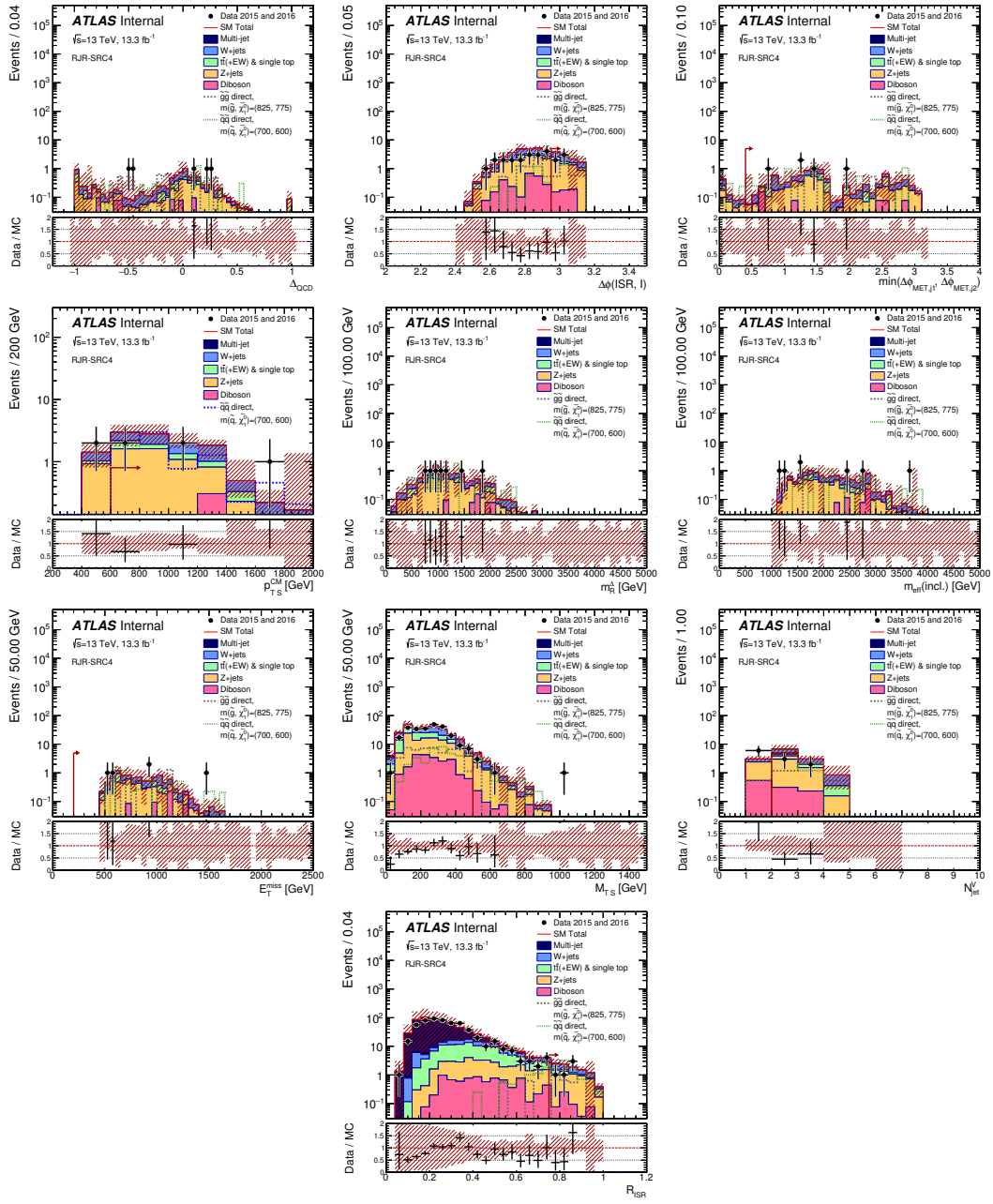


Figure 4

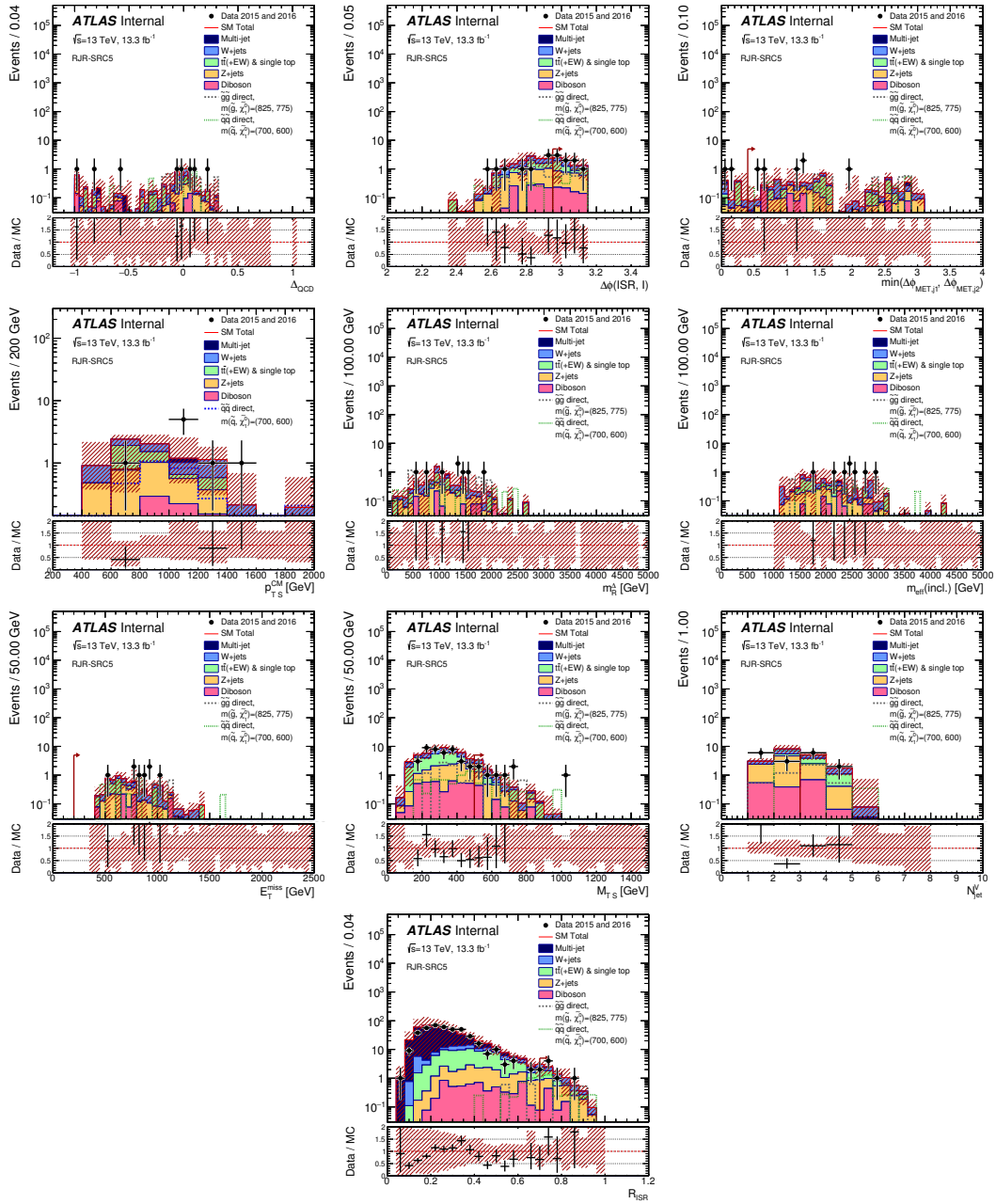


Figure 5

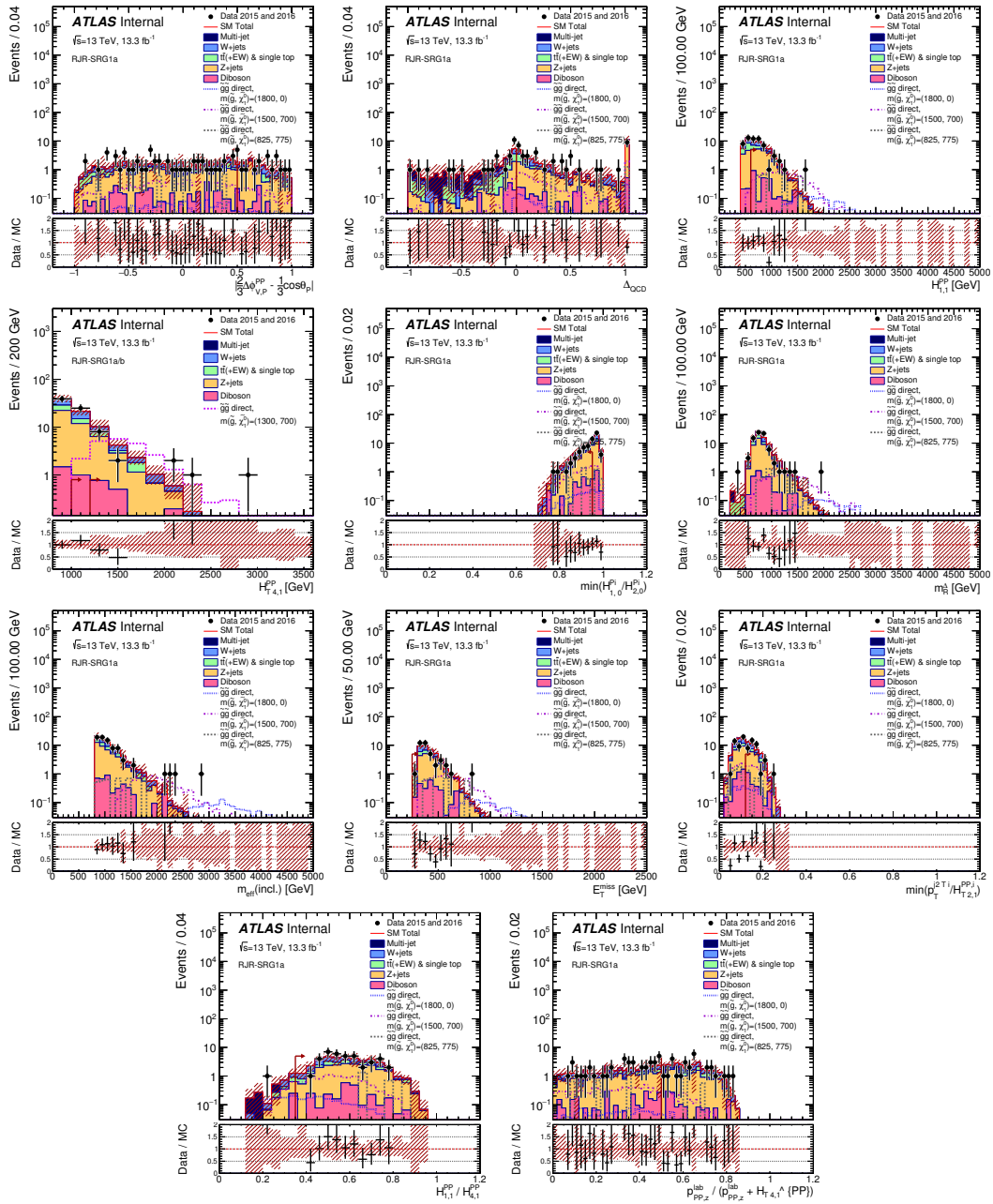


Figure 6

Figure 7

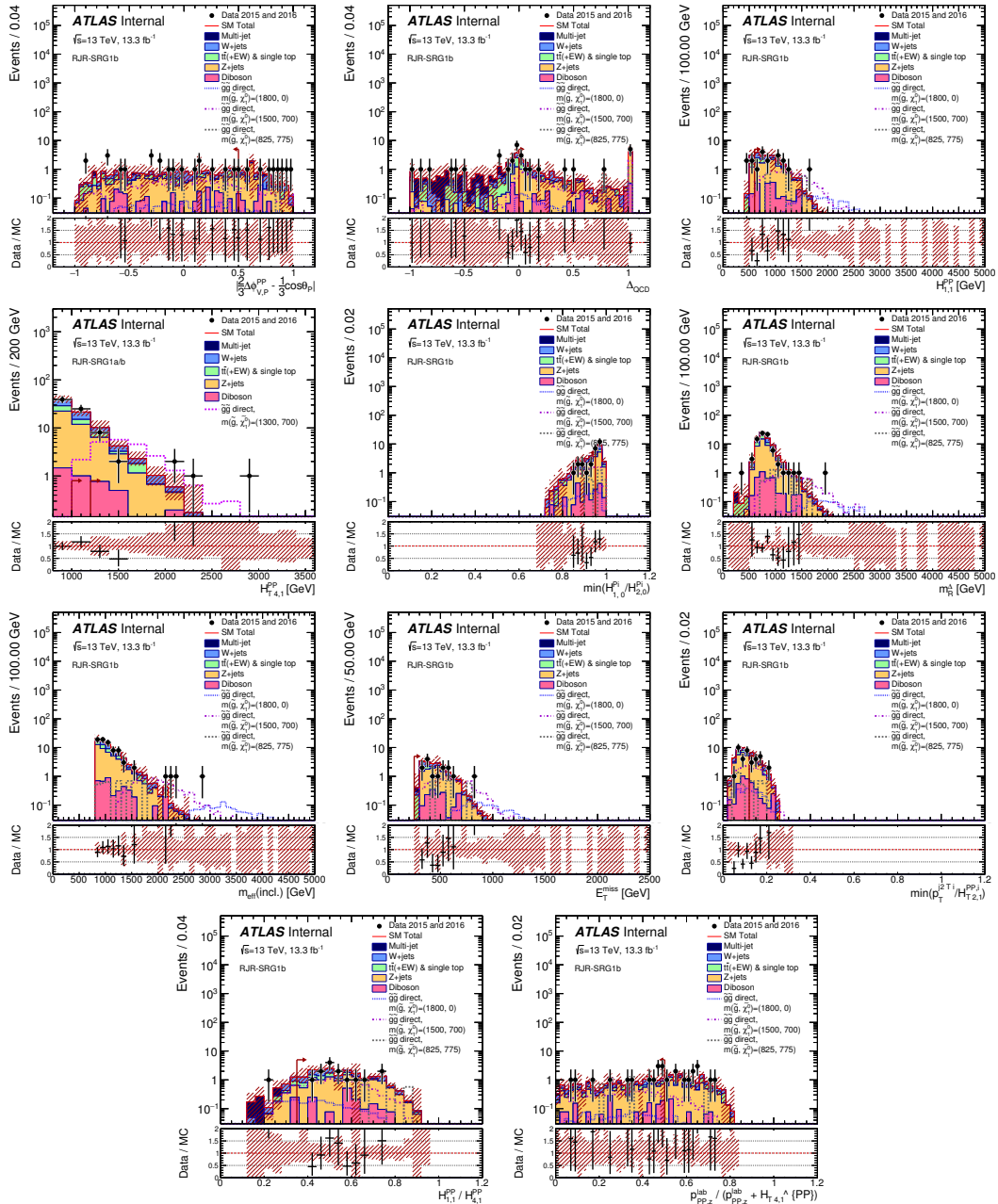


Figure 8

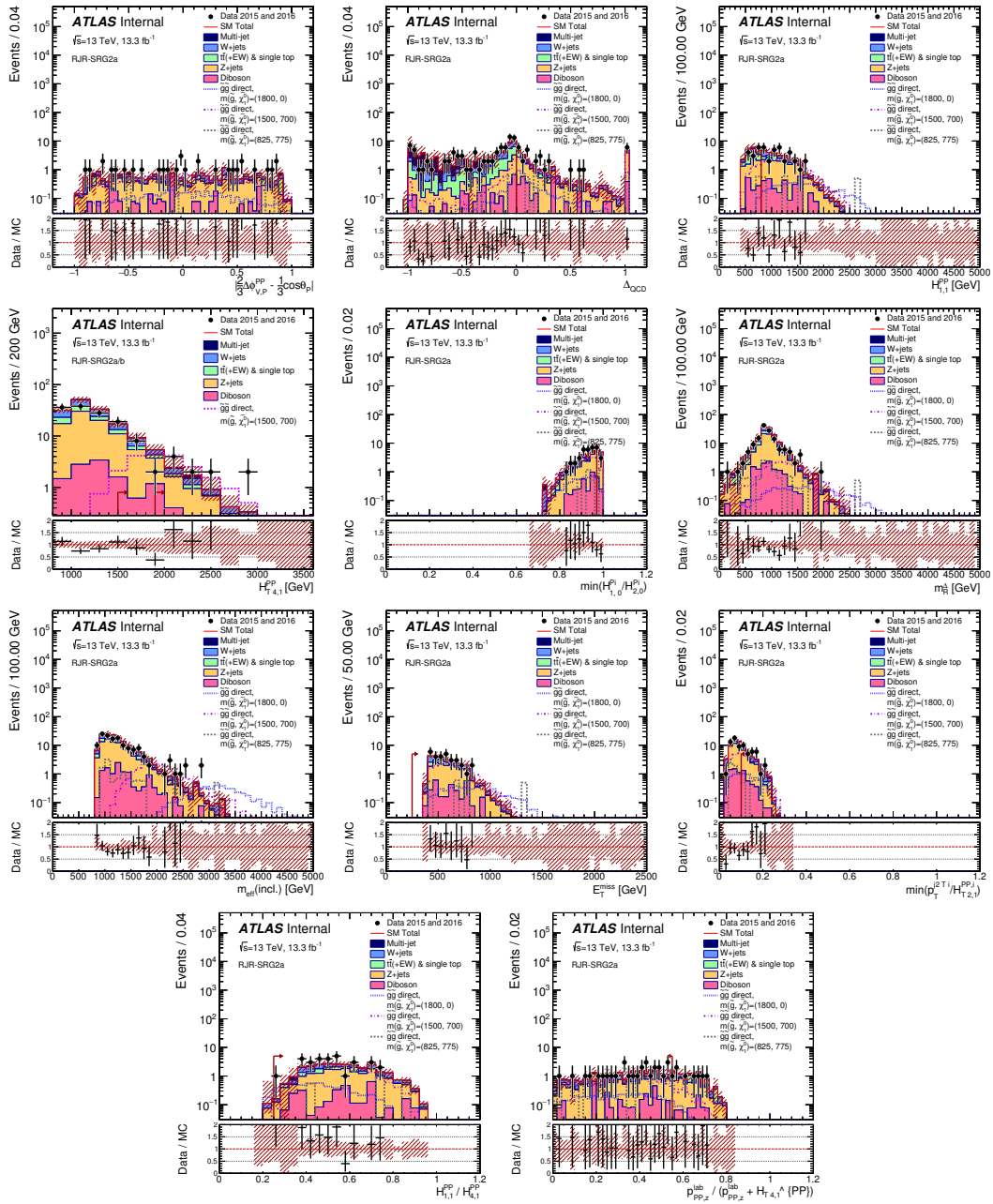


Figure 9

Figure 10

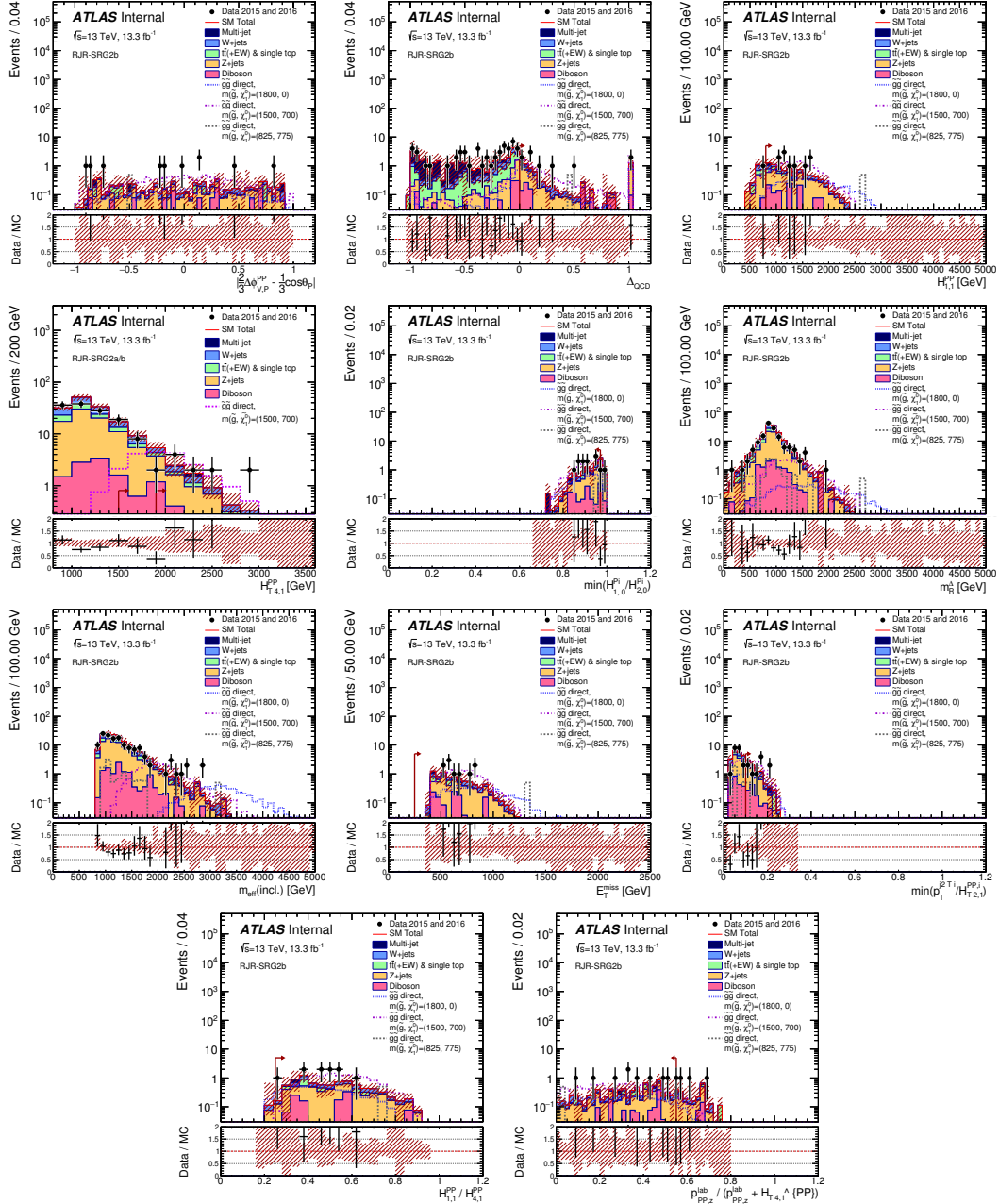


Figure 11

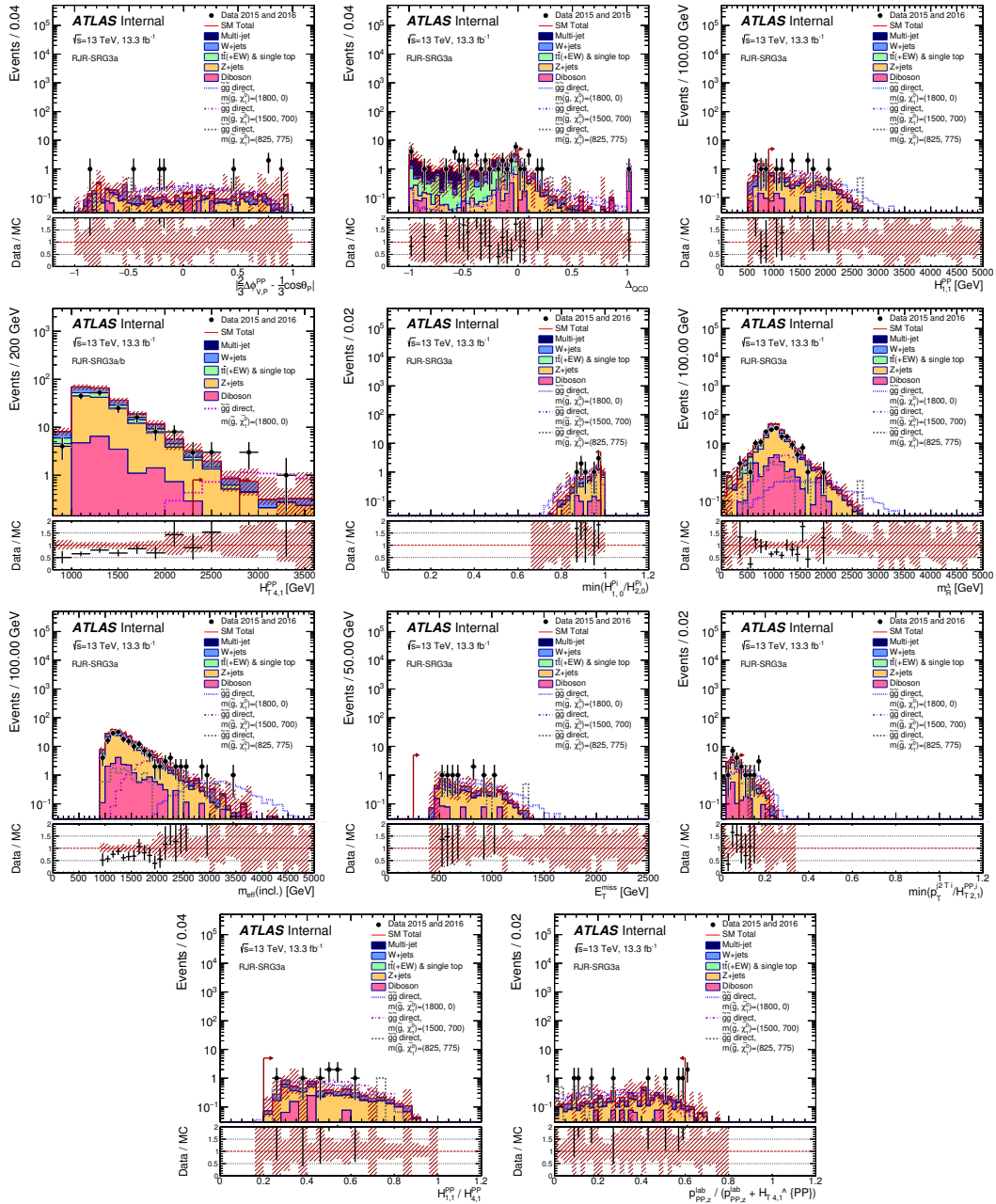


Figure 12

Figure 13

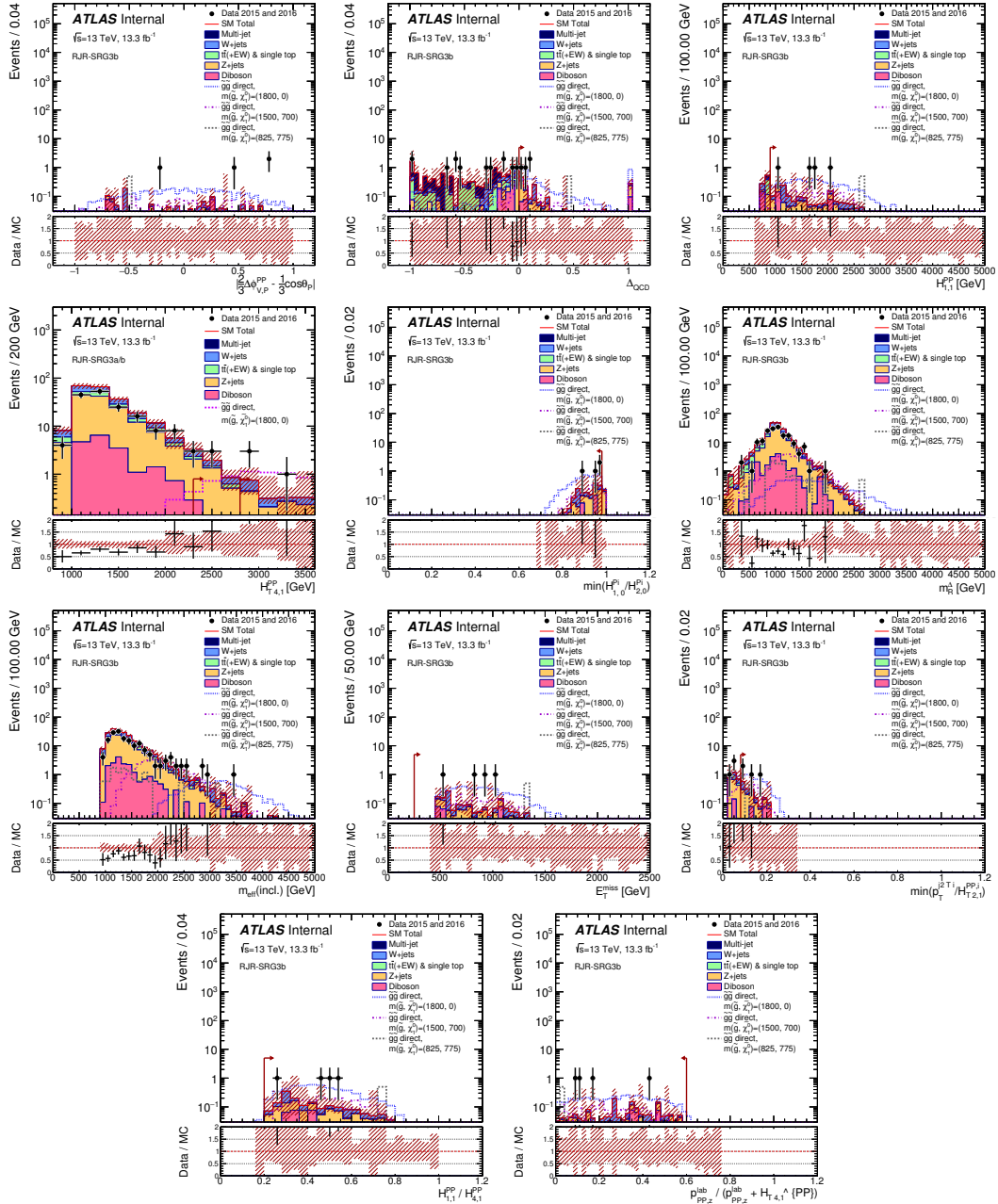


Figure 14

Figure 15

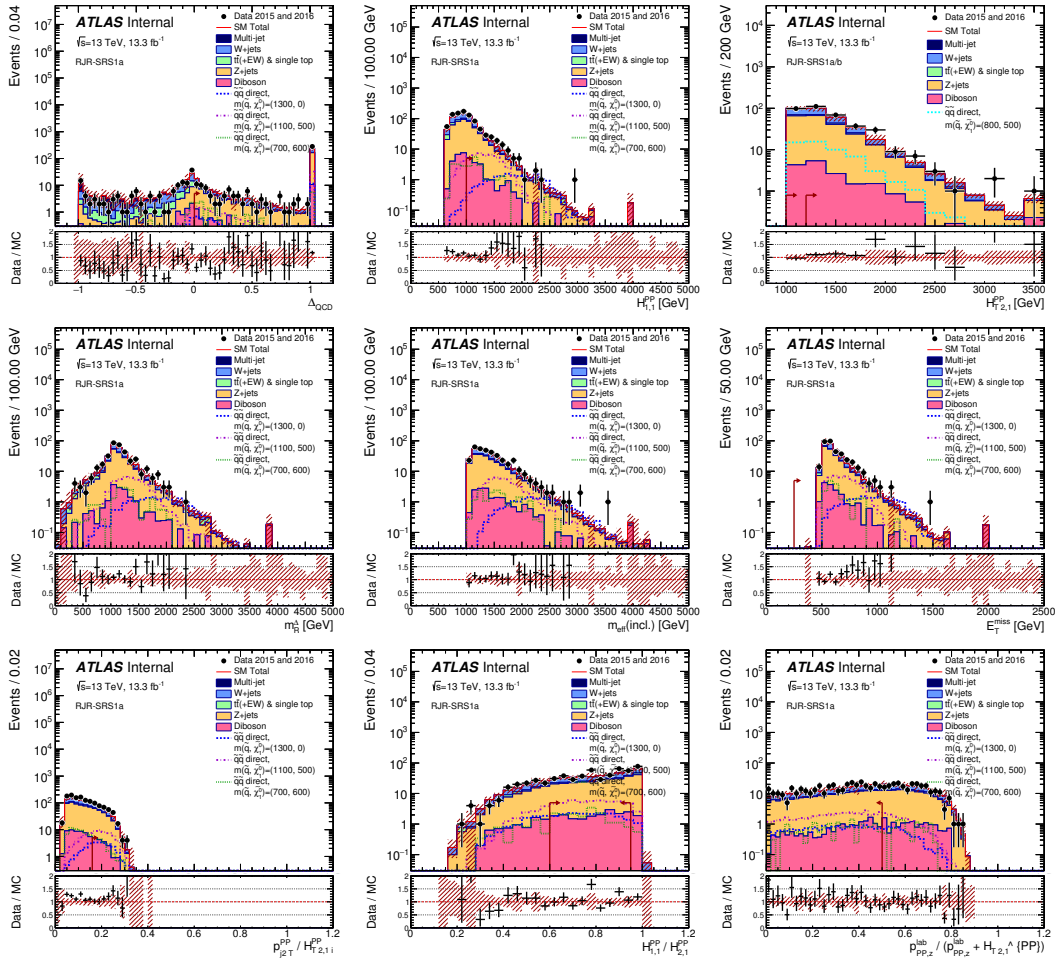


Figure 16

Figure 17

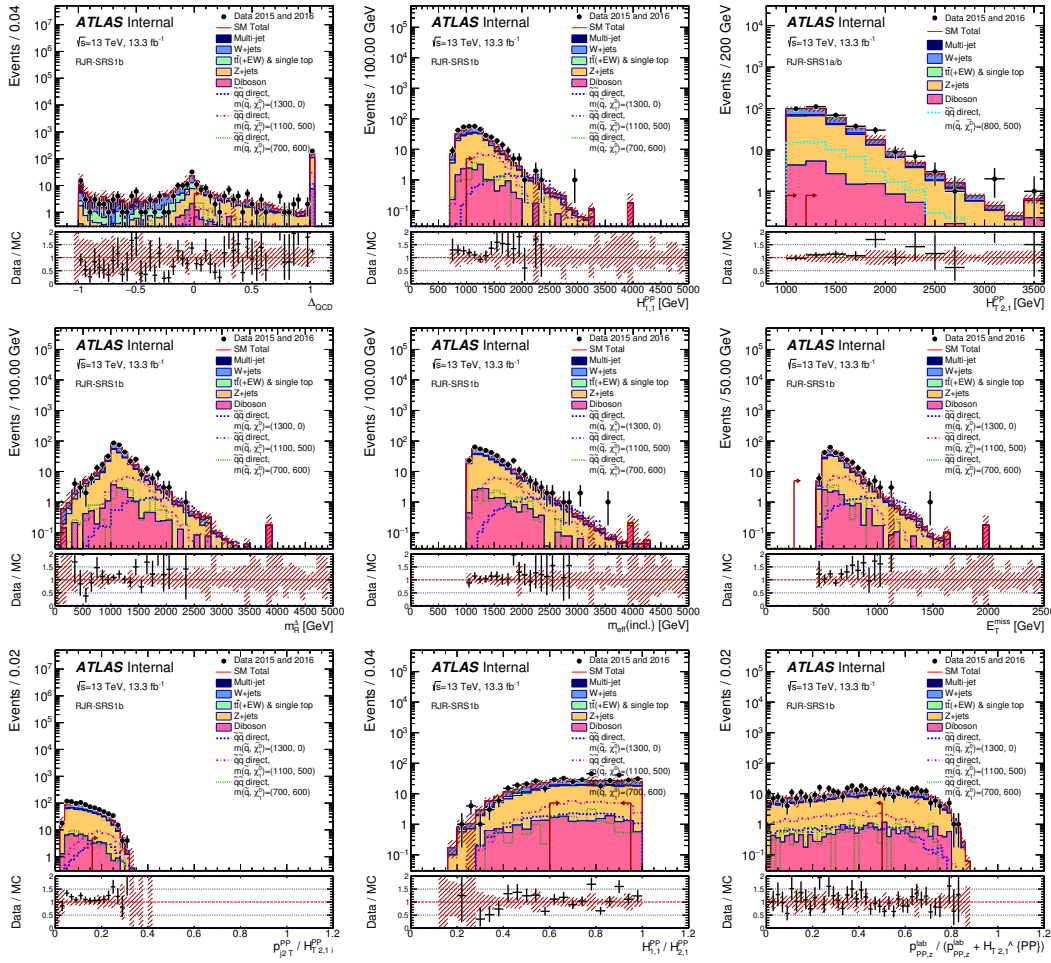


Figure 18

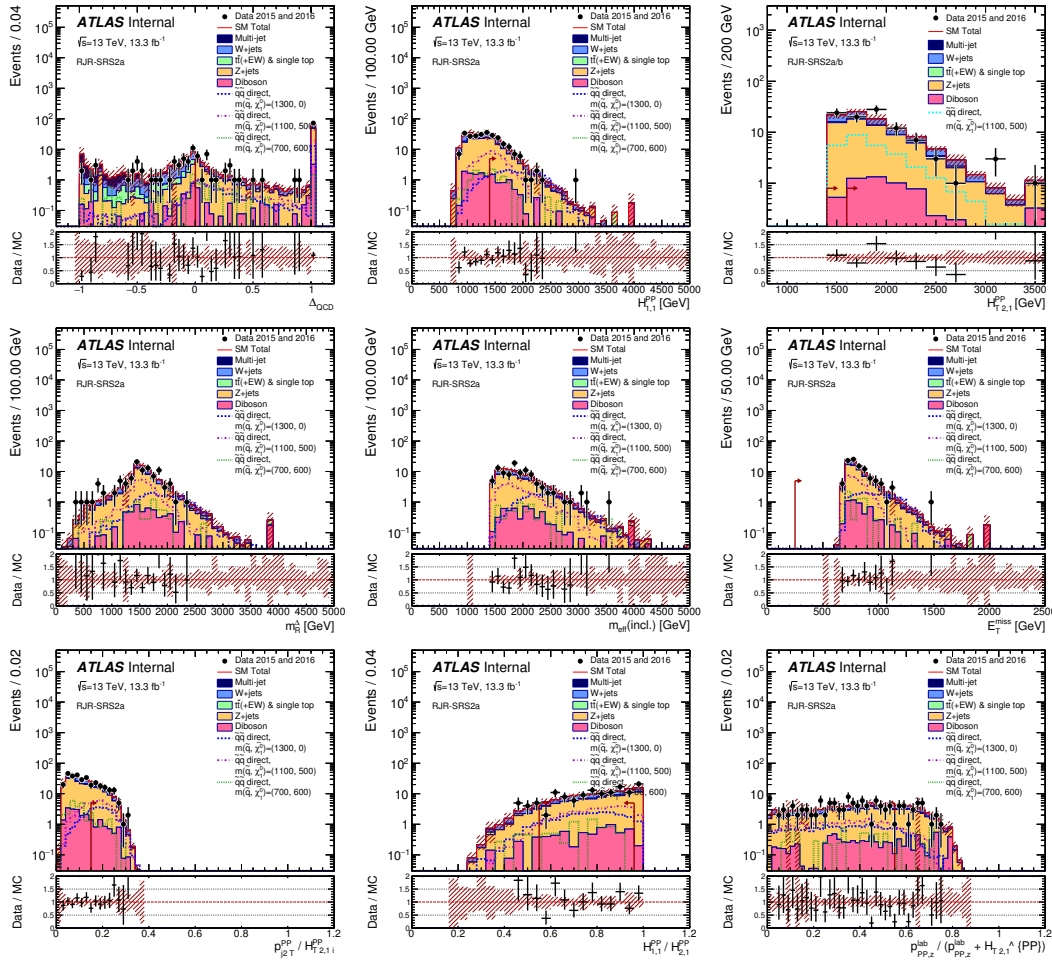


Figure 19

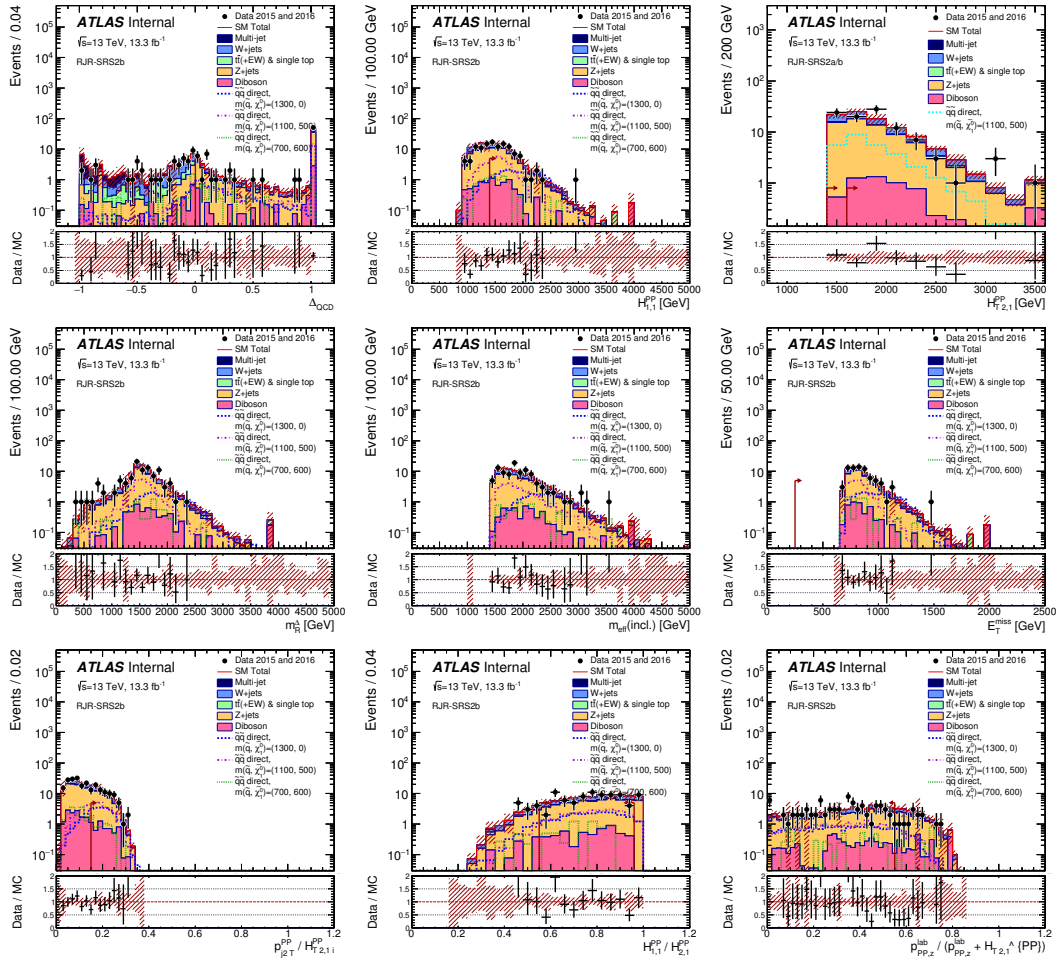


Figure 20

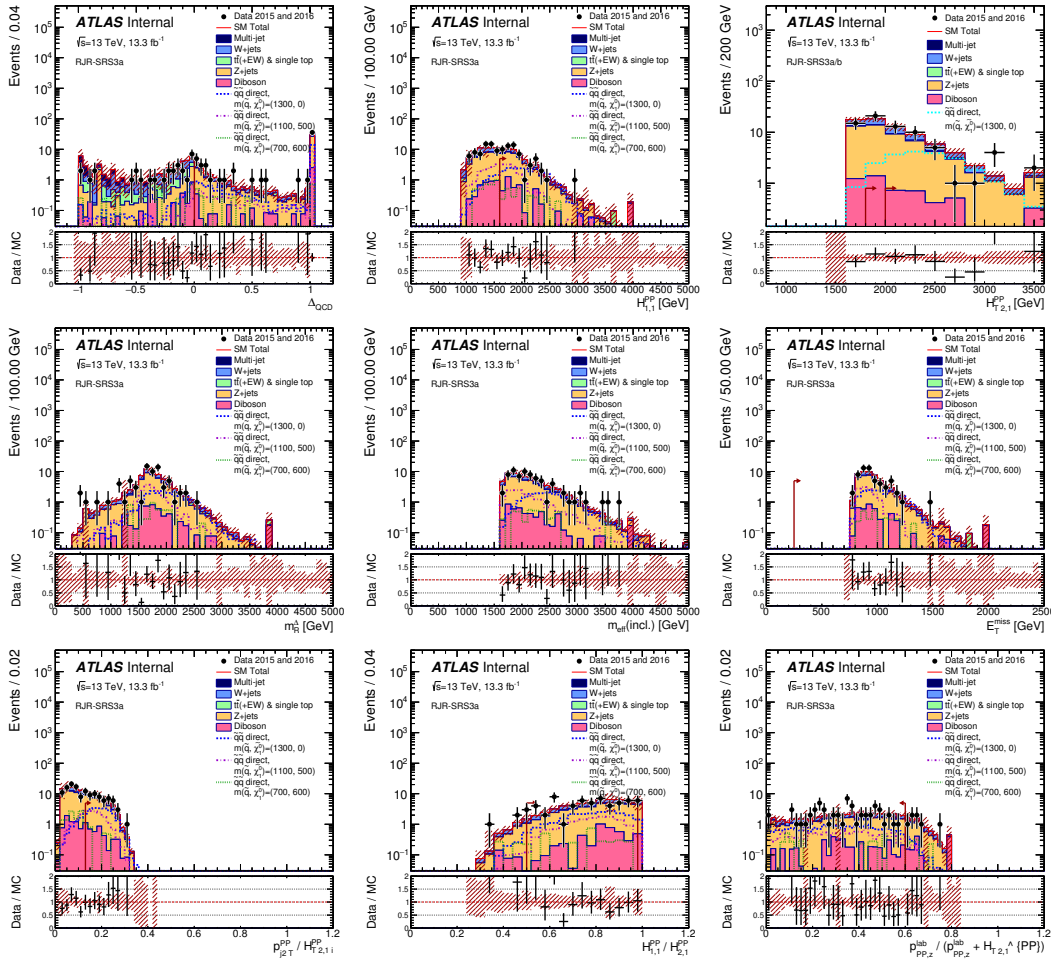


Figure 21

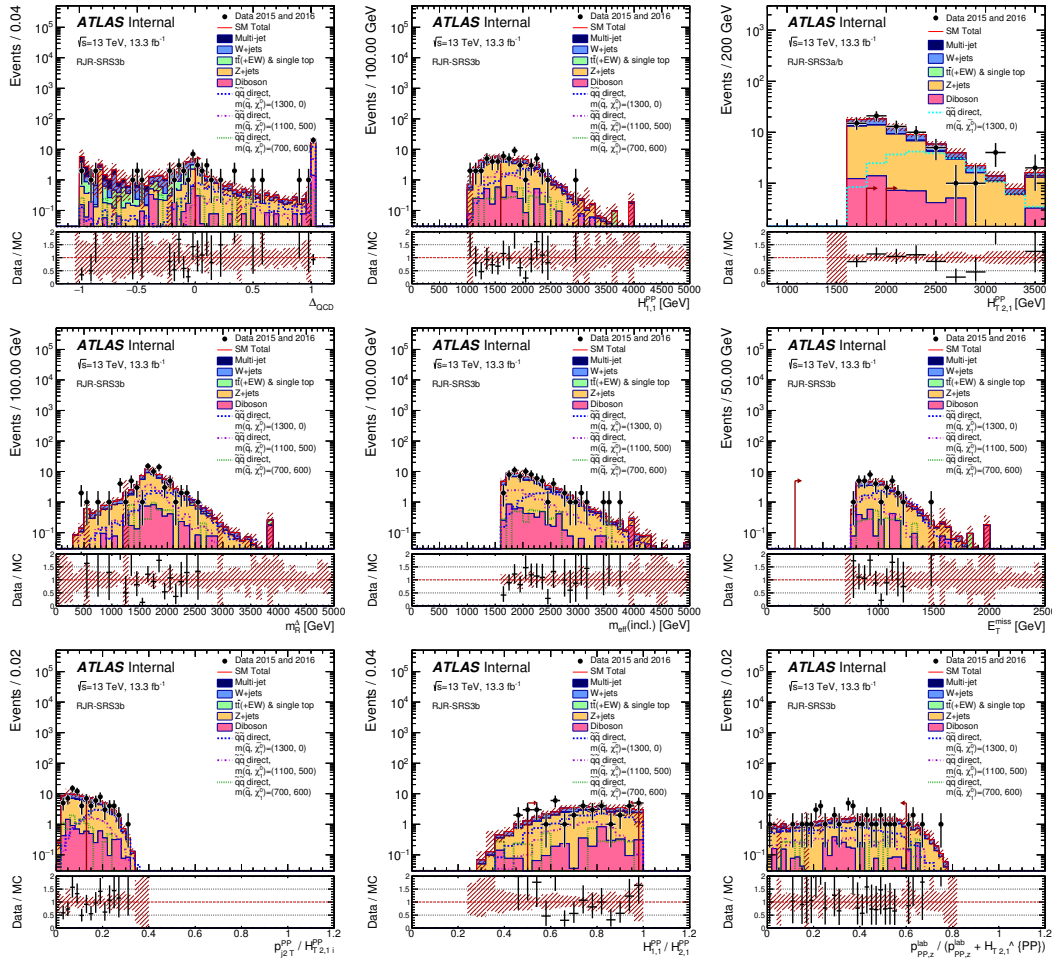


Figure 22